Car Structure Parameter Identification for CAE Barrier Model Development

Master’s Thesis in the Mobility Engineering Master

NIKHIL NAWALE

DEPARTMENT OF MECHANICS AND MARITIME SCIENCES

CHALMERS UNIVERSITY OF TECHNOLOGY
Gothenburg, Sweden 2026
www.chalmers.se

Master's thesis 2026

Car Structure Parameter Identification for CAE Barrier Model Development

NIKHIL NAWALE

Department of Mechanics and Maritime Sciences
Division of Vehicle Safety
Chalmers University of Technology
Gothenburg, Sweden 2026

Car Structure Parameter Identification for CAE Barrier Model Development
NIKHIL NAWALE

Supervisor: Shweta Joshi, Chalmers University of Technology
Supervisor: Fredrik Törnvall, VOLVO Technology AB
Examiner: Robert Thomson, Division of Vehicle Safety, Chalmers University of Technology

Master's Thesis 2026
Department of Mechanics and Maritime Sciences
Division of Vehicle Safety
Chalmers University of Technology
SE-412 96 Gothenburg
Telephone +46 31 772 1000

Cover: Structural layout of a passenger car body highlighting major load paths and structural members. (Source: Volvo XC60 Media Guide [26])

Typeset in LaTeX
Printed by Chalmers Reproservice
Gothenburg, Sweden 2026

Car Structure Parameter Identification for CAE Barrier Model Development
NIKHIL NAWALE
Department of Mechanics and Maritime Sciences
Chalmers University of Technology

Abstract

Frontal collisions between Heavy Goods Vehicles (HGVs) and passenger cars remain a critical safety issue on rural roads due to significant structural and geometrical incompatibilities between the two vehicle types. This study focuses on developing a representative passenger-car surrogate model to support compatibility assessment in car-to-truck crash scenarios, aligned with evolving Euro NCAP protocols. The work involves identifying and categorizing key structural parameters of passenger vehicles—such as load paths, front-end components, and deformation zones—across various European car segments. These parameters are analyzed for geometric variation and translated into stiffness-relevant inputs for the development of a simplified CAE barrier model.

A structured development process is presented in this work, integrating structural positioning, crash response, and stiffness inputs to propose a concept CAE barrier model that aims to capture realistic vehicle deformation behaviour and energy absorption in real-world crashes. Despite limitations related to restricted access to proprietary data and absence of physical testing, the study establishes a structured methodology for stiffness characterization and surrogate modelling. The findings contribute toward improving compatibility evaluation and enhancing Front Underrun Protection Device (FUPD) performance in future HGV safety designs.

Keywords: Frontal collisions, structural incompatibility, HGVs, structural parameters, stiffness characterisation, energy absorption, CAE barrier model, FUPD.

Contents

Acknowledgements

This report is the result of the master thesis work carried out in the Cab Safety and Ergonomics department at VOLVO Technology AB in collaboration with division of Vehicle Safety at Chalmers University of Technology. The thesis fulfills partial requirement for the Master of Science degree in "Mobility Engineering" under Automotive track at Chalmers University of Technology, Gothenburg. This thesis work was started in January 2026 and finished in June 2026.

The project is motivated by the high severity of frontal crashes between HGVs and passenger cars, mainly due to structural and geometrical incompatibilities that are not adequately addressed in current safety evaluations. This work aims to bridge the gap by developing a representative surrogate model to improve crash compatibility analysis and support safer HGV design.

I would like to thank Lina Andersson, Manager, Cab Safety and Ergonomics Department at VOLVO Technology AB for providing us with the opportunity and necessary resources to carry out this thesis work within her team.

I am also grateful to Shweta Joshi from Chalmers and Fredrik Törnvall from VOLVO Technology AB for their constant support and guidance as my supervisors throughout the project. Their valuable suggestions and timely help made this work both interesting and meaningful for us.

Finally, I sincerely express gratitude towards my examiner Professor Robert Thomson at the Chalmers University of Technology for reviewing my work and for the guidance provided throughout. The constant “why” behind every discussion, along with the frequent “that’s interesting” remarks, kept me thinking and motivated during the entire process.

Last but not least, I would like to thank my family and friends for their unwavering support, understanding, and motivation during the course of this work.

Nikhil Nawale, Gothenburg, June 2026

Terminology

Abbreviations

BEV	Battery Electric Vehicle
CAE	Computer Aided Engineering
CFC	Channel Frequency Class
COG	Centre Of Gravity
EA-FUPS	Energy Absorbing Front Underrun Protection System
Euro-NCAP	European New Car Assessment Programme
FIMCAR	Frontal IMpact and Compatibility Assessment Research
FMVSS	Federal Motor Vehicle Safety Standards
FUPD	Front Underrun Protection Device
FUPS	Front Underrun Protection System
FWRB	Full Width Rigid Barrier
HEV	Hybrid Electric Vehicle
HGV	Heavy Goods Vehicle
ICEV	Internal Combustion Engine Vehicle
IIHS	Insurance Institute for Highway Safety
MPDB	Mobile Progressive Deformable Barrier
OEM	Original Equipment Manufacturer
OLC	Occupant Load Criterion
PCA	Principal Component Analysis
SAE	Society of Automotive Engineers
SAFE-UP	proactive SAFEty systems and tools for a constantly UPgrading road environment
SUV	Sports Utility Vehicle
UNECE	United Nations Economic Commission for Europe
US-NCAP	United States New Car Assessment Programme

Symbols with corresponding units

A	Area (mm^2)
A_x	Acceleration in x-direction (g)
δ	Deformation (mm)
D_x	Displacement in x-direction (mm)
E	Energy (kJ)
F_x	Force in x-direction (kN)
k	Stiffness (N/mm)
m	Mass (kg)
σ_c	Crush strength (MPa)
t	Time (ms)
v	Vehicle velocity (km/h)
V_x	Velocity in x-direction (km/h)

List of Figures

List of Tables

1 BACKGROUND

1.1 Traffic Safety

Frontal crashes between Heavy Goods Vehicles (HGVs) and passenger cars remain a serious traffic safety concern, particularly on rural roads with higher speed limits and no median barriers. Although these crashes represent only about 5–11 % of frontal crash cases as reported in SAFE-UP project (2021) [1], they are highly severe, with studies indicating that up to 43–73 % of such collisions result in fatalities, mainly due to mismatches in vehicle characteristics. This severity is largely caused by structural and geometrical incompatibilities—such as differences in mass, stiffness, and load-path alignment—which lead to underride and inefficient energy transfer. Typical real-world scenarios, identified from crash databases and test reconstructions over the last two decades, involve around 50% frontal overlap at relative speeds of about 70km/h, creating highly demanding crash conditions for passenger vehicles [1].

At the same time, the passenger car fleet is evolving with increasing electrification, leading to changes in vehicle mass and structural layouts, particularly in load-path distribution and stiffness. These developments challenge the ability of existing assessment methods—such as the Euro NCAP MPDB test [2]—which were primarily designed for conventional car-to-car interactions, to accurately represent real-world conditions. Earlier studies, including the VC-COMPAT project [3], have provided a baseline understanding of structural compatibility, but they may not fully capture the combined effects of evolving vehicle characteristics and HGV-to-car mismatch. In this context, the current study focuses on understanding how passenger car structures behave during impact, especially in terms of front-end load transfer and deformation. This is closely related to crash compatibility, particularly when interacting with heavier vehicles such as trucks, where Front Underrun Protection Systems (FUPS) plays an important role depending on their engagement with car structures [4].

1.1.1 Passenger car vehicle structure

Passenger car design has undergone significant changes over the years driven by advancements in technology, manufacturing, and safety requirements. Modern vehicles are not only shaped by considerations such as aerodynamics and styling, but also by the need to improve structural performance during crashes. A major focus in vehicle development has been the enhancement of occupant protection, which depends strongly on how the vehicle structure responds under different impact conditions.

As a result, the design of passenger cars has evolved to include well-defined energy-absorbing zones and load paths in the front structure. Components such as longitudinal members, crash boxes, and subframes are arranged in a way that helps manage crash forces and control deformation during an impact [5]. Along with this, safety systems like seatbelts, airbags, and advanced driver assistance features have become standard to provide protection in different types of crashes, including frontal, side, rear, and rollover scenarios. To support these systems, the vehicle body is designed with a combination of deformable zones that absorb impact energy and a rigid occupant compartment, often referred to as the safety cage, which helps limit intrusion and protect passengers.

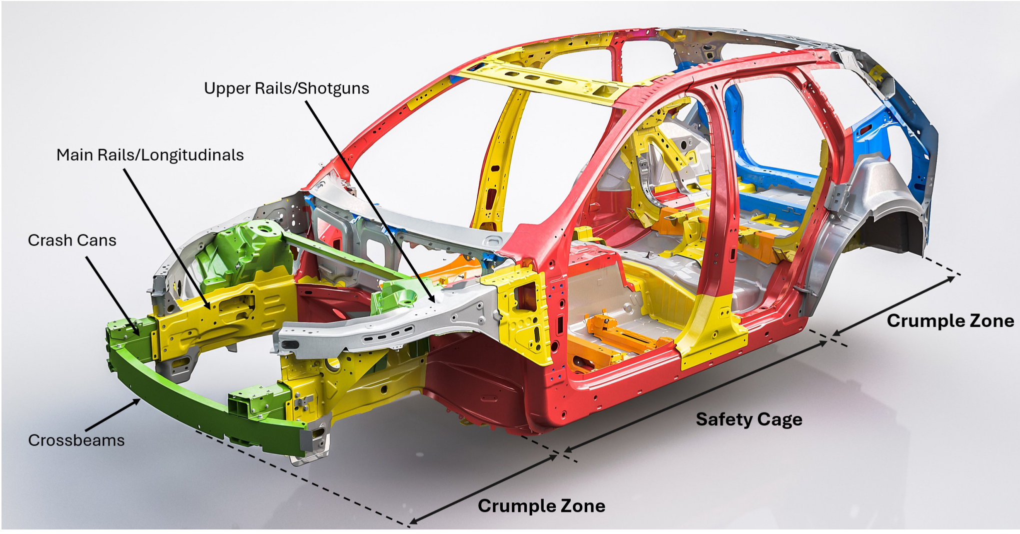

Figure 1.1: Example of passenger vehicle car structure [26]

Figure 1.1 illustrates the structural layout of a passenger car body, highlighting the key components responsible for energy absorption and load transfer during a crash. The front region, referred to as the crumple zone, consists of components such as crash cans, crossbeams, and main longitudinal rails that are designed to deform progressively under impact. This controlled deformation converts the vehicle's kinetic energy into deformation energy, reducing the forces transmitted further into the structure. The load is then transferred through primary structural members such as the main longitudinal rails and upper rails (shotguns) along defined load paths. Behind this, the safety cage is built with higher stiffness to resist deformation and protect the occupant compartment, ensuring that the space around passengers remains intact.

The main energy-absorbing zones are located at the front and rear of the vehicle and are designed to handle different crash conditions by deforming in a controlled manner. In impacts such as a full frontal collision with a rigid barrier, these regions are expected to absorb most of the vehicle's kinetic energy, reducing crash severity and limiting rebound. These zones are designed with varying crush strengths to perform well in collisions with vehicles of different sizes and stiffness, allowing progressive deformation under increasing loads[6]. In contrast, the safety cage is made from high-strength materials and is intended to remain mostly undeformed, maintaining a stable space for occupants and preventing intrusion.

The structural performance of cars is evaluated through programs such as Euro-NCAP and US-NCAP, which assess occupant protection in different crash scenarios.

1.1.2 Crash compatibility

Crash compatibility describes how different vehicles interact during a collision and how effectively they manage impact forces to protect occupants. Ideally, vehicles involved in a crash should have compatible structural stiffness, geometry, & load-path alignment, allowing forces to be distributed over a larger area and absorbed in a controlled manner. When these characteristics are well matched, the structures of both vehicles deform progressively, reducing peak loads and improving overall safety.

However, in real car-to-HGV crashes, large differences in mass, stiffness, and geometry often lead to poor interaction between the two vehicles. Based on the study on frontal crash incompatibility [7] as seen in Figure 1.2, the passenger car mainly contacts the FUPD and lower truck structures, while key load-bearing members are not properly aligned, limiting effective energy absorption and increasing intrusion. This structural mismatch is reflected in Figure 1.3, where the vehicle responses diverge significantly, with the passenger car experiencing a much higher and rapid velocity change compared to the truck. This shows that preventing underride alone is not enough—proper alignment of load paths and stiffness is also needed. For CAE barrier model development, it becomes important to represent these structural characteristics accurately so that vehicle interaction and deformation behaviour are captured more realistically.

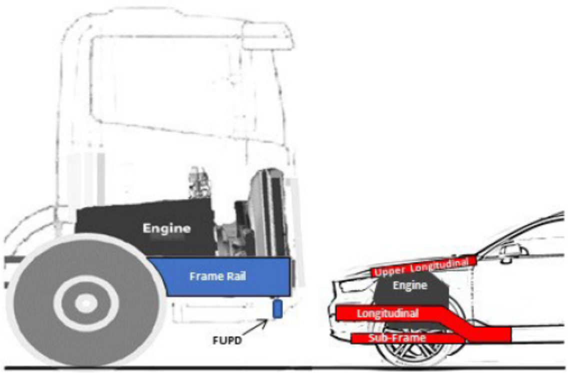

Figure 1.2: HGV-to-car compatibility[7]

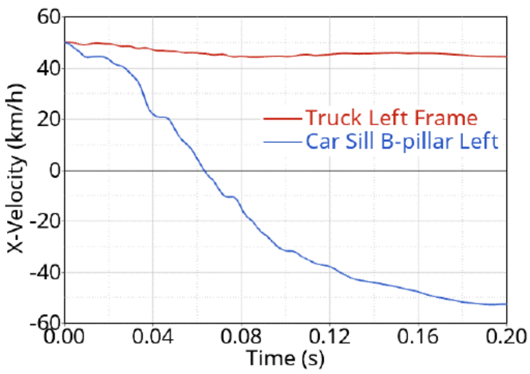

Figure 1.3: Velocity-time profiles for car and truck[7]

Theoretically, vehicle crash behaviour is primarily governed by the conversion of kinetic energy into deformation energy during an impact. The initial kinetic energy of a moving vehicle that must be dissipated through controlled deformation of structural components, is given by

$$E = \frac{1}{2}mv^2 \tag{1.1}$$

This process depends on the stiffness distribution and load paths within the vehicle, which determine how forces are transmitted and absorbed. Ideally, structures deform progressively, creating a stable crash pulse that reduces peak deceleration and allows safety systems to function effectively. At the same time, a balance is maintained between energy absorption in deformable zones and structural integrity of the passenger compartment, ensuring occupant protection during the collision.

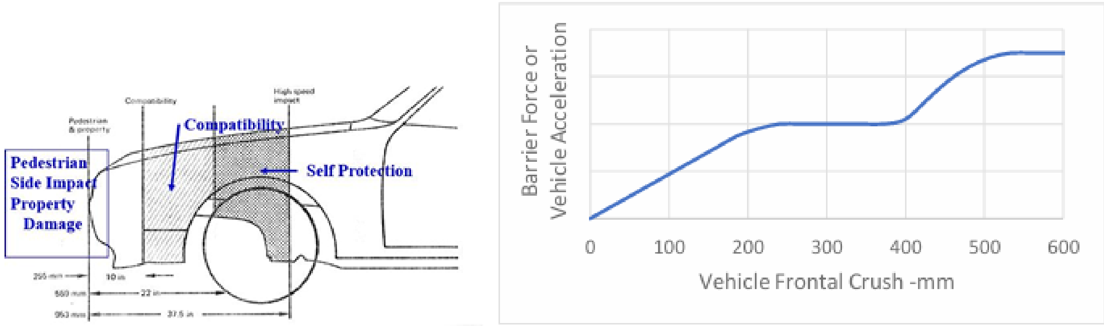

Figure 1.4: Vehicle frontal stiffness compatibility concept [8]

Figure 1.4 illustrates the concept of crash compatibility [8] through both structural alignment and force response. The left image shows the vehicle front structure, highlighting the vertical interaction region where key load-bearing members should align to enable effective load transfer during impact; misalignment in this region can lead to localized deformation and poor energy absorption. The right image shows the corresponding force–crush behaviour, where an initial plateau in the first 400 mm of crush represents controlled force levels for better compatibility, followed by a higher force region for occupant protection. Together, the figures emphasize that effective crash design requires both proper structural alignment and controlled stiffness behaviour to balance compatibility and self-protection.

1.1.3 Truck Front Underrun Protection Systems

Frontal crashes between passenger cars and HGVs are often severe due to significant differences in mass, structural stiffness, and geometry, which affect impact dynamics and load transfer. One of the main reasons is the large difference in weight, which results in much higher kinetic energy on the truck side and leads to a more severe crash pulse for the car occupants. Another issue is geometrical incompatibility, such as differences in front-end heights. Due to this mismatch, the car's front crash zones may not align properly with the truck, and in many cases the car can slide underneath, reducing its ability to absorb energy effectively [9].

To address this, Front Underrun Protection Systems (FUPS) are added to trucks to improve the interaction during a crash. These systems provide a lower contact area, so the car's front structures can engage more directly and start deforming as intended. The design of FUPS is controlled by UNECE Regulation R93 (ECE R93), which defines requirements for strength, geometry, and deformation under load. The main aim is to ensure that the structure remains effective during impact, providing a stable contact interface and preventing underride [4].

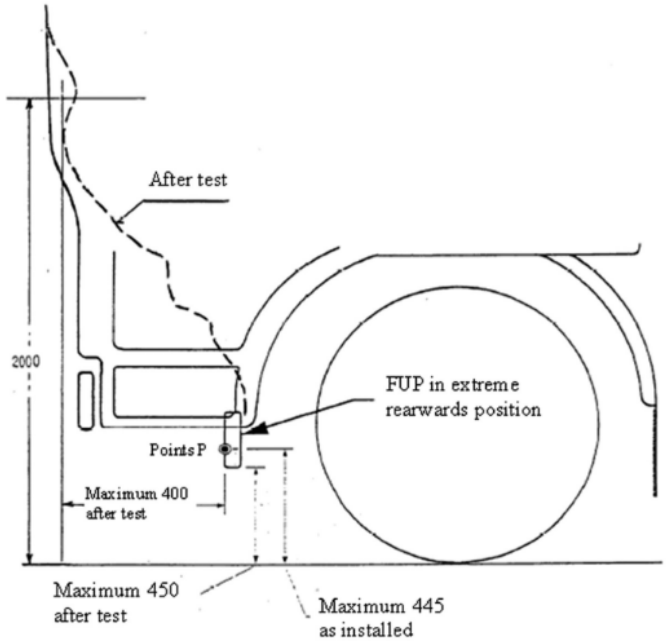

Figure 1.5: FUPS design as per UNECE R93 Regulation (Part III) - Addendum 92, Amendment 1 [4]

Figure 1.5 illustrates the deformation behaviour of a typical FUPS under prescribed regulatory loading, with a maximum allowable rearward displacement of 400 mm as defined in the amended UNECE Regulation R93 (Part III). In this update, the distance is measured in a vertical plane passing through the geometric centre of the test ram in its initial position, ensuring a consistent reference. Positioned ahead of the truck axle, the FUPS deforms rearwards under load while maintaining structural integrity, preventing underride and preserving a stable load-bearing interface for improved crash compatibility.

FUPS can be broadly classified into rigid and energy-absorbing systems (EA-FUPS); however, in practice, most designs combine both behaviours, as structural elements deform under load while still providing sufficient rigidity to prevent underride. While rigid systems offer basic protection, energy-absorbing designs improve compatibility by enabling more gradual force transfer and better stiffness matching during impact. Overall, FUPS help improve crash behaviour by promoting proper structural engagement and more controlled load transfer in car-to-truck collisions.

1.1.4 Euro NCAP Frontal Crash Test Procedures

To evaluate the safety performance of passenger vehicles in frontal collisions, Euro NCAP has developed standardized crash test procedures that simulate different real-world impact scenarios. The focus is not only on strength, but also on stiffness distribution, load paths, and deformation patterns, which influence the transfer of crash forces. In this context, the Mobile Progressive Deformable Barrier (MPDB) test [2] and the Full Width Rigid Barrier (FWRB) test [10], together provide a comprehensive view of vehicle crash behavior.

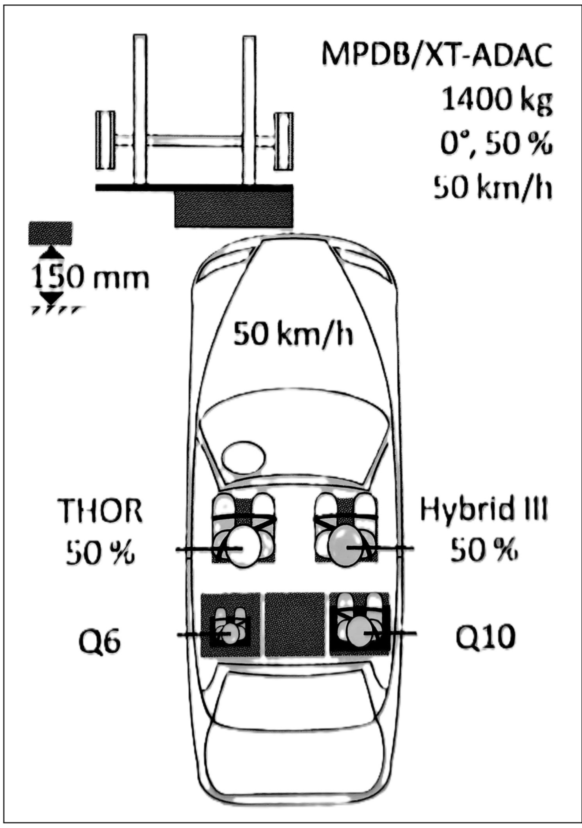

Figure 1.6: Euro-NCAP MPDB Test[2]

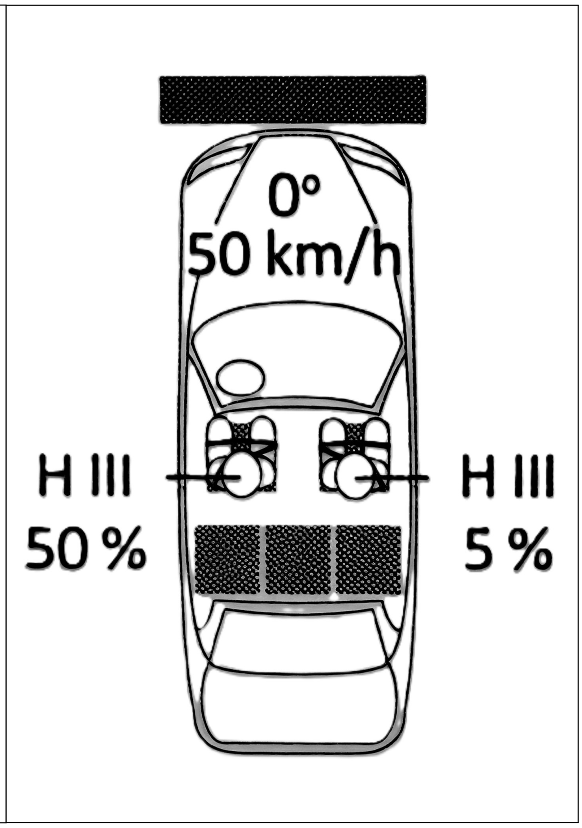

Figure 1.7: Euro-NCAP FWRB Test[10]

The MPDB test as shown in Figure 1.6 focuses on evaluating crash compatibility between vehicles. In this test, a vehicle collides with a moving deformable barrier at 50% overlap at the speed of 50 km/h, representing a car-to-car impact. The barrier has progressive stiffness to mimic a real vehicle front structure of a family car. The alignment of load paths and the distribution of forces across the contact area play a key role in the observed response. The barrier deformation pattern provides information on load spreading, indicating whether the force transfer is uniform or localized. At the same time, the force response of the barrier trolley is measured, allowing the calculation of parameters such as the Occupant Load Criterion (OLC)[13]. These results show the effect of vehicle stiffness and geometry on crash force distribution and overall compatibility performance.

The FWRB test as shown in Figure 1.7 isolates the structural behaviour of the vehicle during a full-width impact. Since the vehicle strikes a rigid barrier, all primary load paths are activated simultaneously, making it possible to assess the global stiffness and load transfer characteristics of the front structure. The resulting deceleration pulse reflects the overall stiffness and energy absorption behaviour, while the load distribution across the front structure indicates the effectiveness of structural engagement. Although interaction with another vehicle is not represented, the test provides useful information on intrinsic structural performance, which complements the findings from the MPDB test.

1.2 Previous studies

Several studies over the past decades have been investigating the frontal crash compatibility between different vehicle categories.

From 2003 to 2006, the study on improvement of VC-COMPAT (Vehicle Crash Compatibility) [3] through the development of crash test procedures focused on enhancing crash compatibility by developing more representative and reliable frontal impact test methods. It emphasizes the importance of evaluating both self-protection and partner-protection by considering how vehicles interact during a collision, rather than assessing them independently. The research highlights key factors such as load-path alignment, stiffness matching, and controlled deformation behavior as critical for reducing injury risks. It also supports the use of advanced deformable barrier concepts, which influenced later developments like the MPDB, designed to better represent real vehicle behavior in frontal impacts.

The FIMCAR project (Frontal IMpact and Compatibility Assessment Research) [11] during 2010 to 2013 aimed to improve frontal crash assessment by addressing limitations in existing evaluation methods, particularly in scenarios involving vehicles of different sizes and structural properties. The project also played a significant role in advancing barrier concepts influencing the development of the MPDB, to better mimic real vehicle structures. By emphasizing the importance of matching stiffness, ensuring proper load-path engagement, and achieving stable deformation, FIMCAR highlighted key requirements for improving both barrier design and truck safety systems. These findings reinforce the need for accurate identification of passenger car structural parameters, providing a strong foundation for developing realistic CAE-based surrogate barrier models.

Krusper and Thomson (2008) investigated crash compatibility between HGVs and passenger cars through both structural interaction analysis and in-depth accident studies, with a strong focus on the performance of FUPS [12]. The study showed that incompatibility in geometry and stiffness between vehicles often leads to ineffective engagement of car load paths, resulting in underride and severe occupant injuries. It highlighted that the effectiveness of FUPS depends not only on strength but also on proper alignment with passenger car structures and sufficient energy absorption capability. The findings emphasized the need for improved design and evaluation of FUPS by considering realistic vehicle structural characteristics. This work underlines the importance of accurately representing car front-end stiffness and load paths, supporting the development of more representative CAE barrier models for compatibility assessment.

Sandner and Ratzek (2015) introduced the MPDB [15] as an improved method for assessing frontal crash compatibility by better representing real passenger car behavior [13]. The study emphasized the importance of capturing progressive stiffness characteristics and realistic load distribution in barrier design to evaluate both self- and partner-protection in collisions. Key assessment parameters such as barrier deformation patterns and load transfer were shown to be closely linked to vehicle front-end structural properties. Compared to conventional barriers, the MPDB approach provides a more realistic representation of vehicle interaction during impact. This work highlights the need for accurately defining vehicle stiffness and load paths, forming a strong basis for identifying structural parameters in CAE barrier model development.

Park and Hor (2021) presented a CAE-based approach for assessing MPDB compatibility by introducing a virtual barrier deformation tracking method to efficiently evaluate barrier response in simulations [14]. The study addressed the challenge of high computational effort associated with detailed deformation modelling by developing a simplified technique that accurately captures barrier surface deformation and displacement patterns. This method enables reliable extraction of key compatibility metrics such as deformation depth and distribution without extensive element-level tracking, significantly reducing simulation time and computational cost. As a result, it allows faster and more efficient evaluation of multiple vehicle configurations during the design stage. The findings highlight that insufficient representation of stiffness distribution and deformation behaviour can lead to inaccurate compatibility assessment. Therefore, accurate modelling of these parameters is essential to ensure reliable prediction of vehicle interaction and to avoid misleading conclusions in CAE-based crash analysis.

2 AIM AND OBJECTIVES

The purpose of this project was to identify and quantify key structural parameters of passenger cars that influence their deformation behavior in frontal crashes and to translate these into stiffness-related inputs for developing a simplified CAE barrier model. Particular focus was given to capturing variations in structural characteristics associated with modern vehicle designs, ensuring that the resulting surrogate model provides a more representative description of the current and evolving passenger car fleet. This, in turn, supports improved compatibility assessment in HGV-to-car crash scenarios, as well as the development of safety systems such as the Front Underrun Protection Device (FUPD) [4].

To achieve this aim, the project focused on the following key objectives:

- Identify the key structural components defining the front-end architecture of passenger cars, such as longitudinal members, crash boxes, and subframes.
- Analyse variations within these components in terms of geometry, positioning, and stiffness characteristics.
- Translate the identified structural parameters into simplified stiffness representations suitable for CAE modelling.
- Develop a foundational dataset that supports the creation of a representative surrogate barrier model.
- Provide a basis for future work involving simulation-based validation of crash behaviour and load-path interactions.

3 METHODOLOGY

The study followed a stuctural appoach as presented in the flowchart below in Figure 3.1. The first step involved identifying and categorizing front-end structures across different car segments, followed by a comparative analysis to study the common load-path regions that must be represented in a surrogate barrier. Next, crash pulses obtained from frontal impact tests were analysed to understand energy absorption during collisions, linking structural layouts with actual crash behaviour. This combined structural and dynamic information was then translated into force-based inputs for barrier modelling. These inputs provide a basis for future barrier development and simulation to replicate vehicle behaviour and support crash compatibility assessment with heavy goods vehicles (HGVs), while the detailed design and validation of a complete barrier model remain outside the scope of this study.

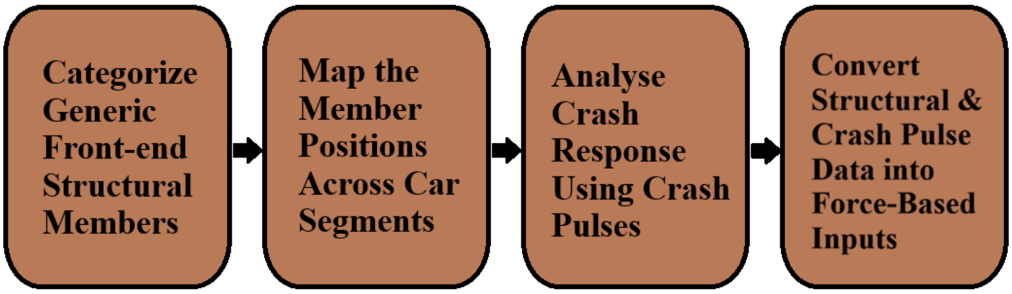

Figure 3.1: Flowchart for car structures identification for CAE barrier development

The structural assessment of vehicle components was conducted by accessing the CAD geometries using A2MAC1 software [25], while the post-processing of crash data was performed using MetaPost (Version 24.1.2) to analyse vehicle crash pulses. Furthermore, MATLAB (Version R2025b) was utilised to process force distribution, which serve as essential inputs for the development of the barrier model.

3.1 Categorize Generic Front-End Structural Members

3.1.1 Car database selection

In order to categorize generic front-end structural members of vehicles, a representative set of cars was defined to cover a wide range of structural designs, including different segments and manufacturers to provide a good representation of the European fleet. Therefore, a vehicle database was developed to map structural members through a structured selection process. Initially, cars were shortlisted based on their sales volume in the European market for the year 2025 [24], so that commonly used and relevant on-road vehicle segments were included. Other factors were also considered during selection, such as the visual appearance of the front structural layout, the availability of CAD models in the A2MAC1 database [25], and the safety performance of the vehicles based on the Euro NCAP ratings and their validity. This approach ensured that the selected dataset was both representative of current vehicle designs and supported by reliable data.

Item	Number of Cars
Top cars sold in EU for 2025	50
Cars selected based on structural analysis	15
Total cars shortlisted	65
ICE cars	15
HEV cars	15
BEV cars	15
Cars finalised based on available A2MAC1 CAD Data	**45**
5 star rated cars	37
4 star rated cars	3
3 star rated cars	4
2 star rated cars	1

Table 3.1: Summary of car database selection

Make	Model	Sales %	Make	Model	Sales %
Dacia	Sandero	1.83	Volvo	XC40	0.68
Volkswagen	T-Roc	1.61	Nissan	Juke	0.68
Volkswagen	Tiguan	1.49	Volkswagen	T-Cross	0.65
Volkswagen	Golf	1.49	Volvo	XC60	0.66
BMW	X1	1.42	Volvo	EX30	0.63
Peugeot	208	1.41	Fiat	500e	0.62
Dacia	Duster	1.29	Volkswagen	ID.3	0.60
Renault	Clio	1.29	Opel/Vauxhall	Mokka e	0.56
Citroën	C3 e	1.23	BMW	3-Series	0.54
Hyundai	Tucson	1.15	MG	3	0.41
Kia	Sportage	1.13	BMW	1-Series	0.35
Toyota	Yaris Cross	1.08	Cupra	Tavascan	0.27
Renault	Captur	1.04	Mazda	Mazda 3	0.18
Toyota	Yaris	0.95	Land Rover	Range Rover Evoque	0.17
Toyota	C-HR	0.88	BYD	Dolphin	0.09
Toyota	Corolla	0.86	Mercedes-Benz	EQE	0.072
Tesla	Model Y	0.83	Alfa Romeo	Giulia	0.025
Volkswagen	Polo	0.83	Audi	A8	0.015
Nissan	Qashqai	0.83	Mercedes-Benz	EQS SUV	0.014
Hyundai	Kona	0.76	Jaguar	I-Pace	0.013
Ford	Kuga	0.75	NIO	ET5	0.004
MINI	Cooper e	0.73	Jaguar	E-Pace	0.001
Jeep	Avenger	0.72			
	TOTAL			**32.84 %**	

Table 3.2: Distribution of vehicle sales percentage (2025) [24]

Table 3.1 presents the distribution of vehicles considered for categorisation. A total of 65 vehicles were initially considered, including 50 top-selling models and 15 additional cars chosen to capture different structural layouts. From this group, the vehicles were classified into Internal Combustion Engine (ICE), Hybrid Electric Vehicle (HEV), and Battery Electric Vehicle (BEV) categories, which were then taken forward for further review. Based on the availability of high-quality CAD data in A2MAC1 [25], the list was subsequently narrowed down to 45 vehicles for detailed analysis, with 15 vehicles selected from each category. Overall, the selected vehicles largely represented modern designs, many of which incorporated advanced safety features. This made the dataset suitable for studying structural behaviour and supported more reliable mapping of front-end load paths for crash-related analysis.

To better represent the European fleet, the dataset was weighted based on vehicle sales volume for 2025, as shown in Table 3.2. Even though the selected vehicles account for about 33% of total sales, they mainly include the most commonly sold models. This means the dataset still captures a significant portion of the active on-road fleet, while also covering a range of structural designs.

3.1.2 Categorization by geometric positioning

Categorization based on geometric positioning focused on identifying structural members according to their location within the front-end of the vehicle. Components were grouped vertically into upper, middle, and lower regions, and laterally into inboard and outboard zones. This helped in understanding how structural members are arranged across the front-end and highlighted differences between vehicles, particularly in the positioning of key load-carrying parts such as longitudinal rails and subframe structures.

Vertical positioning plays a key role in crash behaviour, with studies showing that vertical misalignment is a major cause of incompatibility in HGV–car crashes. From a recent study for frontal crash compatibility [7] as shown in Figure 3.2, there is a clear vertical mismatch between passenger cars and HGVs, where the car's main load-carrying structures (420–520 mm) do not align with those of the HGV (300–467 mm). This is further affected by sideways misalignment of structural members, which reduces proper contact during impact and leads to poor load transfer, lower energy absorption, and higher deformation.

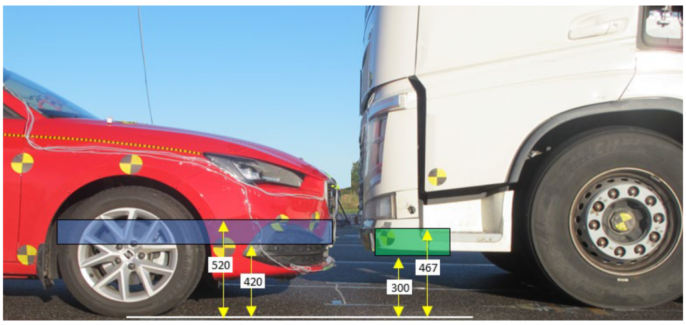

Figure 3.2: Truck-to-car frontal crash compatibility [7]

In addition to the vertical mismatch, differences in structural width and positioning can also affect how vehicles interact, although vertical alignment remains the main issue. In many cases, the car tends to underride the HGV, meaning its structure passes below the main load-carrying parts of the truck. This makes proper engagement difficult. Because of this, the design of the Front Underrun Protection Device (FUPD) becomes important, as it needs to be positioned correctly to allow the car's structures to interact effectively with the HGV. Better alignment can help improve load transfer and lead to more stable behavior during impact.

From a methodology perspective, analyzing geometric positioning is therefore essential for identifying common interaction zones between vehicles. This supports the mapping of stiffness distribution and provides a more realistic basis for developing surrogate barriers, ensuring that they capture the key vertical alignment effects observed in real-world crash scenarios.

3.1.3 Categorization by load path function

Categorizing front-end structural members based on load path function helped to understand how impact forces travel through the vehicle structure during a frontal crash. Instead of grouping components by their position, this approach classified them based on their role in carrying and absorbing loads. In earlier vehicle designs, there was usually a single main load path along the longitudinal rails, where most of the impact energy was carried through one route, often leading to poor load distribution and higher intrusion.

Over the years, vehicle structures have evolved to include multiple load paths—typically upper, middle, and lower—allowing forces to spread more evenly across the structure. Studies such as FIMCAR [11] have shown that the inclusion of additional paths, especially a lower load path, improves structural interaction during a frontal crash and leads to more stable deformation behaviour. As shown in Figure 3.3, the front-end structure was therefore considered using this multi-load-path approach to better represent crash energy management [15].

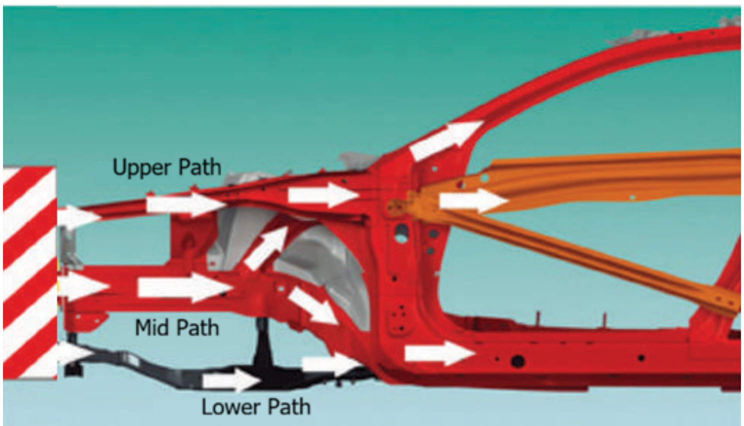

Figure 3.3: Car front-end structural interaction with multiple load paths during frontal crash against a full-width barrier (adapted from [15])

The mid (primary) load path, including crossbeams, crash boxes, and longitudinal members, carries a large share of the impact load and absorbs significant energy during the initial stages of impact. The upper load path, formed by shotguns and reinforcements connected to the A-pillar, adds stiffness and provides an alternative route for load transfer. The lower load path, which includes subframes and sill structures, helps direct loads towards the floor and rear of the vehicle, contributing to overall stiffness and load distribution.

Since these load paths act together during a crash, components often both absorb energy and transfer loads at the same time. Understanding how these paths interact and where they are located helped in identifying how stiffness is distributed at the front end. This, in turn, provided a useful basis for defining representative stiffness characteristics, which are essential for developing a realistic surrogate barrier for compatibility studies.

3.2 Map Member Positions across Car Fleet

3.2.1 Generalities & measurement standards

To ensure consistent mapping of structural member positions across different vehicle segments, all measurements were carried out using CAD data from the A2MAC1 database [25], following standardised procedures. As illustrated in Figure 3.4, a common vehicle coordinate system defined in A2MAC1 was used as the reference for all measurements, with the axes oriented along the $-X$, $-Y$, and $+Z$ directions ensuring consistency across different vehicles. This made it easier to locate and compare structural members across different vehicles, even with differences in size and design.

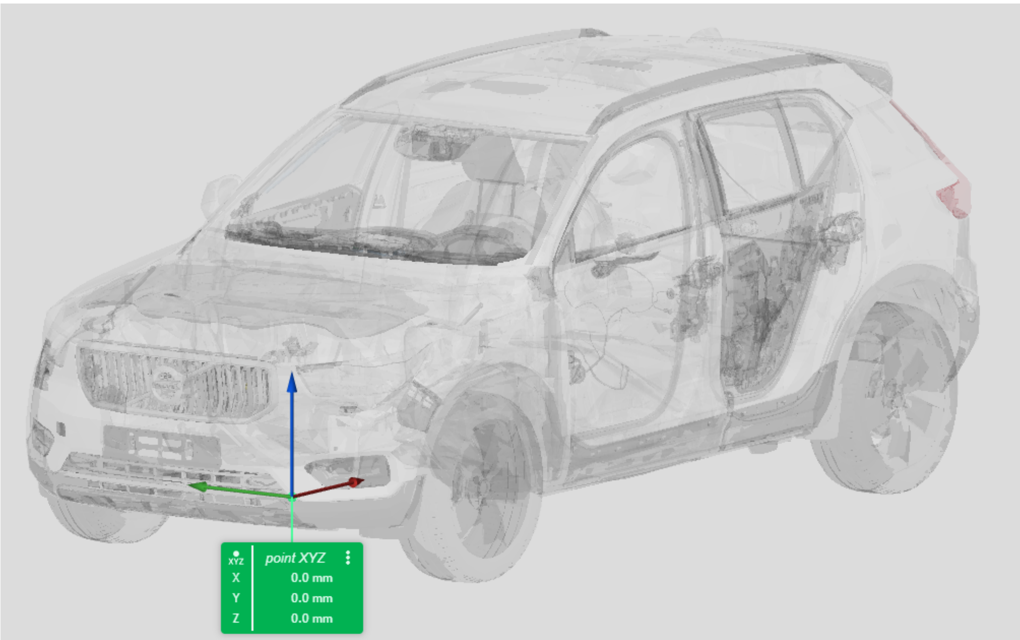

Figure 3.4: Vehicle Coordinate System in A2MAC1 [25]

For the geometric analysis, certain assumptions and conditions from the A2MAC1 database were followed. In the 3D AutoReverse process, all vehicle tanks are considered to be fully filled, and the unladen vehicle weight is taken from the documented teardown data without any additional load. For this study, the unladen mass was further adjusted to reflect occupant loading conditions specified in UNECE R94 [16], where dummies are present during experimental crash tests. An equivalent reference load corresponding to two occupants (80 kg each) was therefore added to align with VC-COMPAT data. In addition, the effect of the added occupant mass on vehicle geometry was accounted for. Based on literature [19] [20] [21], an increase in vehicle mass (+160 kg) can lead to a small reduction in ride height (approximately 10–15 mm per 100 kg), corresponding to a potential reduction of up to 20 mm, which was considered to have a limited influence on the geometric comparison.

3.2.2 Definition of car database

A detailed car structural database was created in an excel format that could help to understand the parameter measurements for different structural components involved in frontal crash of a car. The complete database can be found in the file:

EU Cars Database_2026.xlsx

The initial step in developing the database involved collecting the 'vehicle general information' for each car, arranged in decreasing order of EU sales volume for the year 2025, as listed below:
- Car make
- Car model
- Sales data (year 2025)
- Sales percentage
- EURO-NCAP safety star rating
- Year of test for EURO-NCAP frontal crash
- Year of model produced
- Segment
- ICEV/HEV/BEV
- SUV/Non-SUV
- Unladen Weight
- Length
- Width
- Height
- Wheelbase

Figure 3.5 shows the front and side views of the CAD model obtained for a representative car from the A2MAC1 database [25]. Based on these views, the front-end structural members can be described according to their position and role within the vehicle structure as followed:

- **Main rail & upper rail:** These are the main longitudinal members running along the vehicle front. They form the primary load paths and transfer impact forces rearwards into the occupant structure. The upper rail extends towards the A-pillar and contributes to upper load transfer & structural stiffness.

- **Bumper crossbeam & lower crossbeam:** The bumper crossbeam acts as the first transverse load-carrying member at the front, spreading impact forces across the width of the vehicle. The lower crossbeam supports additional load distribution at the lower level.
- **Crash can:** Positioned at the front and connected between the bumper crossbeam and main rail, it absorbs energy in the initial stages of impact through controlled deformation.
- **Subframe & subframe extension:** Located at the lower part of the structure, they support the lower load path and help transfer loads into the floor and underbody structure.

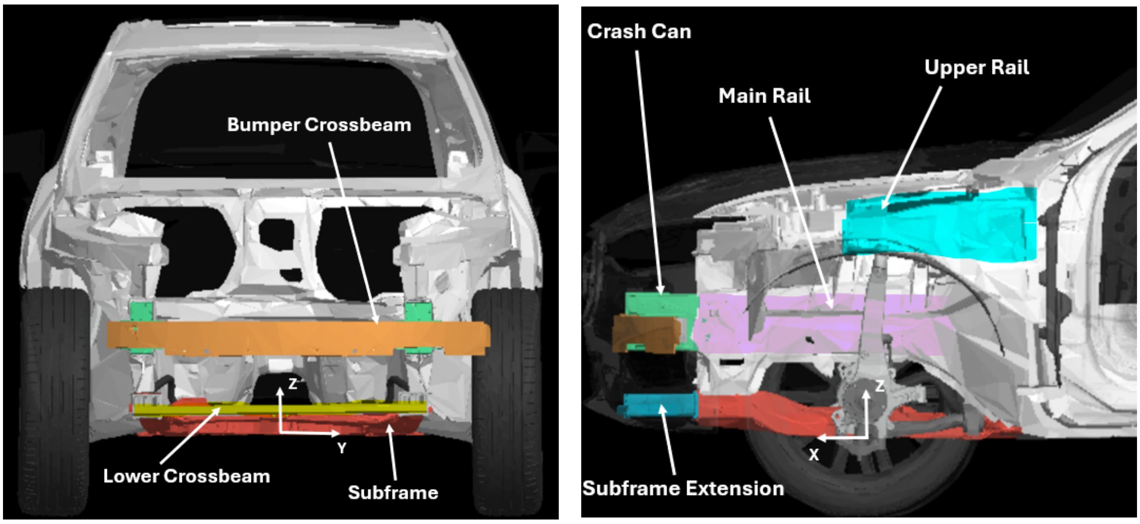

Figure 3.5: Front & Side views of car with nomenclature for front-end structural members [25]

For the 'vehicle front unit measurements', Table A.1 in the appendix lists the column abbreviations used in the Excel database for the corresponding structural components. The measurement methodology is illustrated in figures A.1 to A.6 in appendix A.1. Based on this, the following key geometric parameters were extracted for the structural analysis database:

- **Section Height:** The cross-sectional dimension in the vertical direction, measured with respect to the ground reference. This parameter was recorded for all structural components.
- **Section Width :** The cross-sectional dimension in the transverse direction, measured with respect to the vehicle centreline. This was recorded only for the upper and lower rails, as their lateral positioning significantly influences structural interaction and the distribution and absorption of crash energy.
- **Section Length:** The cross-sectional length in the longitudinal direction, measured with respect to the front wheel centre point. This parameter was recorded for all components.

3.2.3 Data analysis of geometric measurements

The aim of this analysis was to understand the range and spread of load path regions using the collected geometric measurements. For each structural element, following set of basic statistical values was calculated to capture how these dimensions vary across the selected vehicles, while also reflecting typical characteristics of the European fleet:

- Min: Minimum value measured
- Max: Maximum value measured
- Delta: Difference between maximum and minimum values
- Mean: Average value calculated across the 45 vehicles
- Weighted Mean: Average value calculated by weighting the data based on vehicle sales volume

In addition to these statistical measures, the distribution of section heights & widths for key structural components was shown using whisker plots (10–90% range). This helped in representing the spread of data while avoiding the effect of outliers, giving a more realistic view of how structures are positioned across the fleet. Also, weighted delta values were given more importance so that commonly sold vehicles have a greater influence on the results.

3.3 Analyse Crash Response using Crash Pulses

Analysis of the crash pulse data was carried out to understand vehicle response during frontal impacts and to derive inputs for stiffness modelling. A typical crash pulse represents the deceleration–time history of a vehicle and reflects how the front structure absorbs and manages crash energy. As shown in Figure 3.6, the pulse drops sharply during the initial phase of impact due to front-end deformation, reaches a peak, and then gradually stabilizes as the load is transferred through the structure and the vehicle comes to rest. In this study, crash pulses were used to relate structural behaviour with energy absorption characteristics.

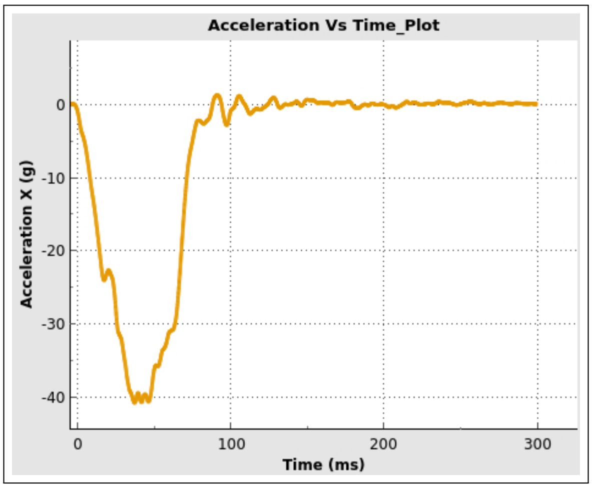

Figure 3.6: Vehicle Crash Pulse obtained from Euro NCAP MPDB/FWRB tests

Crash pulse data was obtained from standardized frontal crash tests, including Euro-NCAP MPDB and FWRB tests. The acceleration signals were measured using accelerometers, typically at the vehicle COG (centre of gravity) for MPDB and at the B-pillar locations on both sides of the vehicle. For the target vehicle, acceleration signals from both sides were averaged to obtain a representative response.

For the analysis, the vehicle mass was considered as the dynamic test mass, which consists of the unladen kerb weight along with reference loads defined in Euro-NCAP test protocols [10]. These reference loads include two adult occupants in the front row (80 kg each), additional mass in the luggage compartment (50 kg), and two child dummies in the second row (23 kg and 36 kg). This combined mass better represents real test conditions and was used for force calculations in the analysis.

The recorded acceleration–time histories were then filtered using appropriate crash filtering classes (SAE J211 CFC filters) to ensure consistency across different datasets [17]. From these filtered signals, key parameters such as peak deceleration, rise time, pulse duration, and pulse shape were identified, providing information on structural stiffness and energy absorption behavior. All parameters were initially processed in SI units. For the final plots, the units were converted to force (kN), acceleration (g), velocity (km/h), displacement (mm), and time (ms) for easier interpretation.

The processed acceleration data was further analysed in a stepwise manner using Metapost post-processing software to derive additional response characteristics:

- **Acceleration–time response** (A_x–t): Raw acceleration signals were filtered using a CFC60 filter to remove noise while retaining essential crash response.
- **Velocity–time response** ($V_x - t$): The filtered acceleration data was integrated to obtain velocity–time histories. Since the crash tests are conducted at a standard impact speed of 50 km/h, the velocity curve was shifted such that the initial velocity corresponds to this impact speed. A CFC180 filter was applied to smooth the signal.
- **Displacement–time response** ($D_x - t$): The velocity–time data was further integrated to obtain displacement–time behaviour using a CFC180 filter.
- **Force–time response** ($F_x - t$): The force response was calculated by scaling acceleration with the vehicle's dynamic test mass defined above. For MPDB barrier analysis, a representative mass of 1400 kg was used.
- **Force–displacement behaviour** (F_x–D_x): Derived by combining force–time and displacement–time data, representing stiffness and energy absorption characteristics.
- **Acceleration–displacement behaviour** ($A_x - D_x$): Obtained by relating acceleration and displacement data to further analyse structural response.

The same post-processing approach was applied across all selected vehicles and test configurations and averaged responses were used to study the overall response to crashes. Representative plots for an individual vehicle and averaged responses are presented in the Results section to illustrate the derived crash behavior.

From the derived results, force–displacement characteristics were obtained for both vehicle and barrier systems, forming the key input for defining stiffness used in subsequent barrier modelling. Overall, the crash pulse analysis provided a direct link between measured crash behaviour and the simplified stiffness representation required for surrogate barrier development.

3.4 Convert Structural & Crash Pulse Data into Force-Based Inputs

This stage focused on converting the structural response of vehicles and processed crash pulse data into a spatial force distribution across the MPDB barrier. The flowchart in Figure 3.7 shows how multiple data sources—namely crash pulse behavior, barrier deformation data, and structural load path information—were combined to obtain representative stiffness characteristics for the barrier model.

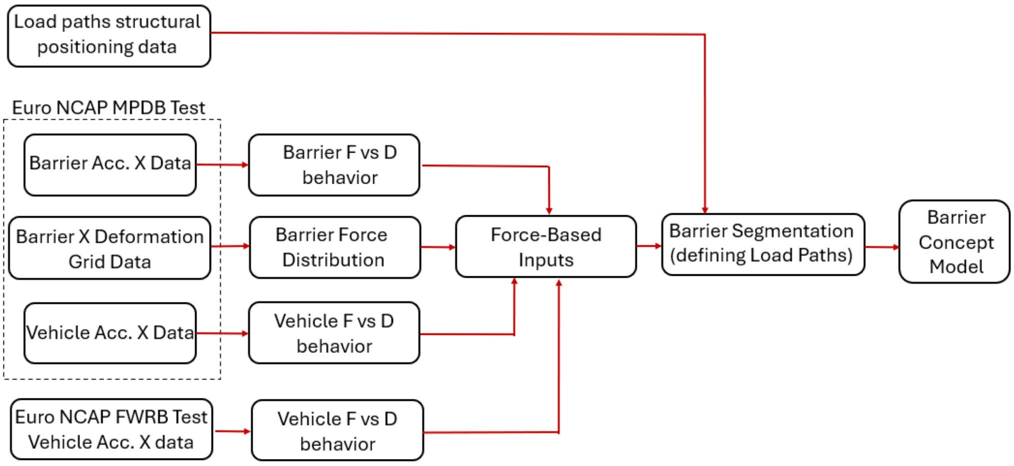

Figure 3.7: Barrier concept model development flowchart

The process began with the use of previously derived force–displacement (F–D) behaviour for the target vehicle. The peak force obtained from these curves was used as a reference to represent the overall crash response during impact [3]. However, as this represents only the global response, additional steps were required to distribute this force across the barrier surface.

To address this, deformation data from the Euro NCAP MPDB test was analysed in detail. In this test, vehicle–barrier interaction is evaluated over a defined rating area on the front-end, covering approximately 45% of the vehicle width on the struck side (Figure 3.8) [2]. The coloured grid represents the distribution of deformation across the barrier surface. Regions with higher deformation indicate stronger structural engagement and energy absorption, while lower deformation corresponds to relatively stiff or less engaged areas. The assessment is based on how uniformly this deformation is distributed, reflecting the effectiveness of load transfer through different structural members.

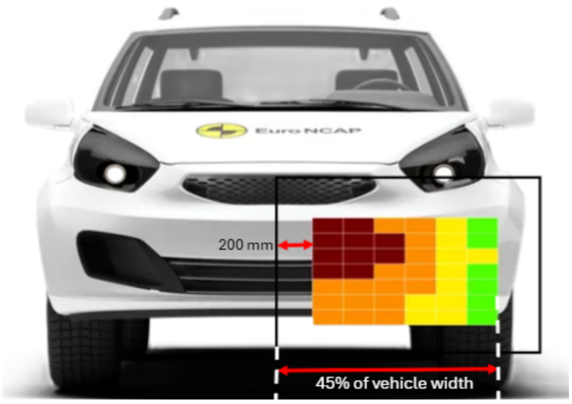

Figure 3.8: MPDB rating assessment area [24]

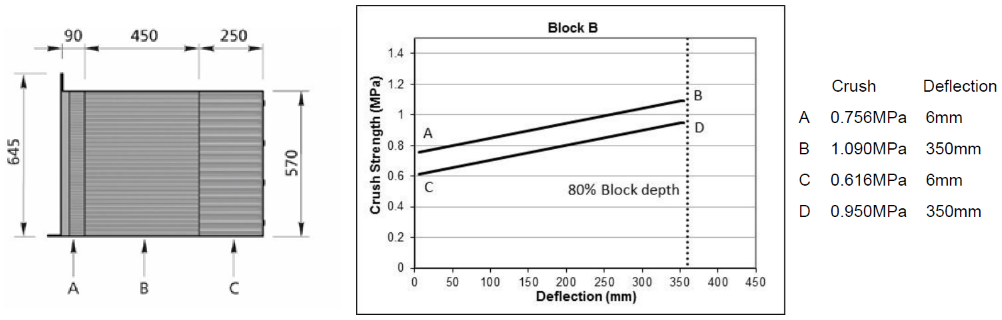

Figure 3.9: MPDB blocks static corridor [2]

In this study, the MPDB deformation data was available as a grid consisting of approximately 1400 measurement points across the barrier face. This grid captured the local crushing behaviour of the honeycomb structure during impact and formed the basis for further processing.

The MPDB barrier is composed of three distinct regions—blocks A, B, & C—each with different crush characteristics, as shown in Figure 3.9 [2]. Blocks A & C consist of homogeneous honeycomb structures with nearly constant crush strength values, typically in the range of 1.54–1.71 MPa for block A & 0.30–0.34 MPa for block C. For the present analysis, mean values within these ranges were used for each block. In contrast, block B is designed as a progressively deformable region with deformation-dependent crush strength defined by a static corridor, enabling the barrier to replicate progressive energy absorption behaviour of real vehicle structures.

Based on the MPDB deformation data, the crush strength at each grid point was determined as a function of local deformation. For deformation values up to 250 mm, the crush strength corresponds to block C with nearly constant values. Between 250 mm and 700 mm, the crush strength varies linearly within block B according to the defined static corridor. Beyond 700 mm, the crush strength is assumed to be constant and equal to that of block A.

Since the crush strength varies with deformation, the energy absorbed at each grid cell was calculated by integrating the contribution across the deformation range. The energy absorbed within each region was determined individually and then summed to obtain the total energy corresponding to the deformation at that cell.

The energy contribution can be expressed as:

$$E = \sum(\sigma_c \cdot A \cdot \Delta\delta) \tag{3.1}$$

where σ_c is the crush strength corresponding to the deformation range, A is the cell area (20 × 20 mm), and $\Delta\delta$ is the deformation increment within each region.
The total energy for a given deformation δ is therefore obtained by summing the contributions from blocks C, B, and A:

$$E_{\text{total}} = E_C + E_B + E_A \tag{3.2}$$

The local force at each grid cell was then calculated using the relation:

$$F = \frac{E_{\text{total}}}{\delta} \tag{3.3}$$

This approach accounts for the progressive crush behaviour of the MPDB barrier, ensuring that the force calculation reflects the variation in deformation-dependent crush characteristics.

The resulting force distribution represents the local response of the barrier based on its deformation behaviour. To represent the actual vehicle–barrier interaction, the global peak force obtained from the target vehicle force–displacement response during the MPDB test was distributed across the barrier surface using this derived force pattern.

A force distribution factor was defined for each cell:

$$\text{Factor}_i = \frac{F_{i,\text{theoretical}}}{\sum F_{\text{theoretical}}} \tag{3.4}$$

where Factor_i is the force distribution factor at cell i, $F_{i,\text{theoretical}}$ is the theoretical force at cell i, and $\sum F_{\text{theoretical}}$ is the total theoretical force summed over all grid cells.

The localised force at each cell was then calculated as:

$$F_{i,\text{actual}} = F_{\max} \times \text{Factor}_i \tag{3.5}$$

where $F_{i,\text{actual}}$ is the localised force at cell i, $F_{\max}$ is the maximum force obtained from the vehicle force–displacement response, and Factor_i is the force distribution factor at cell i.

This approach ensures that the global crash load is distributed across the barrier surface based on deformation-dependent force characteristics derived from the MPDB structure, providing a physically consistent representation of vehicle–barrier interaction.

MATLAB was used to process the deformation data and generate spatial force distributions across the barrier surface. Representative derived force distribution heatmaps along with averaged results across the selected dataset, are presented in the Results section (Figures 4.15 to 4.20) to illustrate this distribution.

The same procedure was applied to a selected set of seven vehicles, chosen based on their structural characteristics and representation within the European fleet. The resulting force distributions were averaged to obtain a generalised trend, reducing the influence of individual vehicle variations. To simplify further analysis, the original deformation grid (28 $\times$ 50 cells, 1400 points) was reduced to a coarser 7 $\times$ 10 grid. Each cell in the reduced grid represents the averaged value of corresponding region, preserving overall distribution pattern while reducing data complexity.

The processed, energy-derived force distribution maps were then compared with the geometric positioning of structural components such as upper rails, main rails, and cross-members. By overlapping the force distribution with section height data, regions of higher and lower load concentration were identified. These variations indicate differences in load transfer and form the basis for defining distinct load path regions within the barrier.

Due to limitations in data availability and time, the analysis was restricted to force distribution, and further processing required to obtain consistent stiffness-based representations could not be completed. As a result, a segmentation based on force distribution trends combined with structural positioning was proposed.

Despite these limitations, the approach demonstrates how crash pulse data and barrier deformation characteristics can be translated into a deformation-dependent force distribution. When combined with the geometric positioning of key load-carrying components, this force distribution provides a practical basis for identifying load path regions across the barrier. These variations in load transfer highlight the potential for segmenting the barrier into distinct zones corresponding to different structural interactions.

In a complete approach, this segmentation would be further refined by incorporating stiffness characteristics within each region to better represent the mechanical behaviour of the structure. This would allow the barrier to capture both the overall crash response and local structural interaction more accurately.

Overall, the methodology establishes a structured framework for progressing from crash response data to a segmented barrier concept. It also defines a clear direction for future work, including stiffness mapping, model refinement, and CAE-based validation for a more representative barrier model.

4 RESULTS

This section outline results of the current study, focusing on kerb weight updates and structural configuration of the selected car dataset. A summary of key geometric parameters, including section heights, widths, and lengths, is presented to describe positioning of the frontal structural components of the car. Furthermore, crash response analysis and the distribution of force and stiffness are reported to assess structural behavior under loading conditions during frontal impact.

A general review of the selected vehicle dataset shows that, although hatchbacks form a significant portion of the sample, their kerb weights remain relatively high. This trend can be attributed to the increasing integration of electrified powertrains and associated subsystems, which contribute to overall vehicle mass. In addition, an overall increase in vehicle ride height is observed across the dataset. This can be linked to two main factors: the growing market preference for SUV-type vehicles, and the need to accommodate battery packs or hybrid drivetrain components in electrified vehicles.

Several distinctive structural configurations were identified across individual vehicles in the dataset:

- Dacia Sandero (2-star safety rated) and Dacia Duster (3-star safety rated) do not have a clearly defined crash can in the front structure.
- Volvo XC60 uses an asymmetric upper cross-member along with a shock guide system.
- BYD Dolphin (5-star safety rated) features a double crash-can arrangement along the mid load path, indicating improved energy absorption.
- Range Rover Evoque shows variation in upper rail height, suggesting uneven load distribution.
- Mercedes EQE & EQS use double main rails with larger section heights, contributing to increased stiffness.
- Tesla Model Y does not have a distinct upper rail (shotgun), as its function is combined with the main rail.
- In many BEVs, the upper rail is integrated into the main rail instead of being a separate component.
- Additional reinforcements are commonly observed across the cooling frame, especially in BEV vehicles.

4.1 Kerb Weights of car fleet

Figure 4.1 presents the kerb weight distribution of EU passenger car models by powertrain type (ICEV, HEV, BEV). A clear separation in average kerb weights is observed, with BEVs showing the highest mean (1973 kg), followed by HEVs (1700 kg), and ICEVs (1544 kg), while the overall fleet average is around 1739 kg. To align with the VC-COMPAT dataset, kerb weight was calculated by adding the mass of two occupants (80 kg each, based on Hybrid III 50th percentile male dummies) to the EURO-NCAP unladen weight in line with ECE R94 requirements.

Table 4.1 summarises the kerb weight values along with weighting factors derived from vehicle sales distribution. In the VC-COMPAT study (2008), only ICEVs were considered, accounting for 61% of the fleet. In contrast, the current A2MAC1 dataset reflects a more recent market distribution, where ICEVs account for 33% (mainly hatchbacks), and electrified vehicles comprising (HEV: 12% & BEV: 7%).

Based on these weighting factors, the contribution of ICEVs in the current dataset results in a weighted mass of 1412 kg, which is lower than the 1428 kg observed in the VC-COMPAT study. However, significantly higher values for HEVs (1676 kg) and BEVs (1744 kg) increase the overall weighted mass to 1592 kg. This represents an increase of approximately 200 kg compared to the VC-COMPAT dataset.

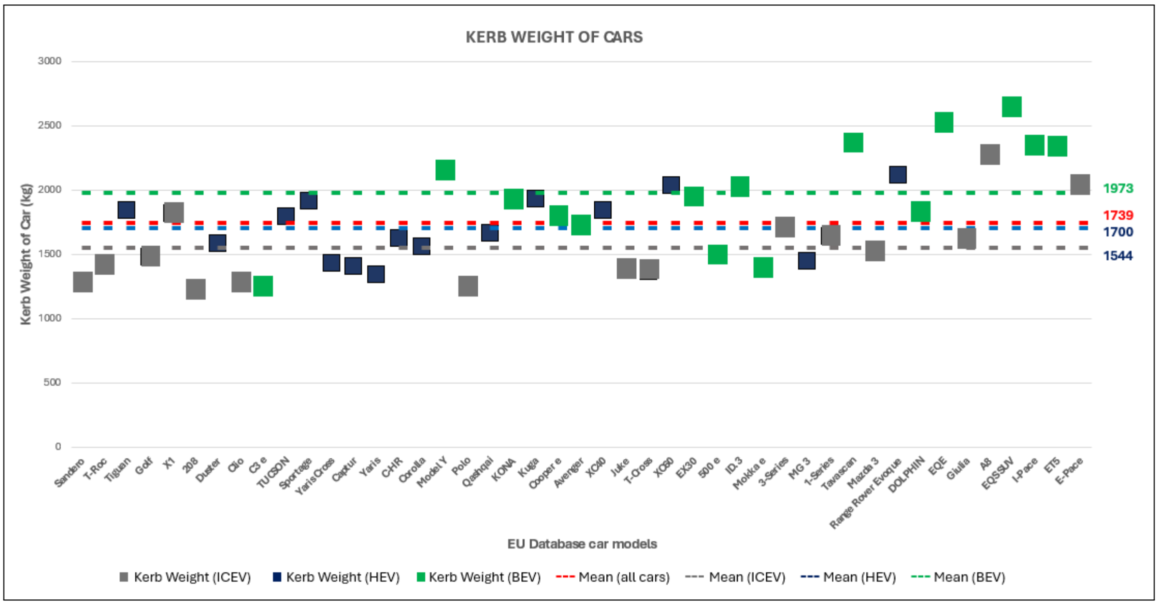

Figure 4.1: Kerb Weight of Cars

Study	**VC-COMPAT**	**A2MAC1**			
Car Type	ICEV	ALL CARS	ICEV	HEV	BEV
Kerb Weight (kg)	1591	1739	1544	1700	1973
Weighting Factor (%)	61	33	12	13	7
Weighted Mass (kg)	1428	1592	1412	1676	1744

Table 4.1: Kerb Weight Comparison - VC-COMPAT vs A2MAC1

4.2 Positioning of Car Structural Components

4.2.1 Section Heights

The following figures present the distribution of section heights for key structural components across all vehicles. Whisker plots (10–90% range) are used to represent data spread while minimizing outlier effects. Weighted delta values are prioritized, with greater significance assigned based on sales. In addition, the previously applied increase in vehicle mass (+160 kg) is expected to result in a small reduction in ride height, estimated to be up to 20 mm based on literature [19] [20] [21] (10–15 mm per 100 kg). However, this reduction is relatively small compared to the differences observed in section heights between the datasets. Detailed height distribution plots for individual structural components are provided in Appendix A.2 for reference.

Figure 4.2 shows the positioning of frontal structural components relative to the MPDB assessment limits. The upper load path (upper rail) lies above the upper boundary, with a weighted mean height of approximately 816–818 mm. Mid load path components, including the bumper crossbeam, crash can, and main rail, are positioned near the upper limit, ranging between 540 mm and 552 mm. In contrast, lower components such as the lower crossbeam, subframe extension, and subframe lie close to or below the lower boundary, typically between 250 mm and 302 mm. The front tire centre is located at a weighted mean height of approximately 340 mm.

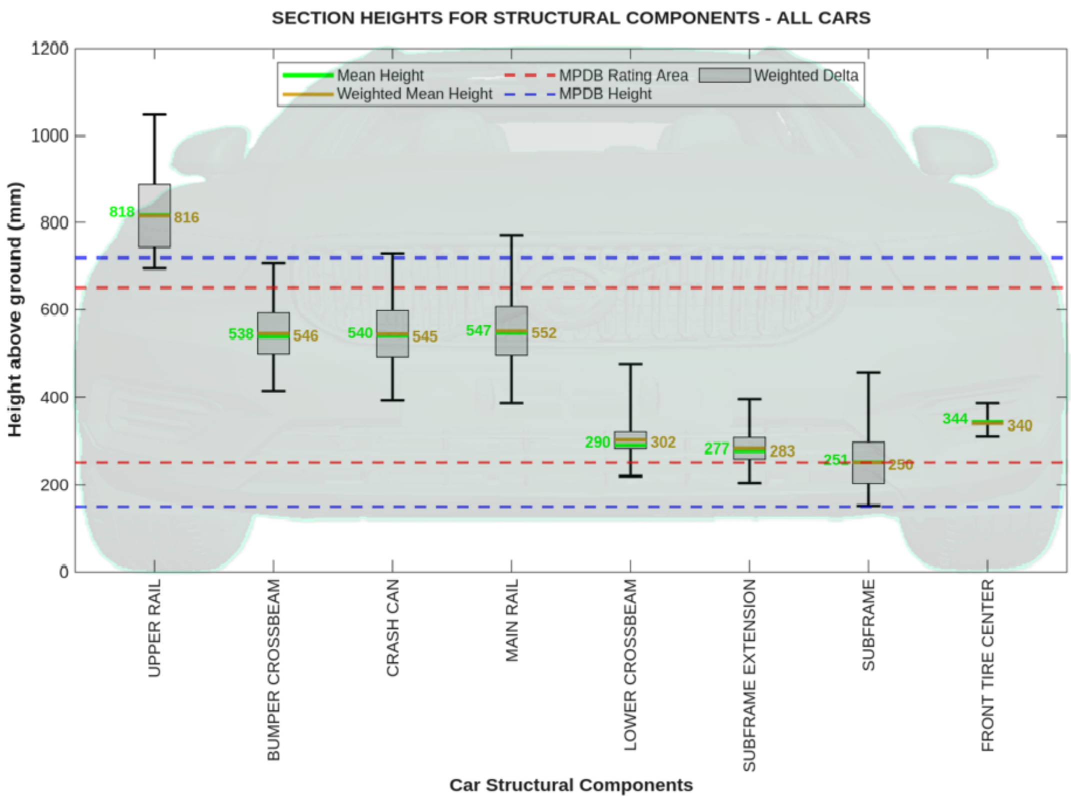

Figure 4.2: Section Height for structural components [25]

Figure 4.3 presents a comparison of section heights between the VC-COMPAT study and the current dataset (A2MAC1 – measured), based on weighted delta values. The measured dataset shows higher values across all components, with the front tyre centre, main rail, and bumper crossbeam positioned above the earlier dataset. The subframe is also higher, while the upper rail shows the highest values in both cases. The actual A2MAC1 case, considering a 20 mm reduction in ride height, shows a downward shift across all components; however, the positions remain noticeably higher compared to the earlier dataset.

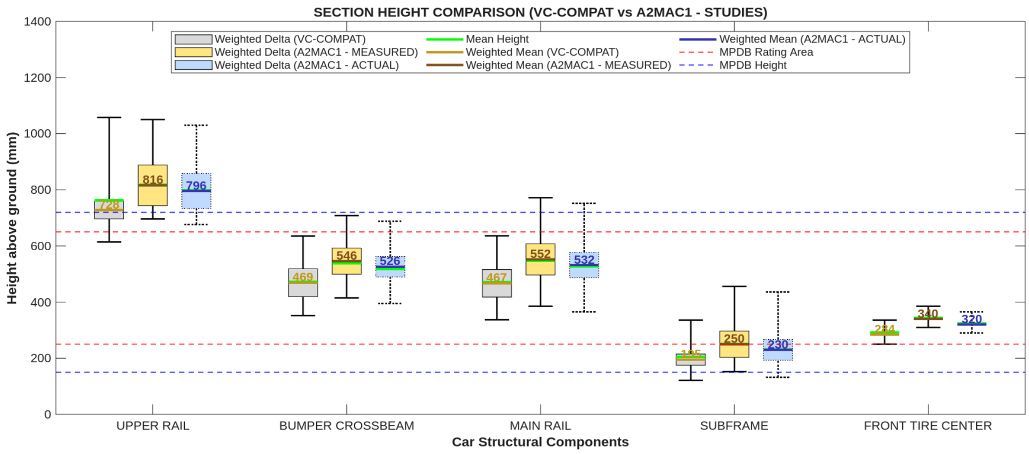

Figure 4.3: Section height comparison - VC-COMPAT vs A2MAC1

Figure 4.4 presents the distribution of section heights across ICEV, HEV, & BEV fleets using weighted delta values. The mid-level components, including bumper crossbeam, crash can, and main rail, show noticeable differences, with HEV positioned higher (550–560 mm) compared to ICEV and BEV (530–545 mm). The subframe also varies, with BEV reaching higher values (260 mm) than ICEV (245 mm). The lower components (lower crossbeam, subframe extension) lie within a narrow range (290–300 mm), showing smaller variation. The upper rail remains highest (830–845 mm), while front tire centre shows limited variation (330–350 mm).

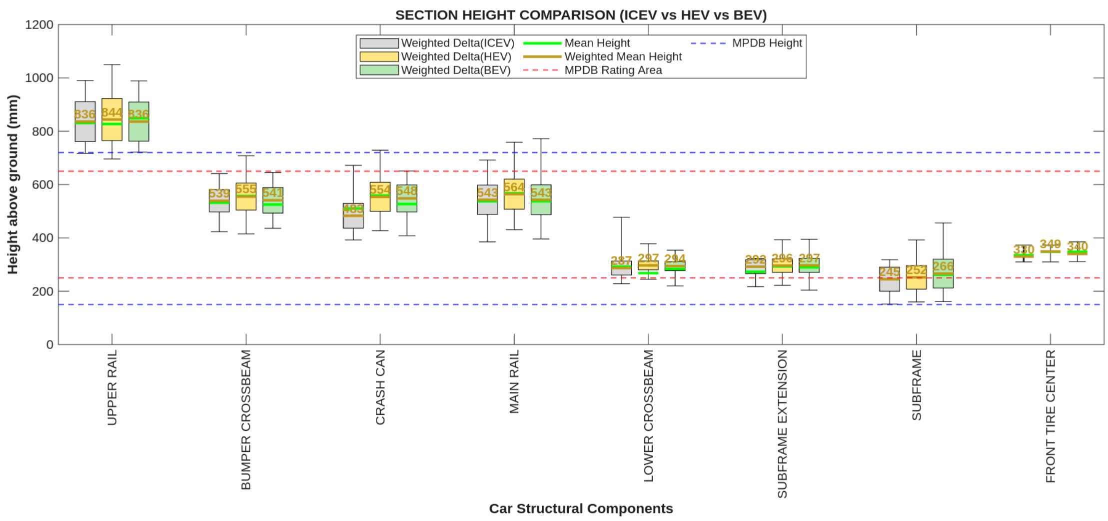

Figure 4.4: Section height comparison - ICEV vs HEV vs BEV

4.2.2 Section Widths

The figures in this section present the distribution of section widths for key structural components involved in frontal impact (rails/longitudinals) across all vehicles, using 10–90% whisker plots and weighted delta values to reflect sales-based significance. It should be noted that the additional vehicle mass considered in the analysis does not affect section widths, since these are fixed geometric properties. Detailed width distribution plots for individual structural components are provided in Appendix A.3 for reference.

Figure 4.5 presents the distribution of section widths across all vehicles. The main rails show weighted mean widths of approximately 478 mm, while the subframe extensions lie within a similar range, with values around 469–490 mm. The distributions are symmetric about the vehicle centreline, as observed from similar values on the left and right sides. The spread indicated by the whisker range shows moderate variation for both components. The positioning of the rails lies within the MPDB assessment limits, with most values falling inside the defined interaction zone, corresponding to approximately 45% of the vehicle width.

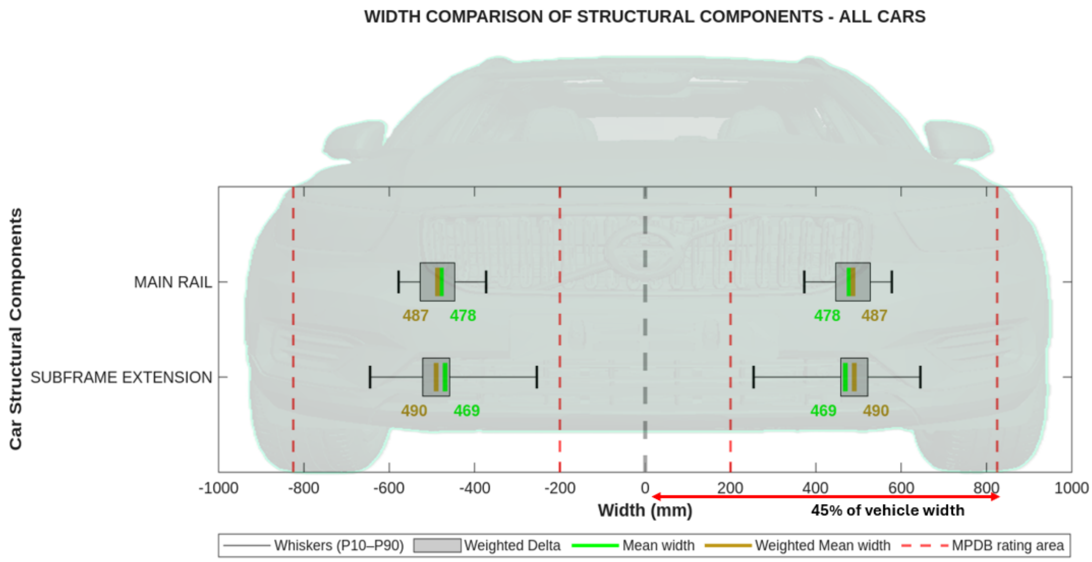

Figure 4.5: Section width for structural components [25]

Figure 4.6 presents the distribution of section widths for main rails & subframe extensions across ICEV, HEV, and BEV datasets using weighted delta values. The main rails show comparable weighted mean widths across all powertrains, with values around 465 mm for BEV and 487 mm for both HEV and ICEV. For the subframe extensions, HEV exhibits the highest weighted mean width at approximately 511 mm, while BEV and ICEV show lower values around 475 mm and 469 mm, respectively. The spread of values, indicated by the whisker range, is broader for the extensions compared to the main rails. The distributions remain symmetric about the vehicle centerline, and all values lie within the MPDB assessment limits.

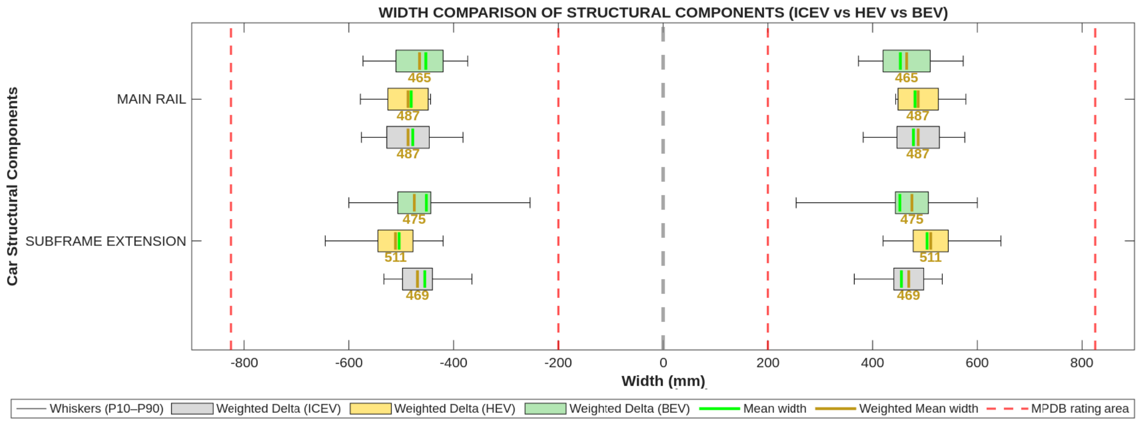

Figure 4.6: Section width comparison - ICEV vs HEV vs BEV

4.2.3 Section Lengths

Figure 4.7 presents the longitudinal placement of key structural components across all vehicles, referenced to the front tire (axle) centreline, showing the forward-most extent of each component along with its variation. The main rail and lower cross-beam extend furthest forward, reaching approximately 750–800 mm, followed by the bumper crossbeam and crash can, which lie within the front interaction region around 650–750 mm. In comparison, the subframe and subframe extension show intermediate forward reach (500–700 mm), while the upper rail remains closer to the axle (150–250 mm). Overall, the forward placement varies across components, with some members extending deeper into the front structure and others concentrated near the impact region. Detailed length distribution plots for individual structural components are provided in Appendix A.4 for reference.

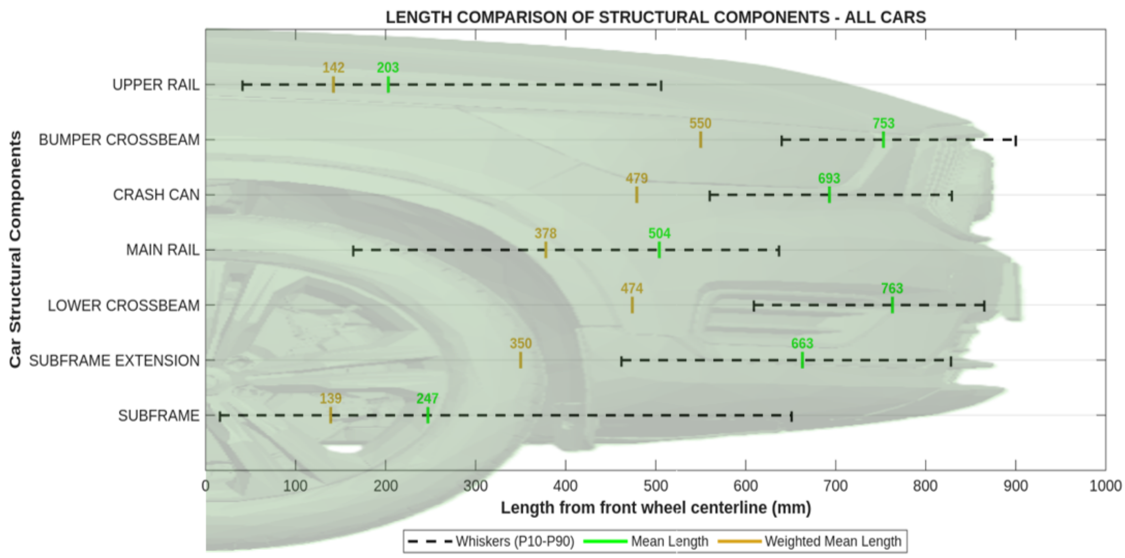

Figure 4.7: Section length comparison for structural components [25]

4.3 Crash Response Analysis

Figure 4.8 shows the crash response characteristics for a representative car. The plots include acceleration–time (A_x–t), velocity–time (V_x–t), displacement–time (D_x–t), force–time (F_x–t), force–displacement (F_x–D_x), and acceleration–displacement (A_x–D_x) responses. For each plot, three curves are presented: MPDB barrier response, MPDB target vehicle response, and FWRB vehicle response. Across all responses, consistent trends are observed between configurations. The MPDB barrier shows a sharper deceleration peak and higher force levels, while the FWRB response is comparatively smoother with slightly higher displacement. These differences are reflected in the derived force–displacement characteristics, where the MPDB barrier exhibits higher stiffness with greater force at lower displacements, compared to the more gradual response seen in the vehicle configurations.

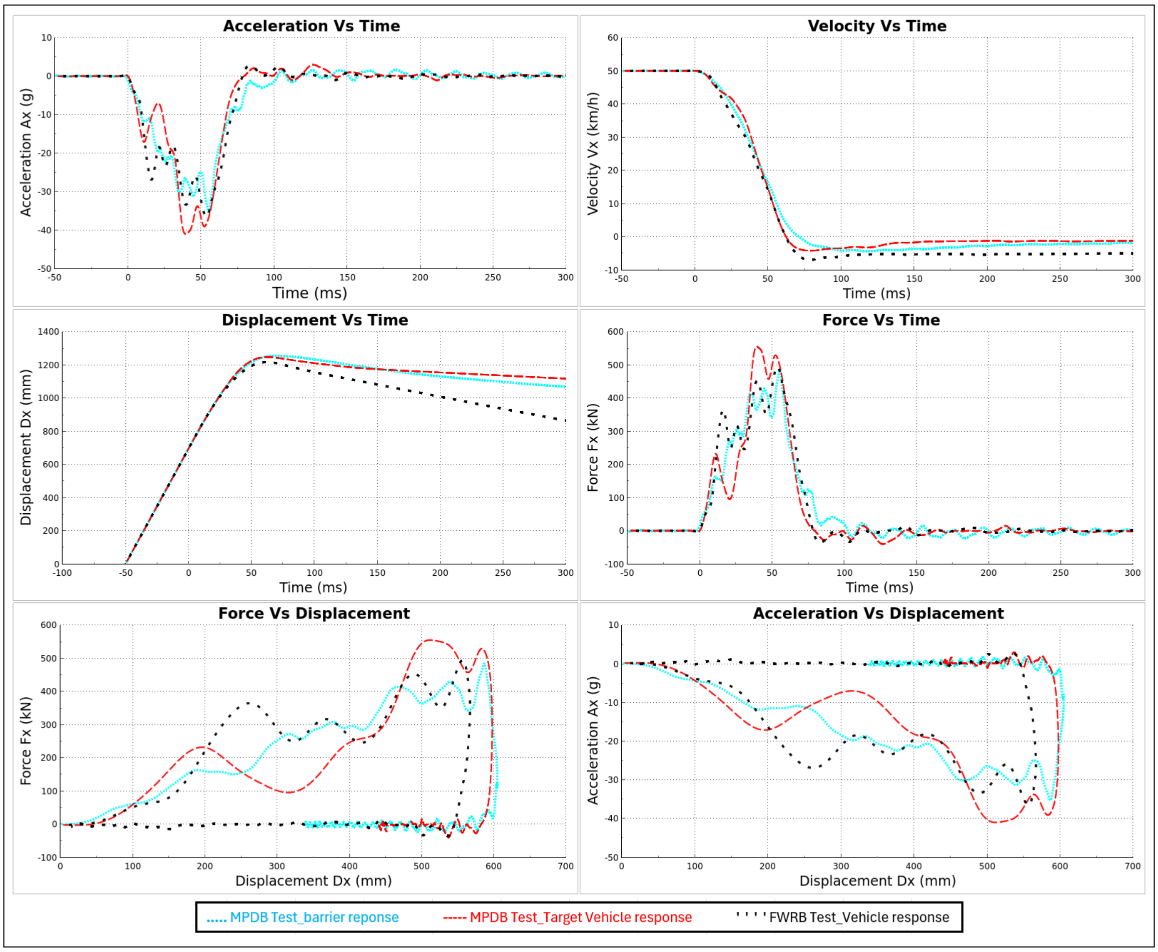

Figure 4.8: Representative vehicle crash response characteristics

Figures 4.9 and 4.10 present the force–displacement (F–D) response of representative ICEV and BEV cases respectively. The ICE vehicle shows a steeper initial rise in force with peak values occurring at lower displacement levels. In contrast, the BEV exhibits a more gradual increase in force, with peak values observed at higher displacement levels and extending over a wider deformation range. The BEV response also maintains relatively higher force levels over a longer displacement interval compared to the ICE case. In both cases, the MPDB barrier demonstrates a comparatively smoother and more consistent force–displacement response.

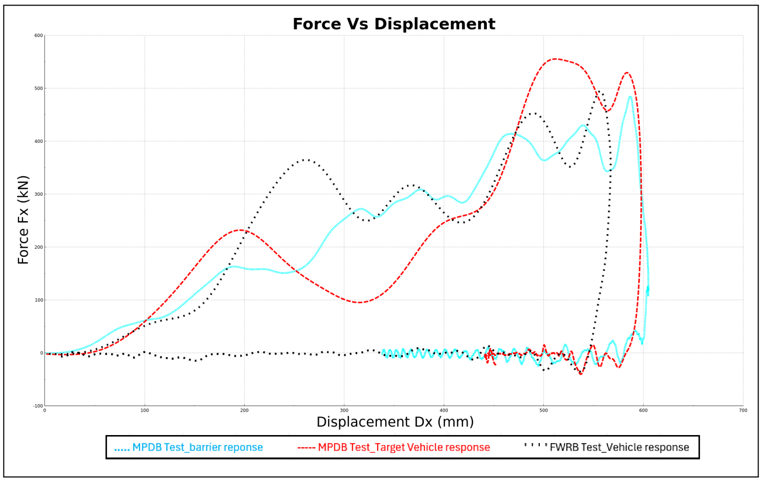

Figure 4.9: Vehicle force–displacement (F–D) response - ICEV

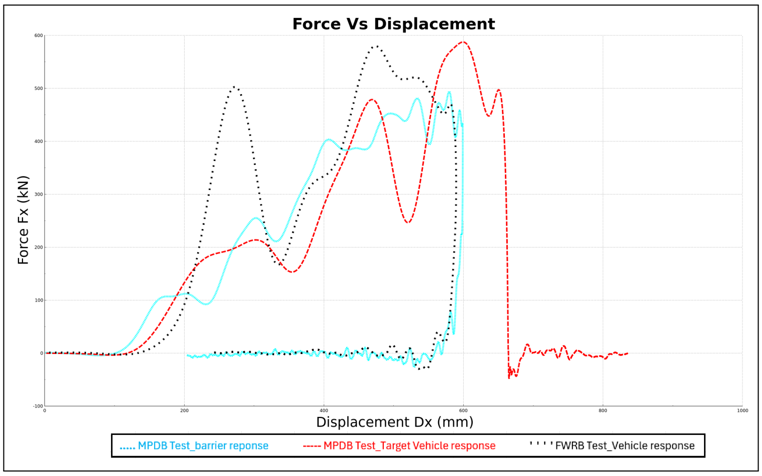

Figure 4.10: Vehicle force–displacement (F–D) response - BEV

Similar response plots were generated for a total of seven representative vehicles, showing consistent trends across all cases, with variations in force levels and displacement behaviour primarily influenced by vehicle mass. The corresponding F-D plots for the remaining vehicles are provided in Appendix A.5, from Figure A.23 to A.27.

To obtain a representative dataset, the responses were averaged for each test configuration. The corresponding averaged F-D plots are presented in Figures 4.11, 4.12, & 4.13 for the MPDB barrier, MPDB target vehicle, & FWRB vehicle, respectively. These averaged curves reduce vehicle-specific variations and highlight the overall response characteristics, with the MPDB barrier showing higher peak forces and a steeper initial response, while the FWRB case remains comparatively smoother.

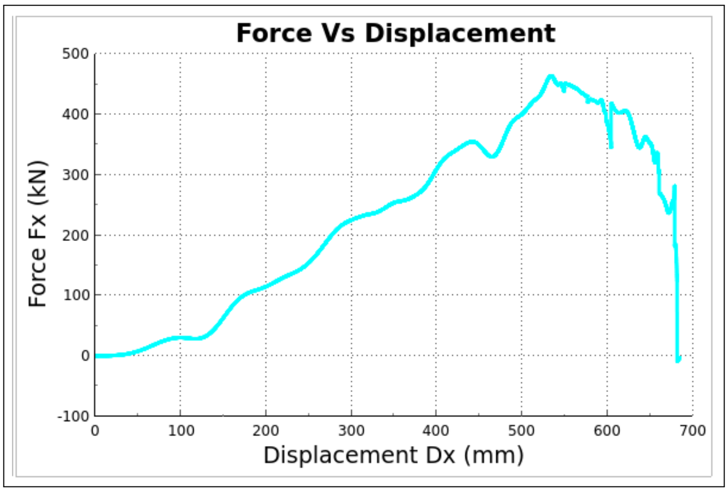

Figure 4.11: MPDB test - barrier force–displacement (F–D) response

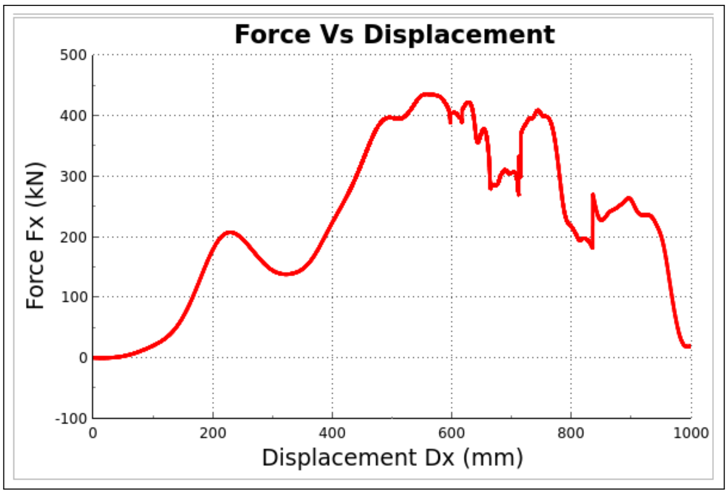

Figure 4.12: MPDB test - target vehicle force–displacement (F–D) response

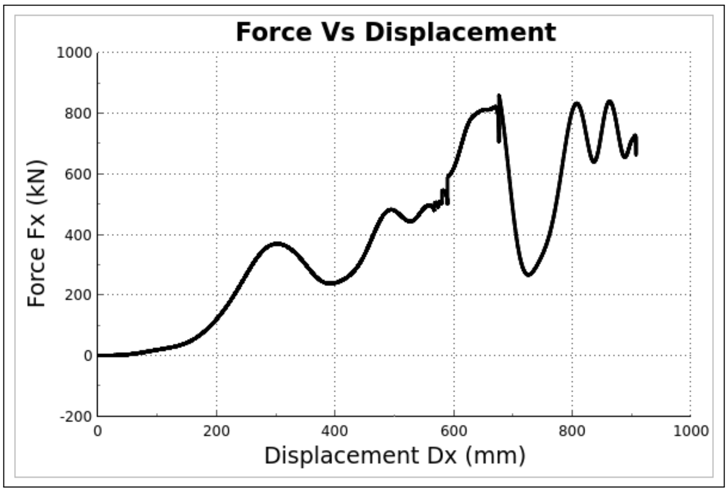

Figure 4.13: FWRB test - vehicle force–displacement (F–D) response

The averaged force–displacement (F–D) characteristics for the vehicle and barrier systems are overlapped in Figure 4.14. These curves represent the overall crash response behaviour derived from the crash pulse analysis. The MPDB barrier curve shows higher force levels at lower displacements, while the vehicle responses (MPDB target and FWRB) exhibit a more gradual increase in force with displacement.

The maximum force obtained from the MPDB target vehicle response is identified from these curves and used as a reference input for subsequent force distribution analysis. The F–D curves therefore provide a link between the time-based crash response and the force levels used for spatial force mapping across the barrier surface.

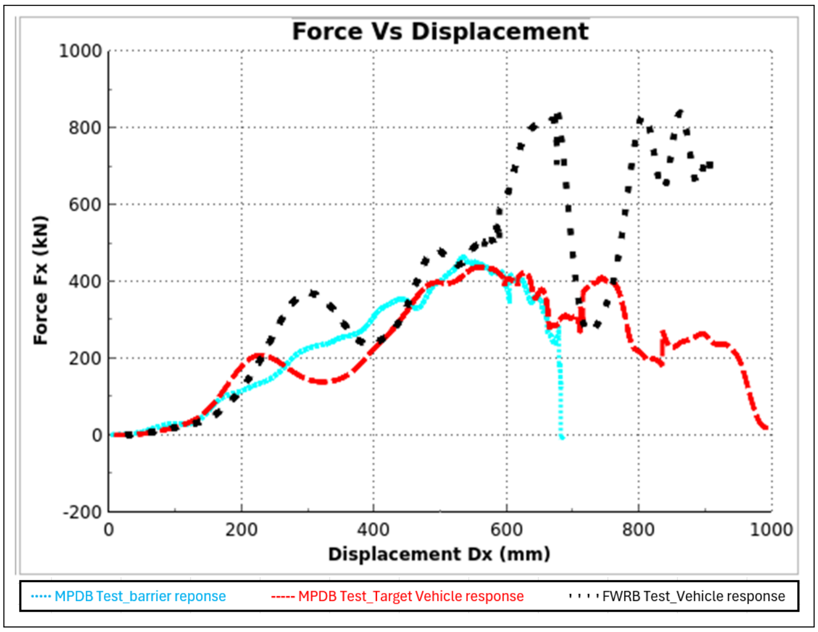

Figure 4.14: Vehicle crash response characteristics - All tests

4.4 Force Distribution and Structural Overlap

Figure 4.15 shows the theoretical force distribution across the barrier surface for a representative ICEV, where the load is distributed based on the crush strength variation along the static corridor of MPDB block B. A non-uniform pattern is observed, with higher forces concentrated in specific regions. A corresponding theoretical force distribution for the BEV case is shown in Figure 4.16. While both cases exhibit a similar overall spatial pattern, spread and intensity of forces differ across the grid.

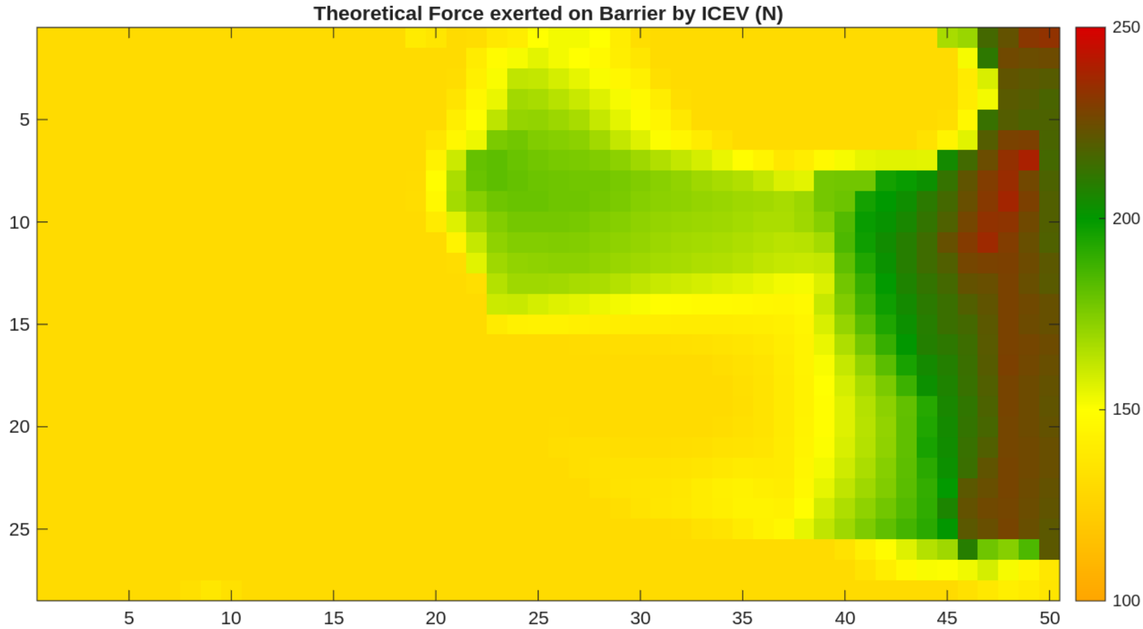

Figure 4.15: Theoretical force distribution heatmap - ICEV

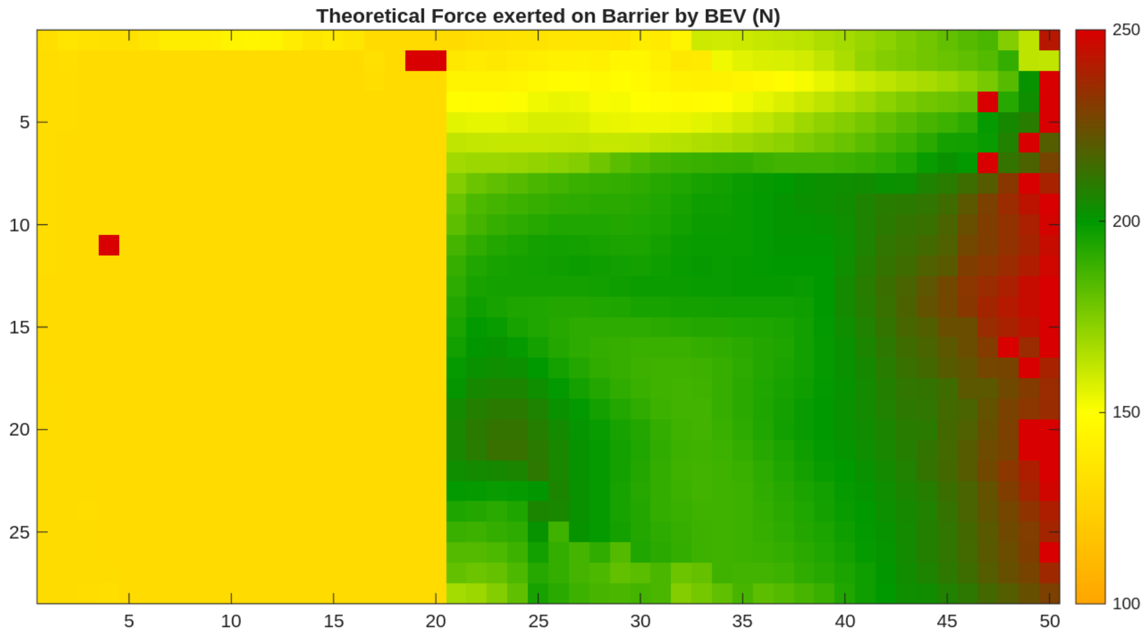

Figure 4.16: Theoretical force distribution heatmap - BEV

Figure 4.17 and 4.18 present the F–D responses of the MPDB target vehicle for ICEV and BEV, respectively, with the maximum force values identified for each case. These values are used to scale the corresponding theoretical force distributions.

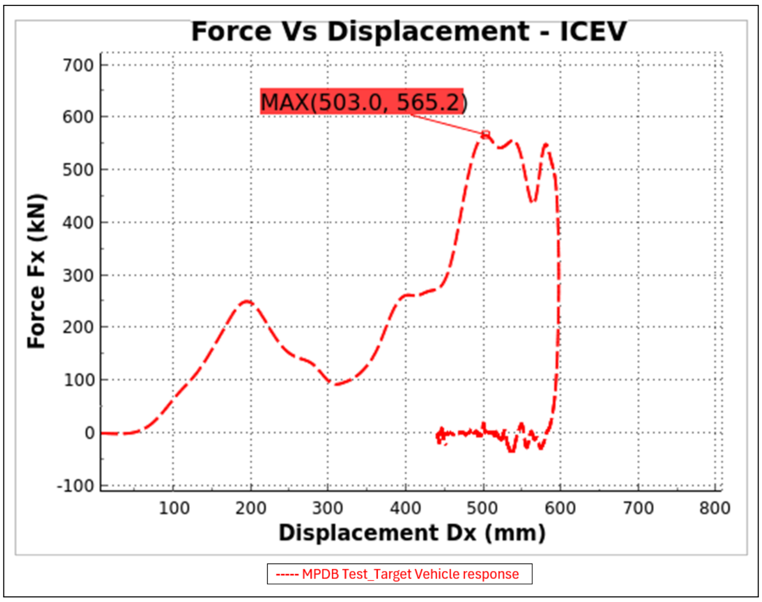

Figure 4.17: F-D response plot for MPDB Test target vehicle - ICEV

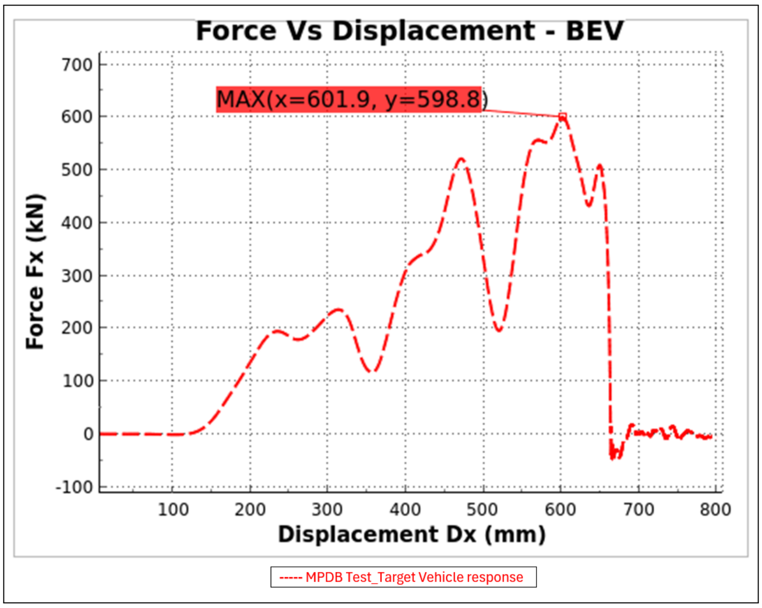

Figure 4.18: F-D response plot for MPDB Test target vehicle - BEV

Using these values, the localized force distributions (Figures 4.19 and 4.20) are derived. The spatial trend remains broadly consistent with the theoretical distributions; however, the force levels and their spread differ between ICEV and BEV, with BEV showing higher and more distributed force levels due to its increased mass.

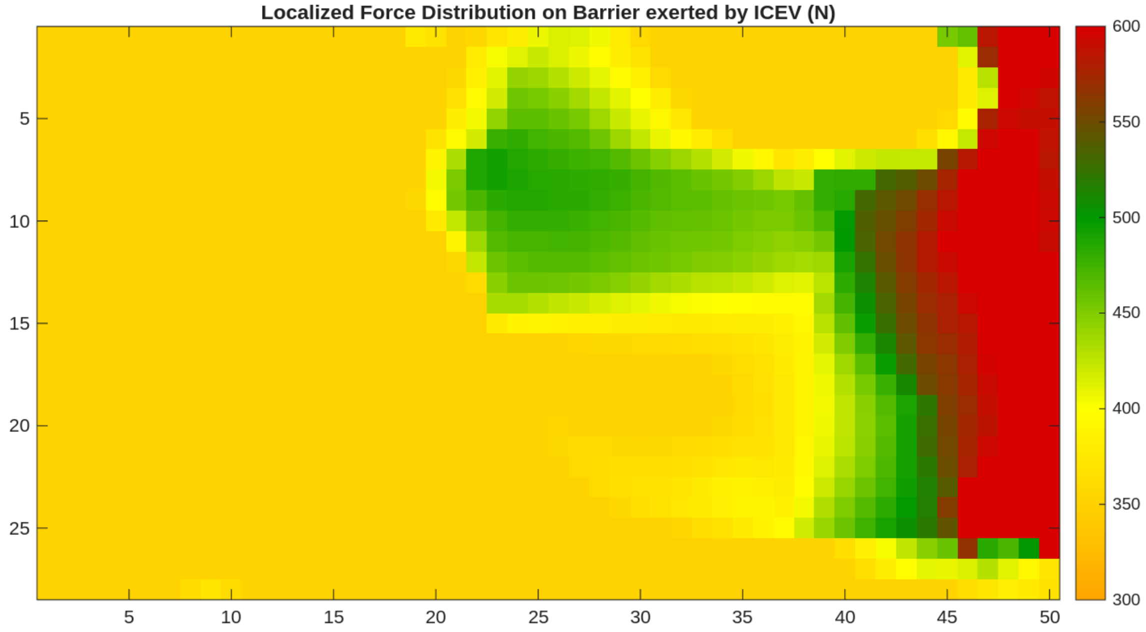

Figure 4.19: Actual localized force distribution heatmap - ICEV

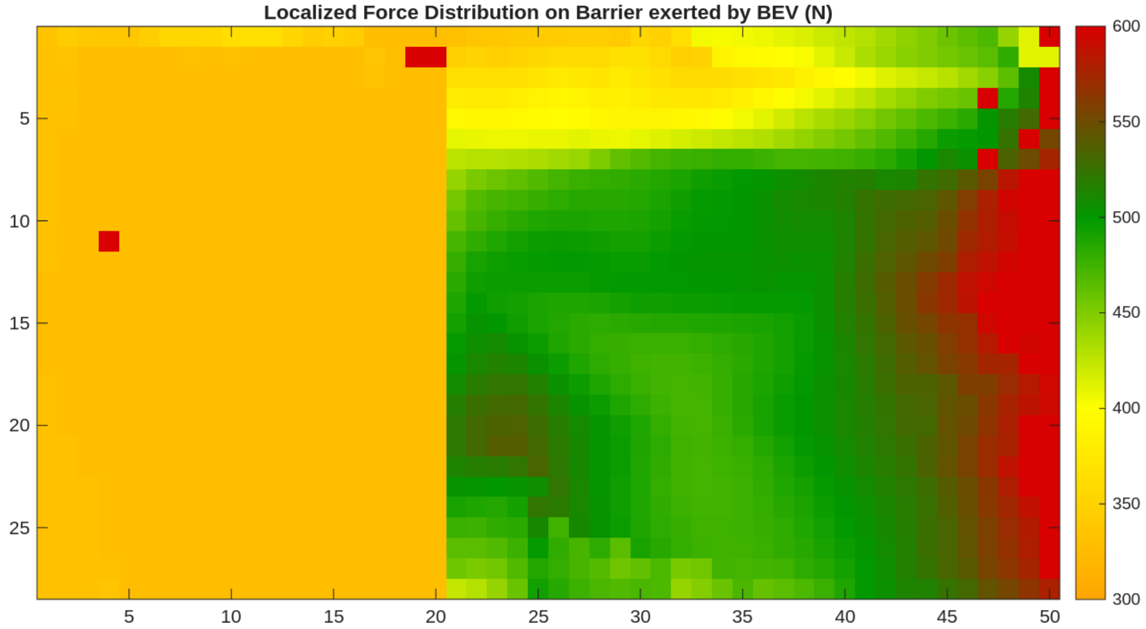

Figure 4.20: Actual localized force distribution heatmap - BEV

To enable easier comparison and interpretation, the results were also represented using a reduced (7×10) grid. The coarser heatmaps retained the overall deformation pattern while reducing the need to evaluate all 1400 grid points, thereby improving computational efficiency for larger datasets. Key regions of high and low interaction remained clearly identifiable even after grid reduction, indicating that the reduced grid captures the main spatial trends effectively.

A similar analysis was carried out for seven vehicles selected in total to capture representative behavior across the data set. The corresponding force distributions were first averaged to obtain a representative theoretical force heatmap (Figure 4.21), showing the spatial distribution of load across the barrier surface. Detailed force distribution heatmaps for all individual vehicles, including both derived and localised cases, are provided in Appendix A.6 (Figures A.28 to A.37) for reference.

The F–D responses of these vehicles were then averaged (Figure 4.22) to obtain a representative maximum force value. Using this reference, the averaged theoretical force distribution was scaled to derive the localized force distribution (Figure 4.23), capturing the spatial variation of load across the barrier.

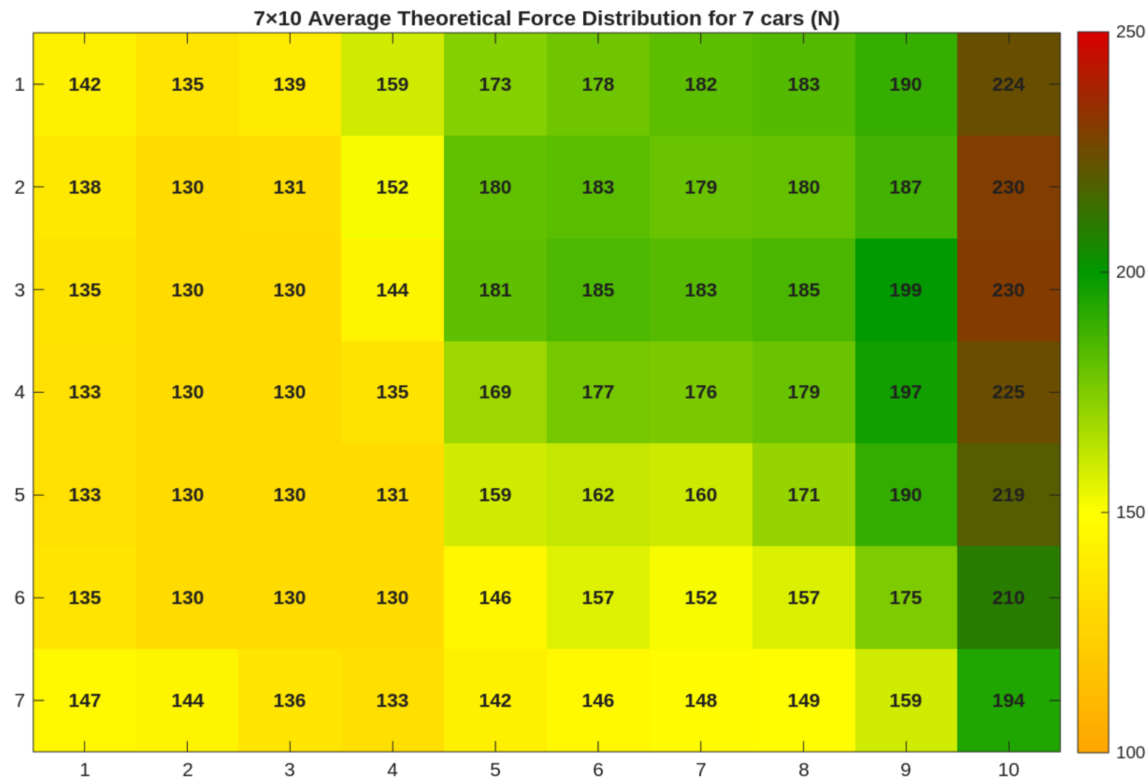

Figure 4.21: Averaged theoretical force distribution heatmap for 7 cars

The force–displacement (F–D) responses for the same set of vehicles were then averaged (Figure 4.22), and the corresponding maximum force value was identified. This value was used as the reference input for stiffness calculation.

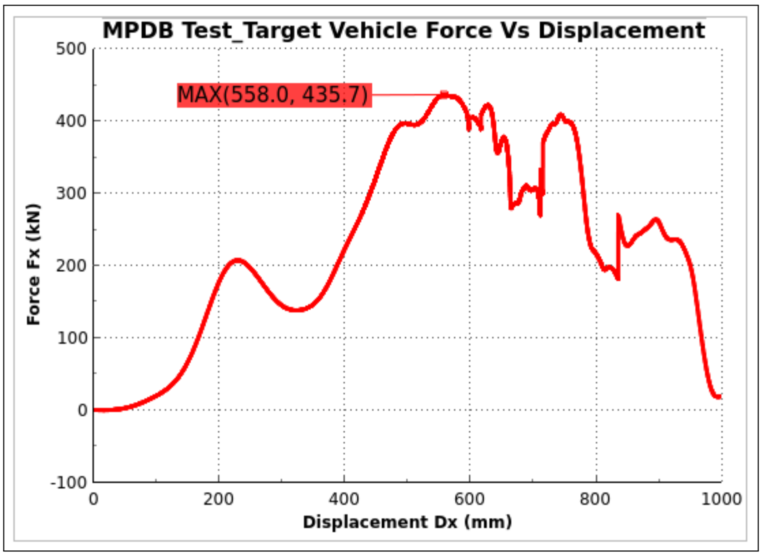

Figure 4.22: Averaged F-D characteristics plot for 7 cars

Based on this reference, the averaged force distribution was converted into a corresponding stiffness distribution, resulting in the representative stiffness heatmap (Figure 4.23), which captures the spatial variation of stiffness across the barrier.

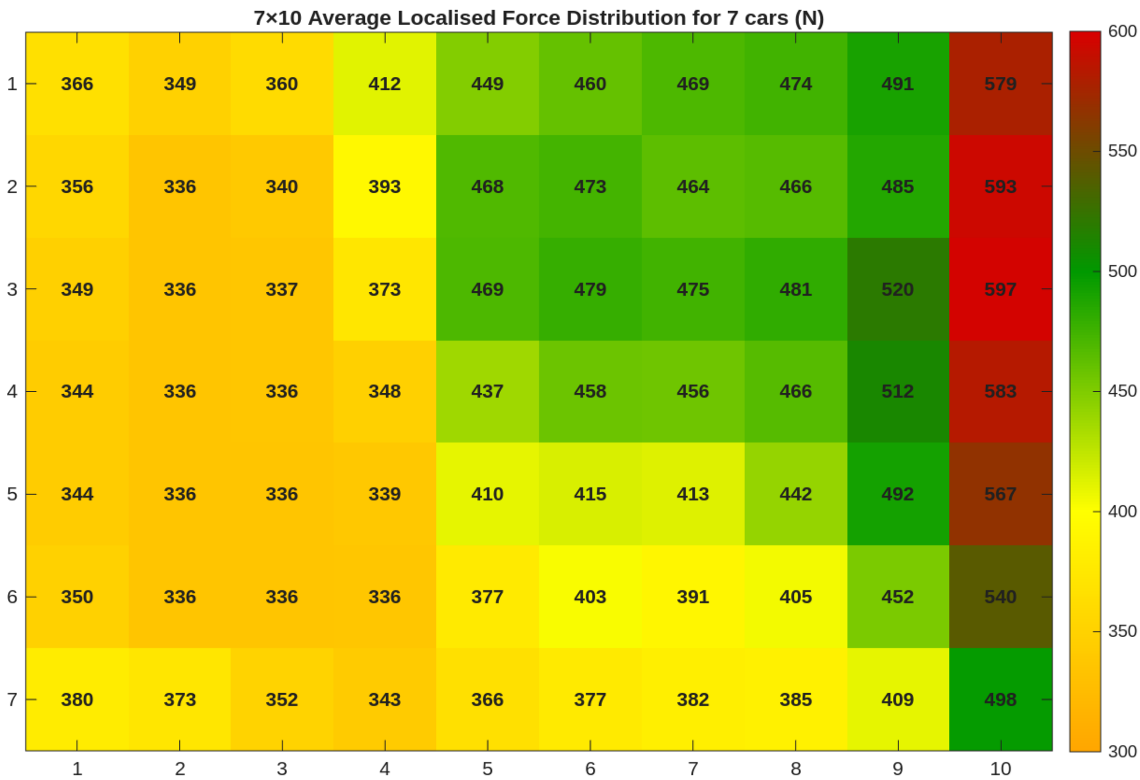

Figure 4.23: Averaged localized force distribution heatmap for 7 cars

Figure 4.24 shows the overlap of section height distributions with the force distribution on the barrier surface. The force distribution is compared with the adjusted section heights, considering an approximate 20 mm reduction in ride height due to the additional dummy mass (+160kg) based on literature study [19] [20] [21]. The region of higher force intensity is concentrated within a vertical band that aligns closely with the main rail, indicating that this component lies within the primary interaction zone during impact. In contrast, the upper rail lies above this region and the subframe extension lies partially below it, showing comparatively limited overlap with the dominant force region.

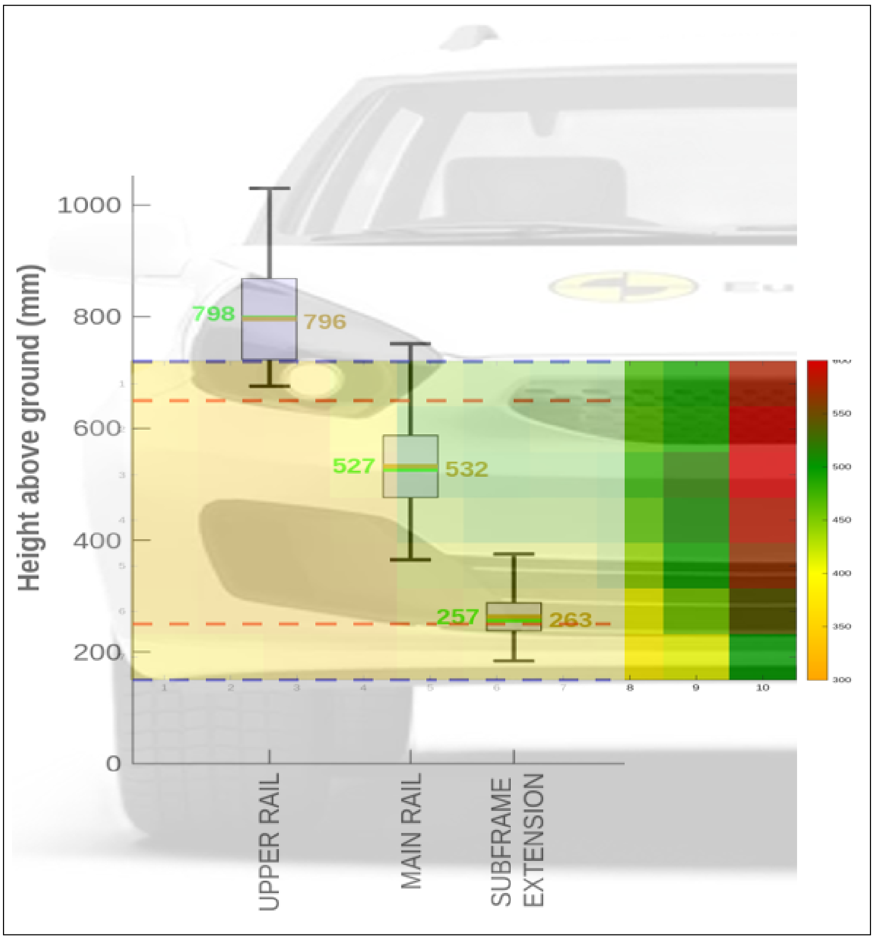

Figure 4.24: Localized force overlap with structural height positioning for 7 cars

Figure 4.25 further shows the overlap in the lateral direction, where the force distribution broadly follows the width positioning of the structural members. The alignment observed in both vertical and lateral directions highlights regions where the force concentration coincides with the position of key components. These overlapping regions form distinct hotspots, representing areas of strong structural interaction on the barrier surface.

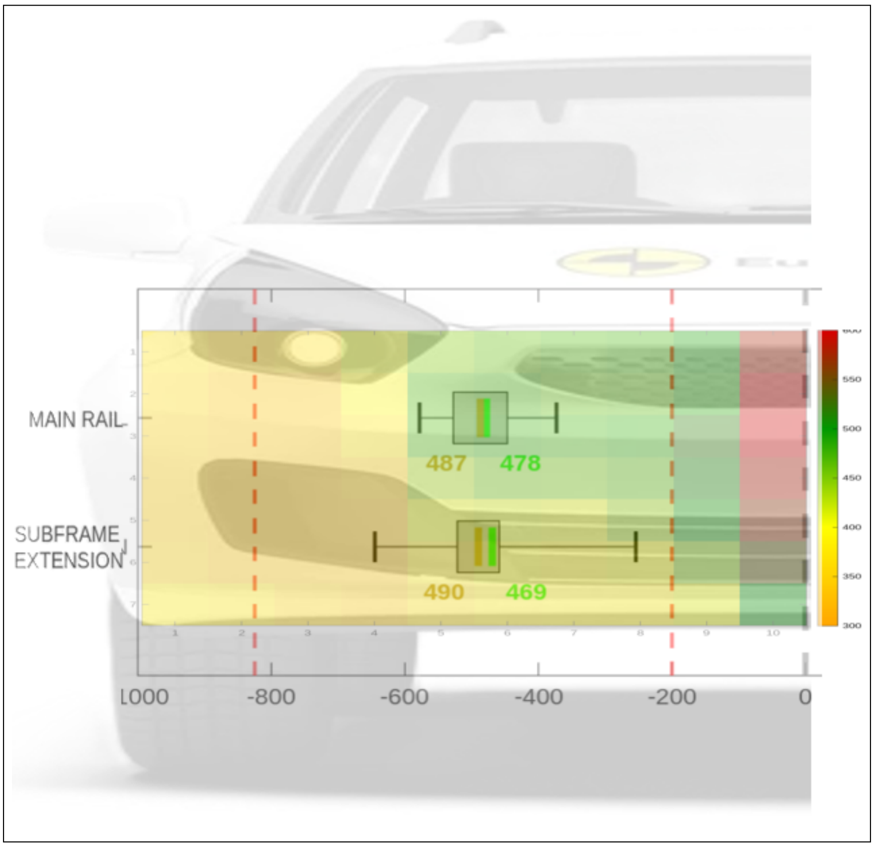

Figure 4.25: Localized force overlap with structural width positioning for 7 cars

In addition to these aligned regions, some higher force concentrations are observed outside the defined structural bounds. These are associated with contributions from engine compartments in ICE vehicles and motor/packaging regions in BEVs, which are not fully captured by the structural components. Overall, the combination of vertical and lateral overlap provides a clearer identification of hotspot zones, showing where force concentration occurs in line with component positioning as well as where additional contributions exist.

5 DISCUSSIONS

5.1 Kerb weight updates in cars

The kerb weight distribution results (Figure 4.1) and weighted values in Table 4.1, indicate that although the overall mean mass (1592 kg) is still close to the MPDB reference value of 1400 kg, this hides a significant shift in the vehicle fleet. The comparison with the VC-COMPAT dataset (1428 kg), which was based on an ICE-dominated fleet, shows an increase of nearly 200 kg in the weighted average mass. This increase is primarily due to the growing contribution of heavier HEVs and BEVs, while the share of ICEVs in the current dataset is reduced.

This trend highlights that the existing MPDB reference mass, based on a lighter ICE fleet, may no longer represent current vehicle characteristics. As electrification increases, the resulting higher vehicle mass is expected to influence real-world impact behaviour. Therefore, it becomes necessary to reconsider the use of a single reference mass in barrier design, or at least account for the evolving fleet composition, to ensure that the barrier concept remains representative of modern vehicle interactions.

5.2 Geometric positioning of car front structures

- **Section Height**

The distribution of section heights (Figure 4.2) shows that the structural layout is broadly grouped into lower, mid, and upper load paths with respect to the MPDB assessment limits. The mid-level components are positioned close to the MPDB interaction region, aligning key load-carrying members within this zone. The upper rail remains clearly above this region, while lower components lie closer to the lower boundary, maintaining a layered vertical arrangement.

This overall arrangement suggests a consistent structural strategy, where different load paths are positioned at distinct vertical levels. This distribution may influence the transfer of loads through the structure during frontal impact, with the mid-level components contributing near the interaction zone and the upper and lower paths supporting load sharing across the structure. Although a small reduction in ride height is expected due to the added occupant mass (20 mm), this effect is minimal compared to the observed upward shift in section heights (80–100 mm) in the A2MAC1 dataset.

The observed differences in weighted mean heights between A2MAC1 & VC-COMPAT indicate a consistent upward shift in the positioning of structural components in the A2MAC1 dataset (Figure 4.3). Placing the primary load path components, such as the main rails and bumper crossbeam, slightly higher improves their alignment with the MPDB loading zone, which can enhance load transfer during a frontal impact. Similarly, the higher position of the upper rail shows a stronger upper load path, helping to spread the impact energy more effectively. In contrast, the comparatively lower positioning of components in the VC-COMPAT dataset may result in reduced overlap with the MPDB interaction region. These differences reflect changes in structural design approaches over time, with newer vehicles showing trends in how frontal crash performance has evolved compared to the earlier VC-COMPAT dataset.

The differences in section heights across ICEV, HEV, and BEV mainly reflect changes in structural layout (Figure 4.4). In HEV and BEV cases, mid-level components such as the main rails and crash cans are positioned slightly higher, likely due to battery packaging at the floor level. In contrast, lower structural components like the subframe and its extensions remain largely consistent across all powertrains. The upper rail also remains the highest component, maintaining a clearly defined upper load path. Although these differences are small, they are important in the context of increasing electrification and evolving vehicle design.

- **Section Width**

The observed distribution of section widths (Figure 4.5) indicates that both main rails and subframe extensions are consistently positioned within the MPDB interaction zone, defined by approximately 45% of the vehicle width. This suggests that the lateral placement of these components aligns well with the expected load contact region during a frontal impact. Since the MPDB assessment area is based on about 45% of the vehicle width, placing these components within this range helps ensure good contact and load transfer. The symmetry about the centerline also shows a balanced layout, and the small variation in widths suggests a consistent approach in how these main structural members are positioned.

The similarity in main rail widths across ICEV, HEV, and BEV shows that the primary load-carrying components are positioned in a consistent way across different powertrain types. (Figure 4.6). In contrast, the variation observed in subframe extension widths, particularly the higher values in HEV, indicates differences in structural packaging that may be influenced by component layout. Since the MPDB assessment area depends on the vehicle width, keeping the rails within this region helps ensure proper contact during a frontal impact.The symmetry about the centerline also shows a balanced layout, while the small variations in width suggest that the placement of these components is fairly consistent across different vehicles.

- **Section Length**

The variation in section lengths (Figure 4.7) reflects how different components extend forward from the front tyre (axle) centreline. Components such as the main rail, lower crossbeam, and subframe extend further forward, showing their role in carrying loads deeper into the structure. In contrast, the crash can and bumper crossbeam are mainly located in the front impact region and act as initial load transfer elements. The upper rail lies closer to the axle, while the subframe extension falls in between. Some components extend up to the firewall, helping transfer loads further into the vehicle, while others remain more localised near the front. This arrangement reflects how load transfer is managed along the vehicle length during a frontal impact.

5.3 Crash pulse response

The crash pulse results show clear differences between the MPDB barrier and vehicle responses, partly linked to mass. The barrier shows a sharp deceleration peak and higher early force, indicating a stiffer response, while vehicle responses are smoother with a gradual force build-up. Heavier vehicles show a more sustained response, whereas lighter vehicles decelerate more quickly. This is also seen when comparing ICE and BEV, where the heavier BEV shows a delayed response with peak values occurring later.

The overall trends remain similar for all five vehicles, even though there are small differences between lighter and heavier cars. The averaged plots make this easier to see by removing individual variations. Even after averaging, the same behaviour is seen: the MPDB barrier response is steeper, while the FWRB case is more gradual and spread over a larger deformation.

The force–displacement curves reflect the same behaviour, with the barrier reaching higher forces at lower displacements and the vehicles showing a gradual increase. Heavier vehicles also maintain higher force levels over larger displacements. These results are useful for the next step, where this behaviour is used to define stiffness in the barrier model.

5.4 Force Distribution and Structural Overlap

The variation in force across the barrier surface shows that the interaction between the vehicle and the barrier is not uniform. While some higher force regions align with major structural load paths, particularly at mid-level components, other regions show limited correspondence. These additional force concentrations can be attributed to contributions from non-structural elements such as the engine block in ICE vehicles and motor, battery packaging, and radiator systems, which also participate in load transfer during impact but are not explicitly represented by the defined structural components.

Across ICEV, BEV, and averaged results, a similar overall trend is seen, with most of the force concentrated around the mid-height region. However, the way force spreads is different, with BEV showing a more distributed pattern compared to the more concentrated regions in ICEV. This difference is mainly due to variations in vehicle mass and layout.

When both height and width are considered together, the overlap between structural positioning and force distribution highlights clear hotspot regions. These are the areas where load transfer is most significant. Also, some high-force regions extend beyond these overlap zones, indicating additional contributions not captured by the defined structural components. These hotspots, along with the additional regions, help in identifying key interaction zones for further barrier design and segmentation.

6 CONCLUSIONS

Understanding the relationship between structural geometry and crash performance is essential for improving vehicle compatibility. This study demonstrates that variations in component positioning, crash pulse response, force distribution, and stiffness characteristics across vehicle segments form a strong foundation for developing representative barrier models. Moreover, the analysis of evolving design trends over past decades highlights the need for continuous updates in barrier concepts to accurately reflect modern vehicle front-end behaviour in frontal impacts.

The key findings drawn from the analysis supporting the development of a CAE barrier model, are summarised below:

- The kerb weight results show that even though the overall average is still close to the current MPDB value, the growing share of heavier HEVs and BEVs points to a clear shift in vehicle mass. This trend highlights the need to reconsider and update the reference kerb weight used in MPDB barrier development to ensure it remains representative of future fleet conditions.

- The structural layout groups components into lower, mid, and upper load paths, with mid-level members aligned with the MPDB interaction zone. This pattern is consistent across ICEV, HEV, and BEV, with only minor variations due to electrification, reflecting a well-defined load transfer strategy for frontal crash performance.

- Modern vehicles show a clear upward shift in structural component heights, reflecting evolving design trends such as increased ground clearance. This suggests a need to revisit MPDB barrier assessment heights to maintain proper alignment with current front-end structures.

- Component placement from the front tyre centreline shows differences in forward reach, with the main rail, lower crossbeam, and subframe extending further forward, while the bumper crossbeam and crash can are positioned closer to the impact region, supporting progressive load transfer.

- The derived crash response and force–displacement (F–D) characteristics show consistent behaviour across vehicles, with clear differences between barrier and vehicle responses. These results provide a reliable basis for representing load transfer in barrier modelling.

- The force distributions show non-uniform interaction across the barrier surface, with specific regions carrying higher loads. The reduced grid approach captures these patterns effectively while remaining suitable for larger datasets.

- Combining force distributions with load path positioning shows clear overlap in some regions, helping identify key load transfer areas and support barrier segmentation. At the same time, the high-force regions are not fully covered by the structural components, suggesting contributions from engine or motor/packaging that are not included in the dataset.

7 FUTURE WORK

Current crash assessment approaches provide a useful basis for evaluating vehicle interaction, but they are largely based on designs representing older vehicle fleets. Over time, front-end structures have evolved due to trends such as increased ground clearance and the growing influence of electrification. As a result, there is a need to revisit barrier concepts so that they better reflect the interaction behaviour of modern and emerging vehicles. This forms the main motivation for the present work.

Within this context, the current study is limited by the size and coverage of the structural dataset used. While the available data was sufficient to identify general trends in load path positioning and force distribution, it does not fully capture the variability across different vehicle categories and newer designs. In addition, certain high-force regions observed in the analysis are not fully aligned with the defined structural components, indicating contributions from engine compartments in ICE vehicles and motor/packaging regions in BEVs, which are not explicitly represented in the current structural definition. This is mainly due to the limited scope of the project and time constraints associated with data collection and processing.

Similar limitations apply to the crash pulse and deformation grid data used to derive representative force–displacement (F–D) behaviour, peak force levels, and localised force distributions across the barrier surface. Although the available test data helped in identifying key interaction patterns, it does not fully represent real-world variability. Access to larger and more consistent datasets would significantly improve the reliability of the derived inputs. In this context, advanced data processing techniques such as Principal Component Analysis (PCA) can be explored to efficiently handle large deformation datasets while capturing dominant structural behaviour patterns [22].

Moving forward, an important step would be to develop a more comprehensive input database by combining structural positioning, crash pulse response, and deformation-based force distribution across a wider range of vehicles. This would allow more consistent derivation of F–D behaviour and local interaction characteristics, forming a stronger basis for further model development. Also, incorporating the additional contributions from engine and motor/packaging regions into the structural representation would further improve the accuracy of captured interaction behaviour.

Based on these improved inputs, barrier segmentation can be further refined using identified high-force regions and their alignment with structural components [18]. The current segmentation approach provides a useful starting point; however, additional iterations are required to better define segment boundaries and capture variations in structural interaction.

Finally, these refined inputs can be implemented in a CAE-based barrier model, followed by simulation and iterative tuning. This would enable validation of both global crash response and local deformation behaviour, ensuring that the barrier concept more accurately represents modern vehicle structures and evolving design trends [23].

References

[1] Krusper, A. (2014): Structural Interaction between Vehicles: An Investigation of Crash Compatibility between Cars and Heavy Goods Vehicles, Chalmers University of Technology.

[2] Euro NCAP (2023); Mobile Progressive Deformable Barrier (MPDB) Frontal Impact Testing Protocol, Version 2.0.

[3] VC-COMPAT Consortium (2012): Compatibility of Passenger Cars and Light Commercial Vehicles, Final Report, European Commission Seventh Framework Programme (FP7).

[4] UNECE Regulation No. 93 (2002): Uniform Provisions Concerning the Approval of Front Underrun Protective Devices (FUPDs), United Nations Economic Commission for Europe.

[5] Thomson, R., et al. (2007): Car-Car Crash Compatibility: Development of Crash Test Procedures in the VC-COMPAT Project, International Journal of Crashworthiness.

[6] Buzeman, D., Viano, D.(2018): Crash Compatibility, Springer.

[7] Thomson, R., et al. (2021): Frontal Crash Incompatibility of Heavy Goods Vehicle in Crash Test with Passenger Car, ESV Conference, Paper No. 23-0321.

[8] Digges, K., Dalmotas, D., and Prasad, P. (2023): "An NCAP Rating for Females," Proceedings of the 27th International Technical Conference on the Enhanced Safety of Vehicles (ESV), Paper No. 23-0323.

[9] Thomson, R., et al. (2023): Frontal Crash Incompatibility of Heavy Goods Vehicle in Crash Test with Passenger Car, Proceedings of the 27th International Technical Conference on the Enhanced Safety of Vehicles (ESV).

[10] Euro NCAP (2023): Adult Occupant Protection Assessment Protocol, Version 9.1.3.

[11] FIMCAR Consortium (2012): Frontal Impact and Compatibility Assessment Research (FIMCAR), Final Report Summary, European Commission FP7.

[12] Krusper, A., Thomson, R. (2008): Structural Interaction between Vehicles – Compatibility between Passenger Cars and Heavy Goods Vehicles, Chalmers University of Technology.

[13] Sandner, V., Ratzek, H. (2015): Development of the Mobile Progressive Deformable Barrier (MPDB) for Frontal Impact Compatibility Assessment, Proceedings of the Enhanced Safety of Vehicles (ESV) Conference.

[14] Park, J., Hor, H. (2021): CAE-Based MPDB Compatibility Assessment Using Virtual Barrier Deformation Tracking, International Journal of Automotive Technology.

[15] I-CAR NZ (2019): Understanding Collision Energy Management (CEM).

[16] UNECE, Regulation No. 94 (1995): Uniform Provisions Concerning the Approval of Vehicles with Regard to the Protection of the Occupants in the Event of a Frontal Collision, United Nations Economic Commission for Europe (UN/ECE).

[17] SAE International (2014): Surface Vehicle Recommended Practice J211/1, Instrumentation for Impact Test – Part 1: Electronic Instrumentation, SAE Standard, Revised.

[18] Jiajie Yin, Zhi Fu, Jinzhou Ding, Linhui Liu, Tiqiang Fan, Yu Liu, Tao Li, Xingtao Liao, Yong Peng, Fang Wang (2025): Study on vehicle collision results under the AC-MPDB scheme, Transportation Safety and Environment, Volume 7, Issue 3.

[19] Vdovin, A., Sebben, S., Walker, T. et al (2014): Investigation of vehicle ride height and wheel position influence on the aerodynamic forces of ground vehicles. International Vehicle Aerodynamics Conference: 81-90.

[20] Trombella, M.(2021): Development of a Methodology for Crash Compatibility Assessment Using CAE Models, Master's Thesis, Politecnico di Milano.

[21] Synák, F., Nedeliaková, E. (2024): Changing the Position of the Vehicle's Center of Gravity as a Result of Different Load Distribution. Applied Sciences, 14(20), 9328.

[22] Jolliffe, I. T.(2002): Principal Component Analysis, Springer.

[23] Ellway, J., van Ratingen, M., et al.(2023): Euro NCAP Mobile Progressive Deformable Barrier (MPDB) Testing, Proceedings of the 27th ESV Conference.

[24] Euro NCAP European Cars Sales 2025.
Available: `https://www.euroncap.com/`

[25] A2MAC1 Platform 3D Explorer Database.
Available: `https://ibp.a2mac1.com/visual`

[26] Volvo XC60 Media Guide 2018.
Available: `https://downloads.regulations.gov/NHTSA-2023-0022-0080/attachment_2.pdf`

A Appendix

Column Abbreviation	Nomenclature in Excel Database
R	Length of vehicle
S	Width of vehicle
T	Height of vehicle
U	Wheelbase of vehicle
AA	Ground Clearance of vehicle
AB	Distance of front wheel axis center from ground
AC	Firewall distance from the front wheel axis center
AD	Subframe Extension bottom face height from ground
AE	Subframe Extension top face height from ground
AG	Subframe Extension start distance from the wheel center axis
AH	Subframe Extension end distance from the wheel center axis
AJ	Lateral distance from vehicle centerline to inner face of Subframe Extension
AK	Lateral distance from vehicle centerline to outer face of Subframe Extension
AN	Main Rail bottom face height from ground
AO	Main Rail top face height from ground
AQ	Main Rail start distance from the wheel center axis
AS	Lateral distance from vehicle centerline to inner face of Main Rail
AT	Lateral distance from vehicle centerline to outer face of Main Rail
AW	Lower Crossbeam bottom face height from ground
AX	Lower Crossbeam top face height from ground
AZ	Lower Crossbeam start distance from the wheel center axis
BA	Lower Crossbeam end distance from the wheel center axis
BC	Bumper Crossbeam bottom face height from ground
BD	Bumper Crossbeam top face height from ground
BF	Bumper Crossbeam start distance from the wheel center axis
BG	Bumper Crossbeam end distance from the wheel center axis
BI	Crash Can bottom face height from ground
BJ	Crash Can top face height from ground
BL	Crash Can start distance from the wheel center axis
BM	Crash Can end distance from the wheel center axis
BO	Subframe bottom face height from ground
BP	Subframe top face height from ground
BR	Subframe start distance from the wheel center axis
BS	Subframe end distance from the wheel center axis
BU	Upper Rail bottom face height from ground
BV	Upper Rail top face height from ground
BX	Upper Rail start distance from the wheel center axis
BY	Upper Rail end distance from the wheel center axis

Table A.1: Nomenclature used for geometric measurements of car

A.1 Car Nomenclature

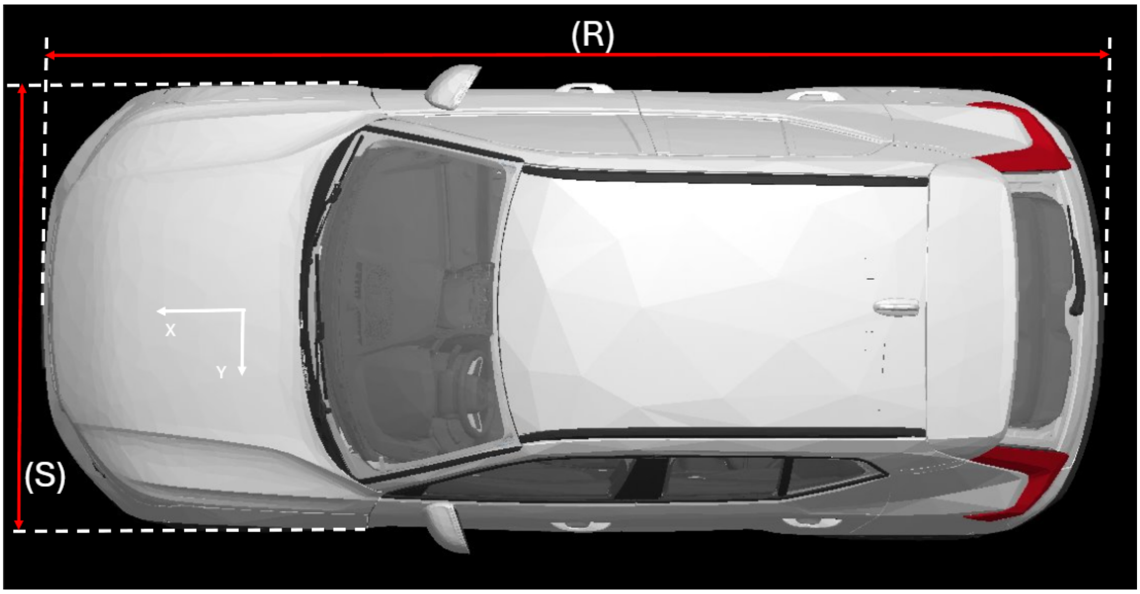

Figure A.1: Car overall dimensions - Top view [25]

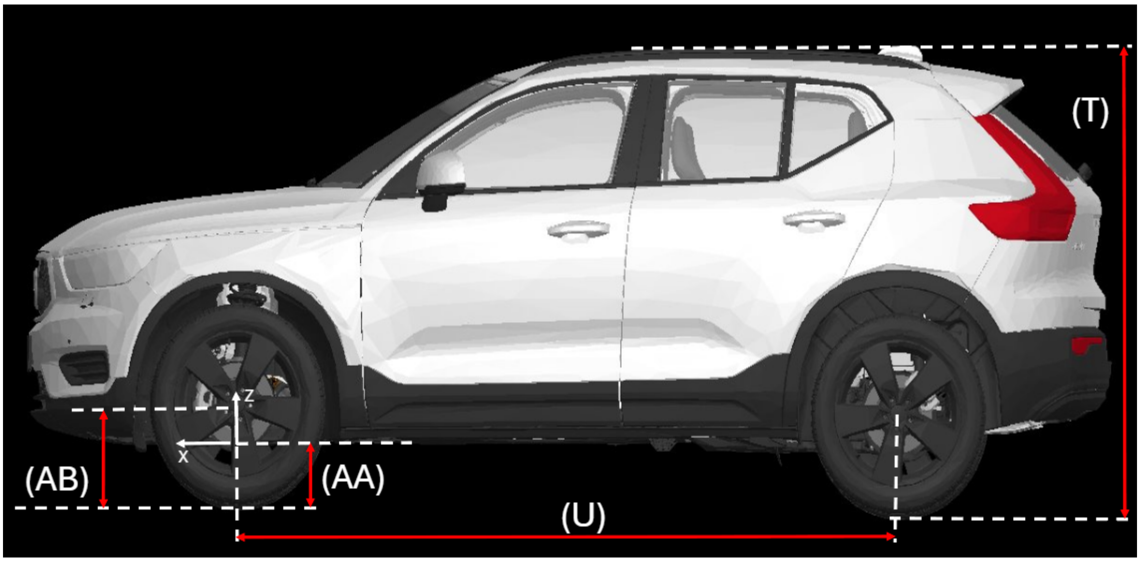

Figure A.2: Car overall dimensions - Side view [25]

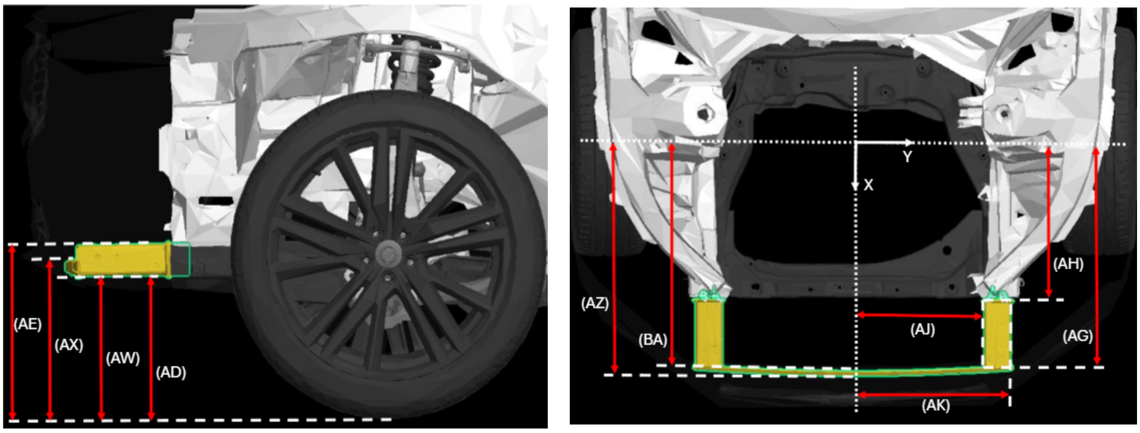

Figure A.3: Measurements for Subframe Extension & Lower Crossbeam - Side & Top views [25]

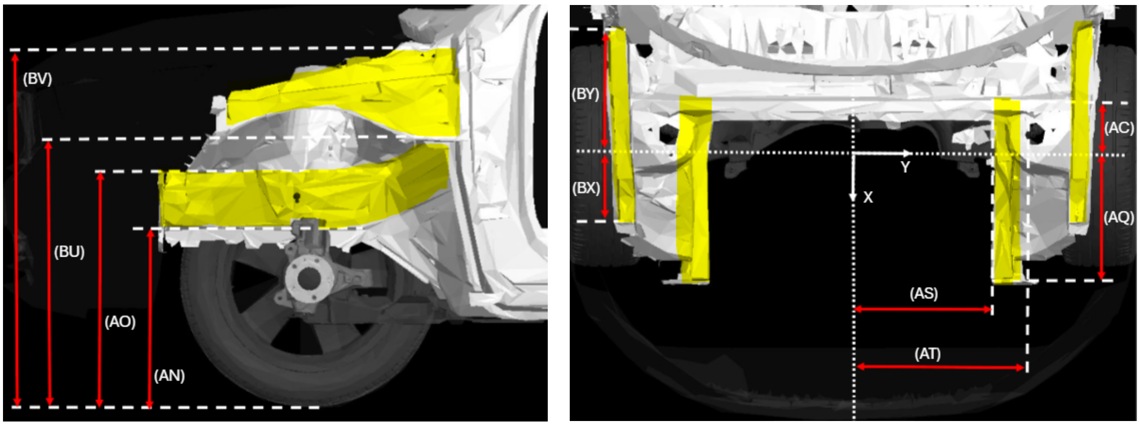

Figure A.4: Measurements for Main Rail & Upper Rail - Side & Top views [25]

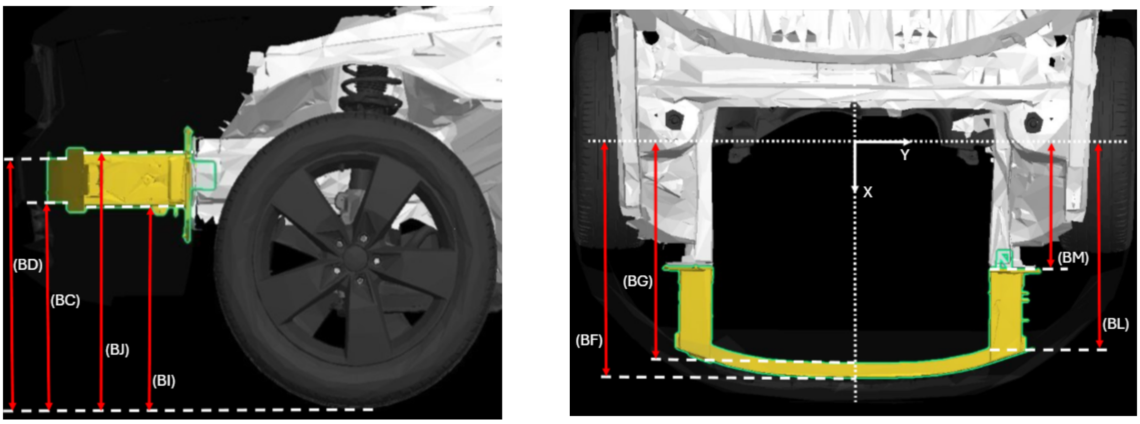

Figure A.5: Measurements for Crash Can & Bumper Crossbeam - Side & Top views [25]

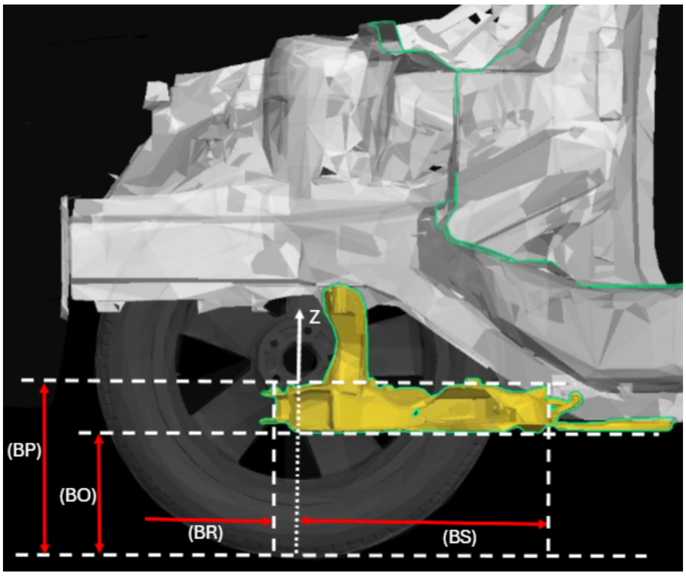

Figure A.6: Measurements for Subframe - Side view [25]

A.2 Section heights of car components

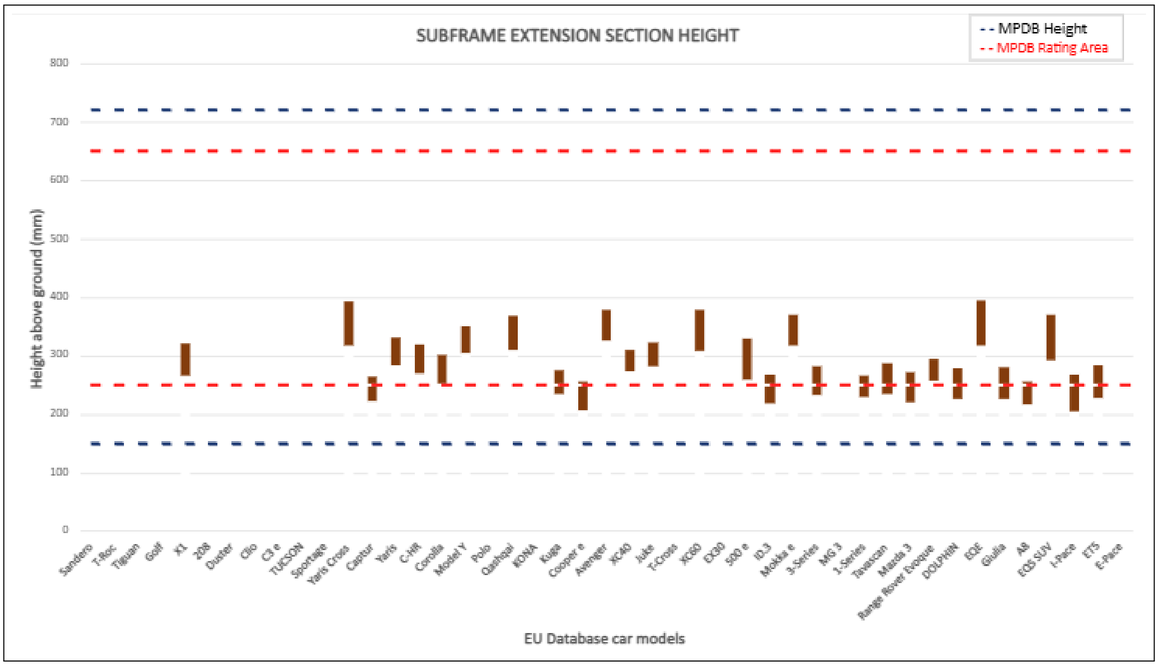

Figure A.7: Subframe Extension - Section Heights

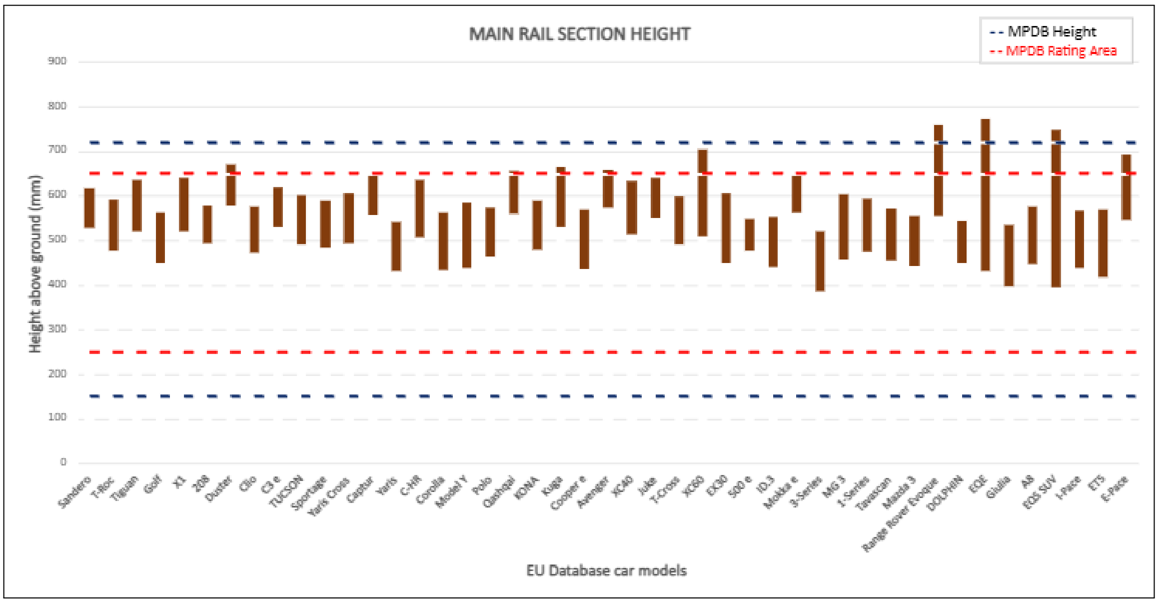

Figure A.8: Main Rail - Section Heights

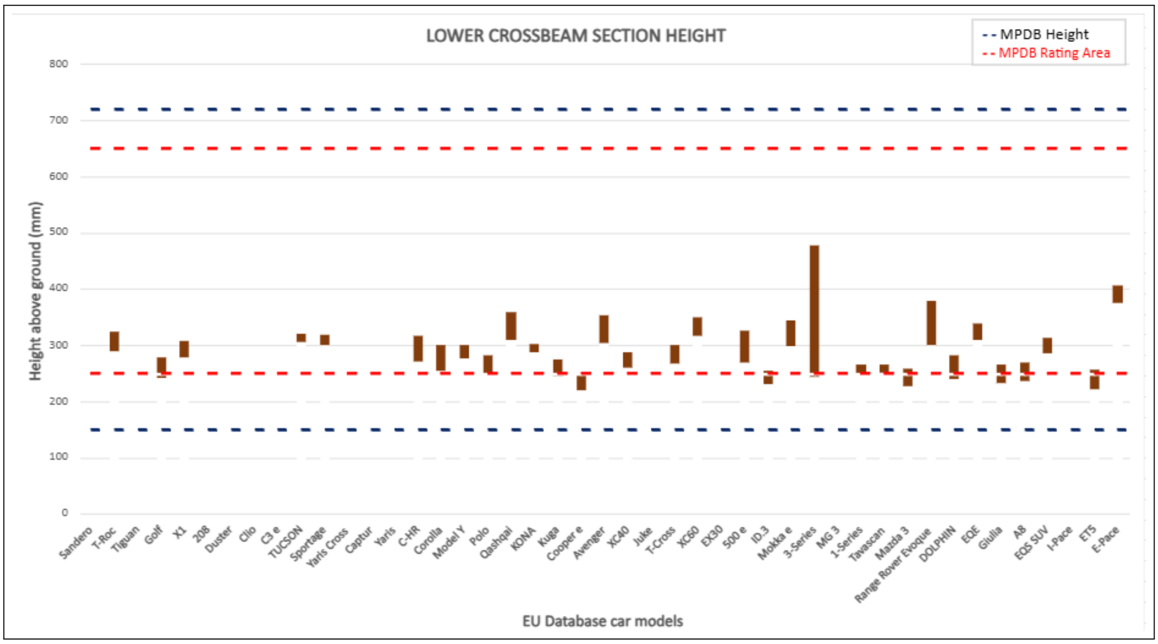

Figure A.9: Lower Crossbeam - Section Heights

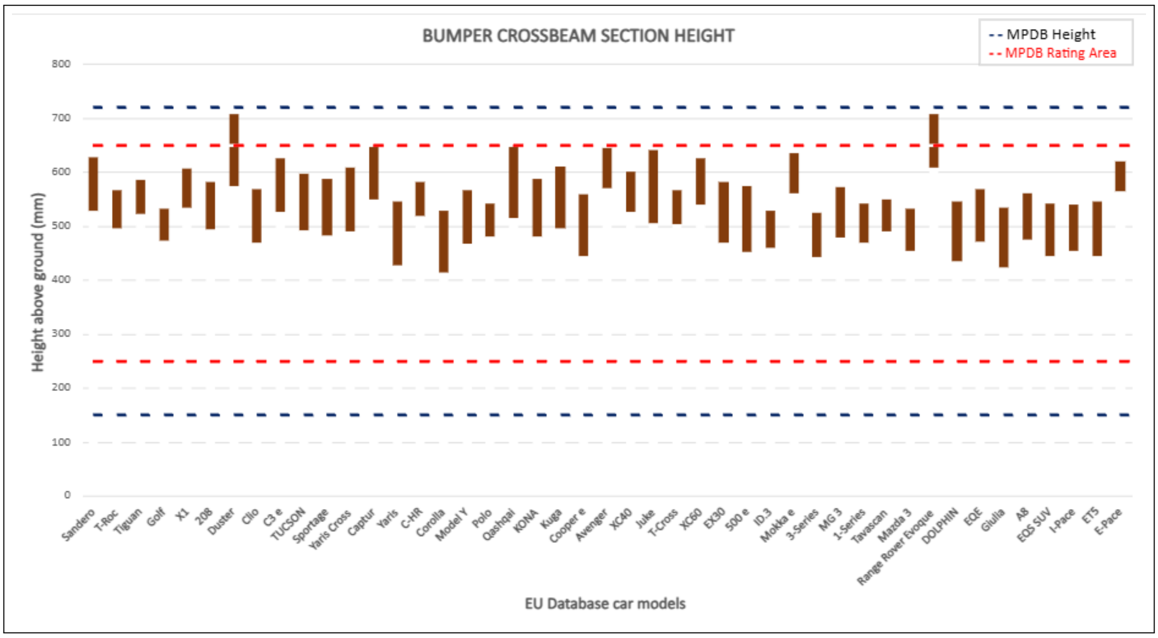

Figure A.10: Bumper Crossbeam - Section Heights

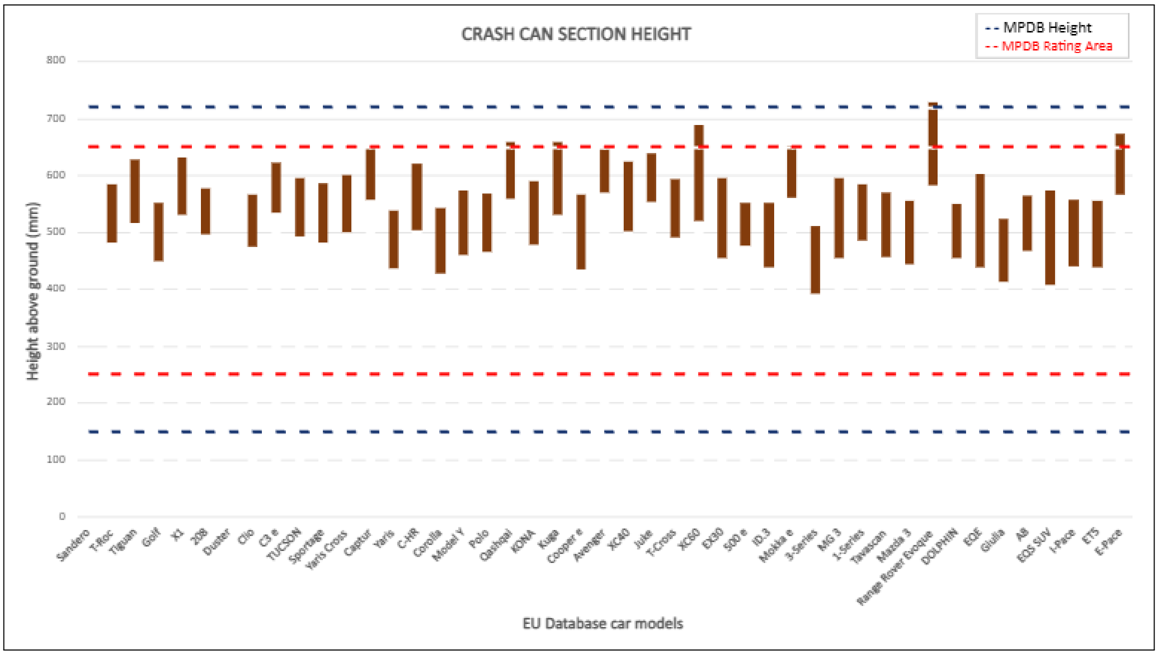

Figure A.11: Crash Can - Section Heights

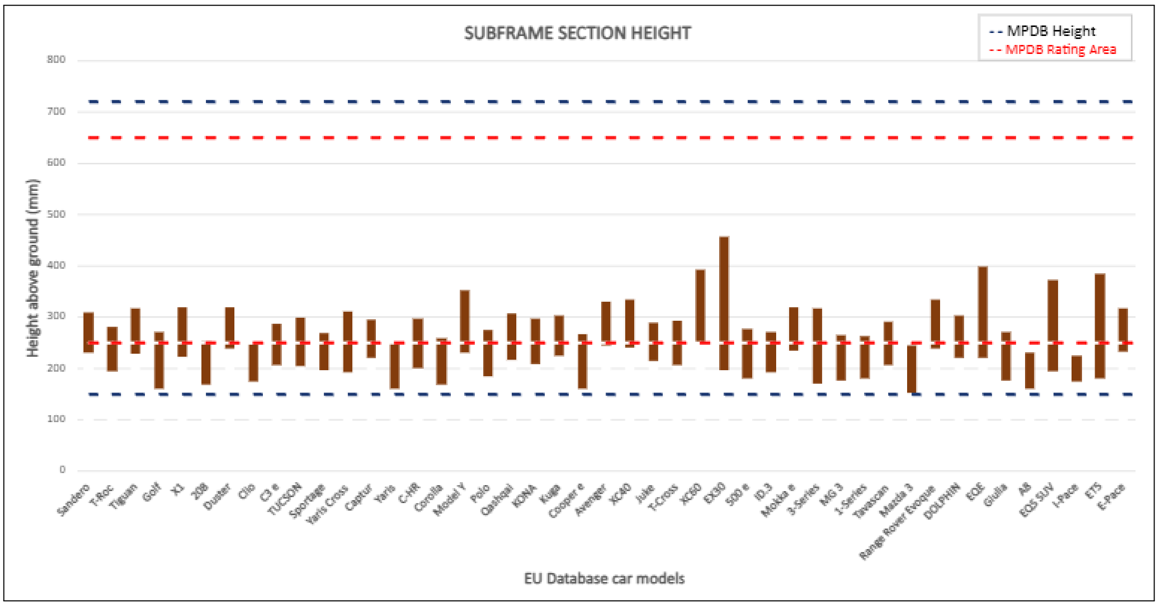

Figure A.12: Subframe - Section Heights

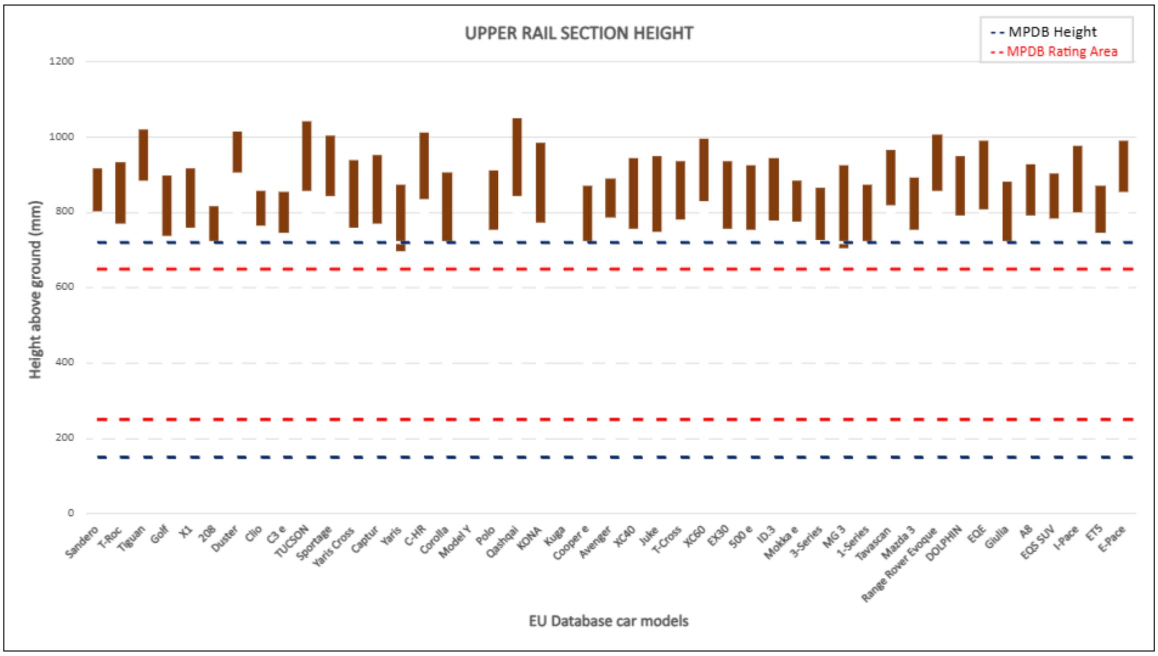

Figure A.13: Upper Rail - Section Heights

A.3 Section widths of car components

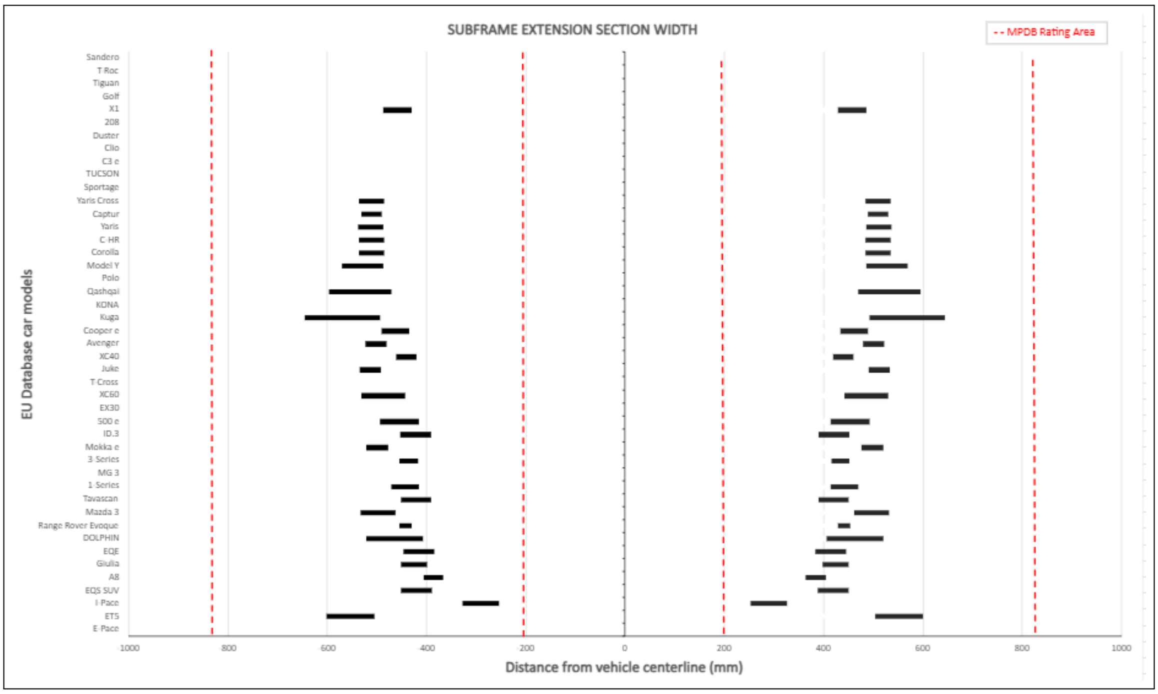

Figure A.14: Subframe Extension - Section Widths

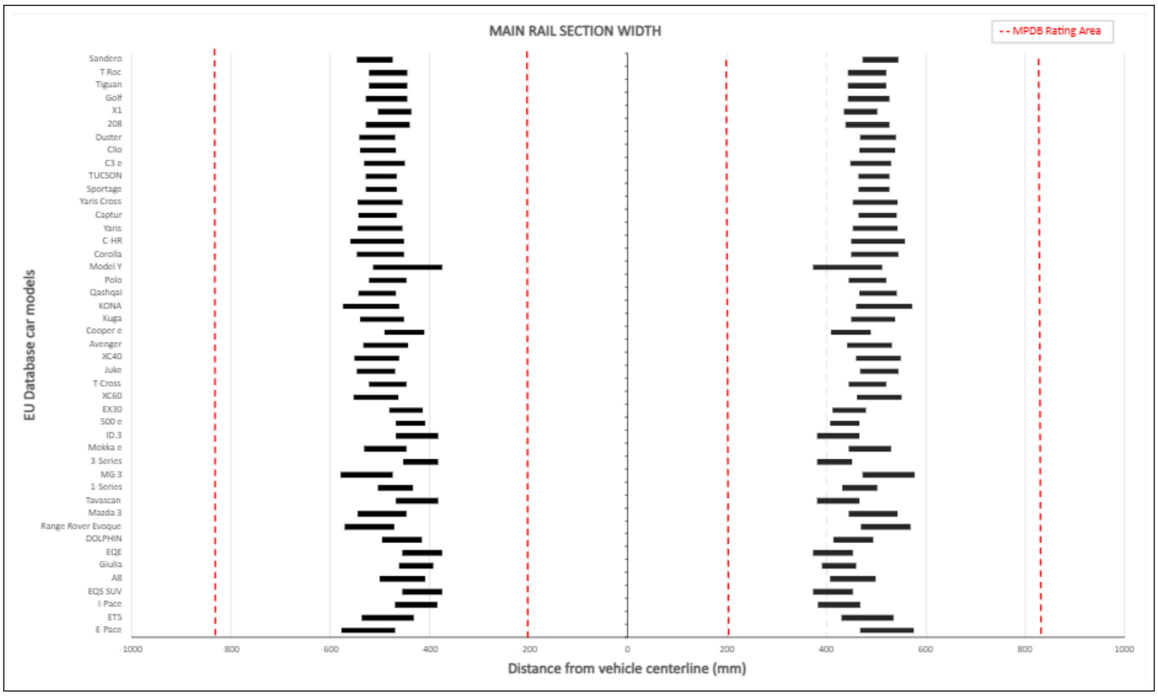

Figure A.15: Main Rail - Section Widths

A.4 Section lengths of car components

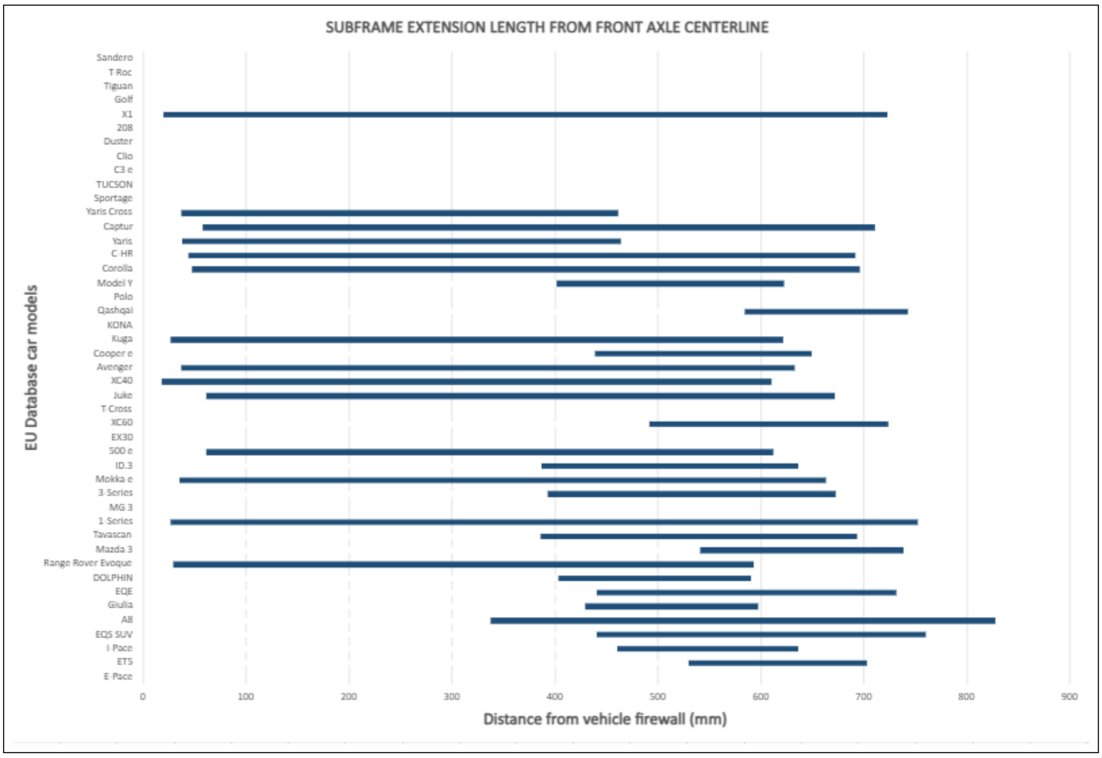

Figure A.16: Subframe Extension- Section Lengths

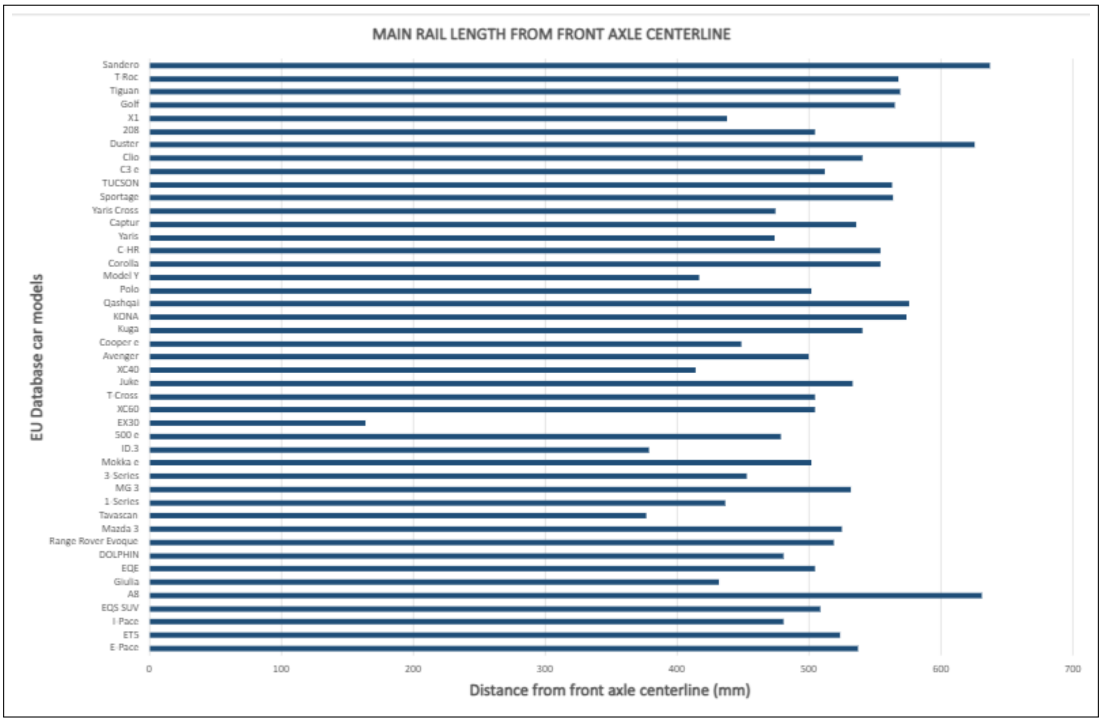

Figure A.17: Main Rail - Section Lengths

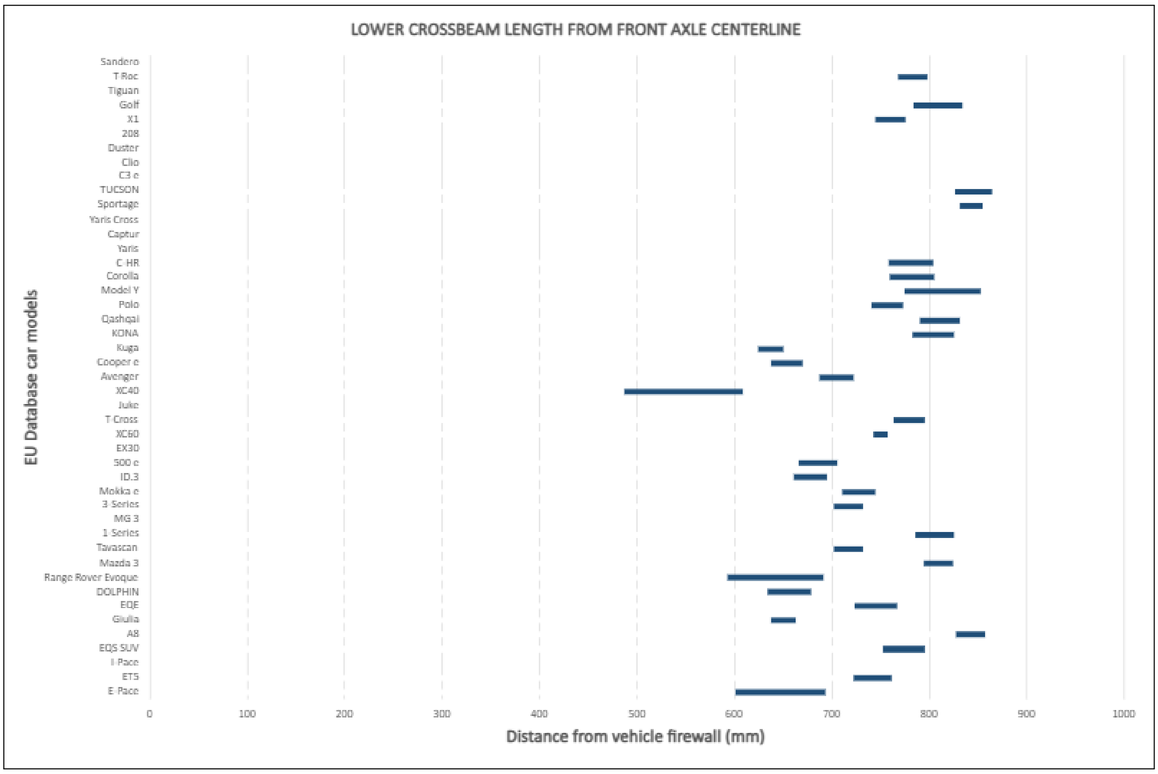

Figure A.18: Lower Crossbeam - Section Lengths

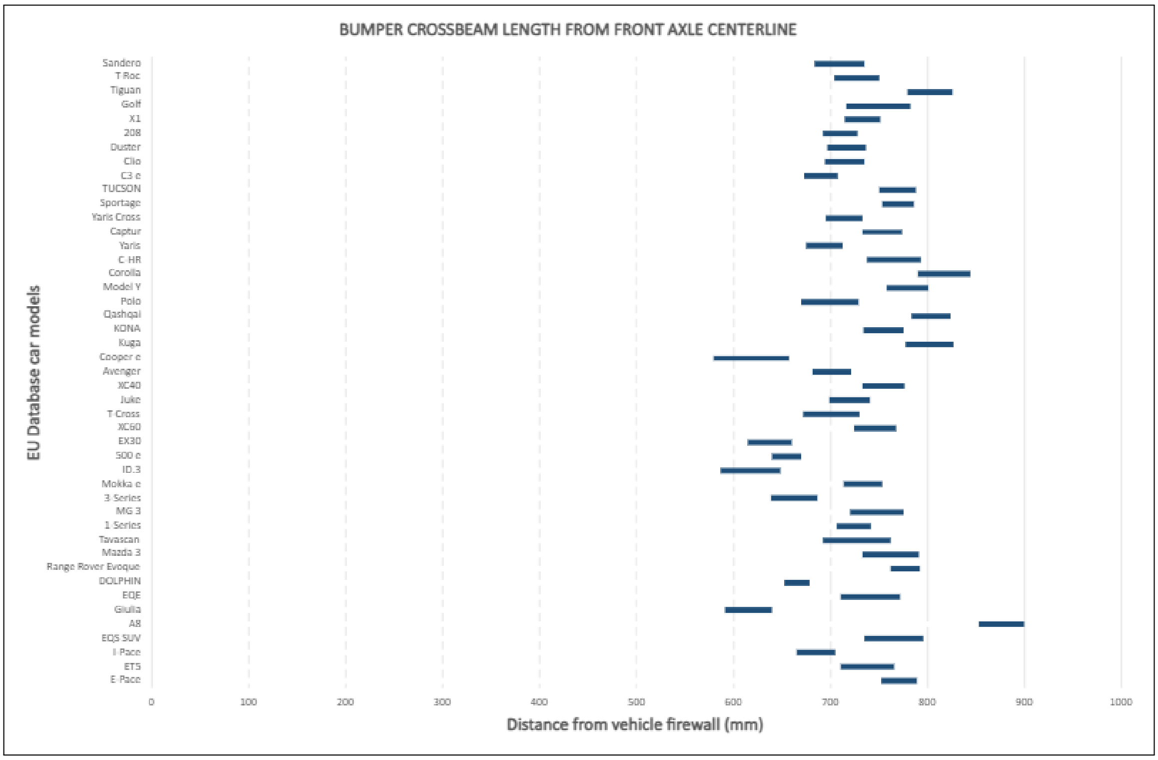

Figure A.19: Bumper Crossbeam - Section Lengths

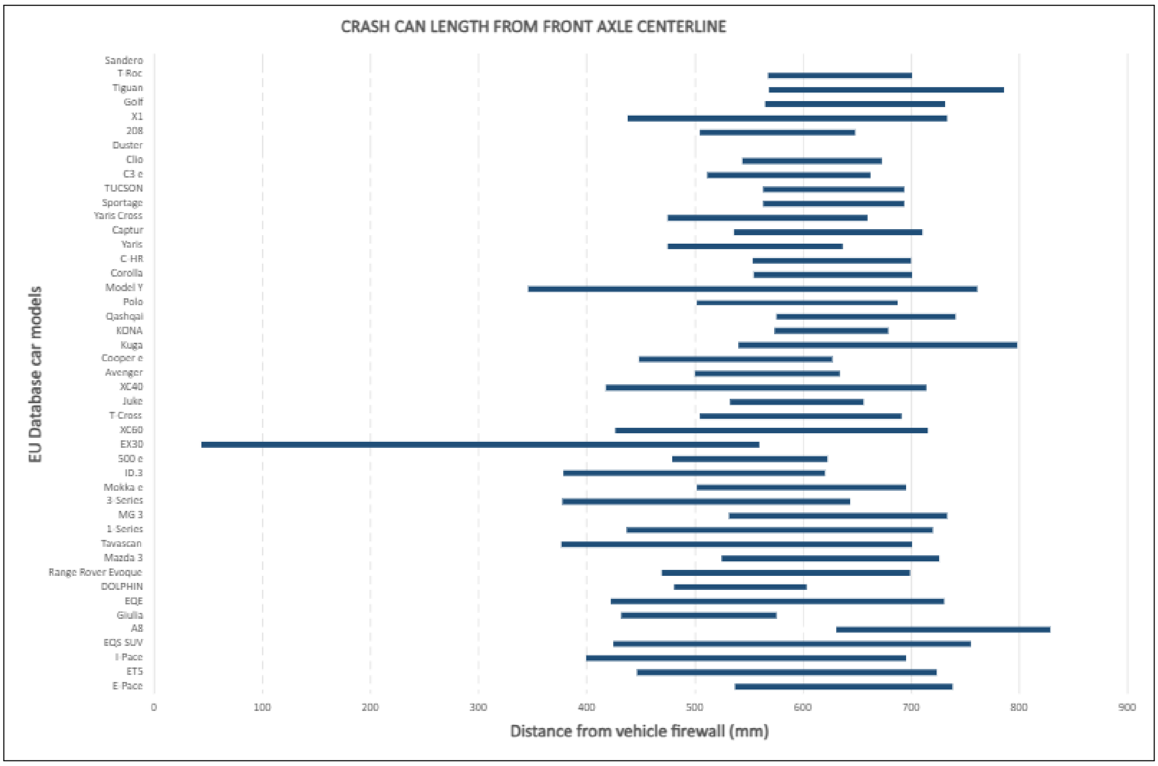

Figure A.20: Crash Can - Section Lengths

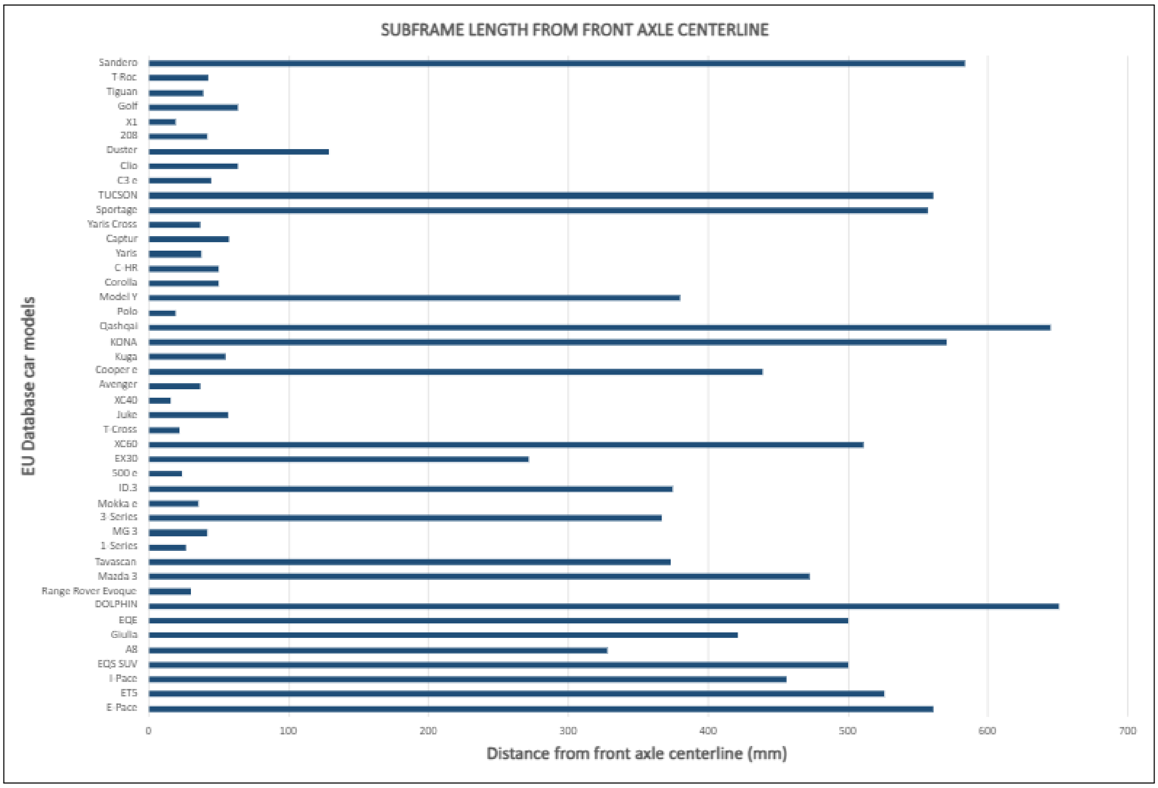

Figure A.21: Subframe - Section Lengths

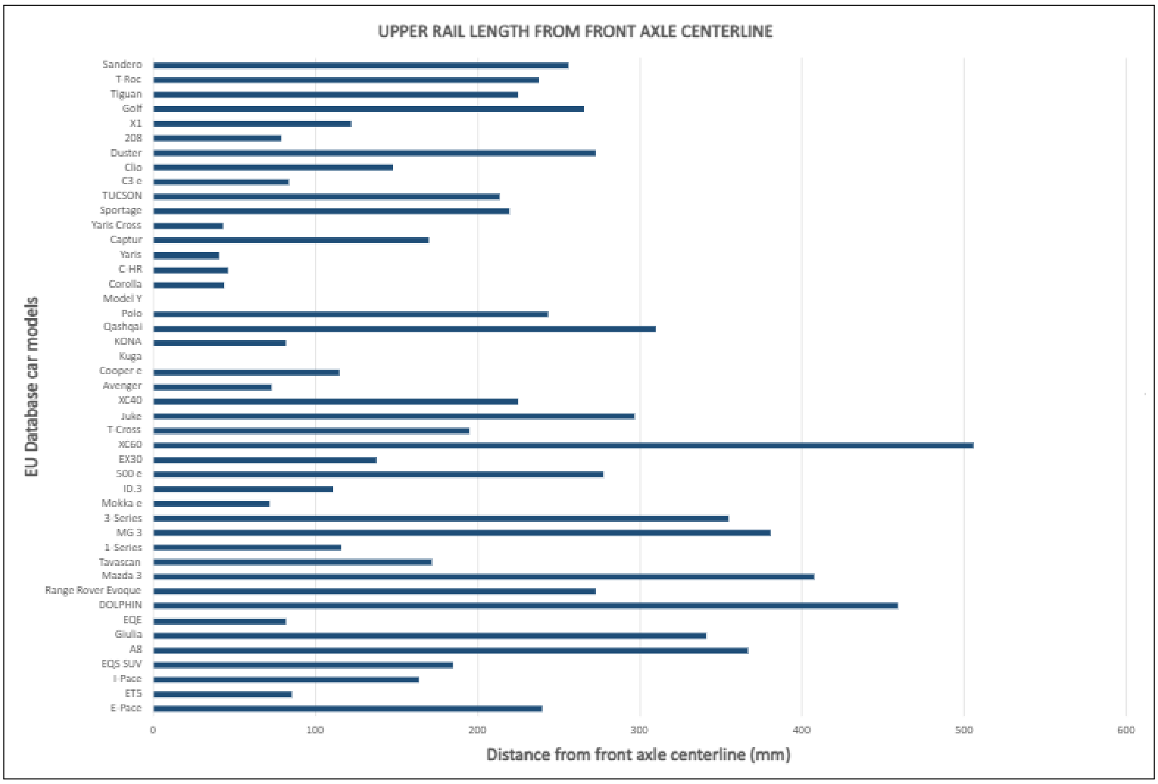

Figure A.22: Upper Rail - Section Lengths

A.5 Crash pulse response for individual cars

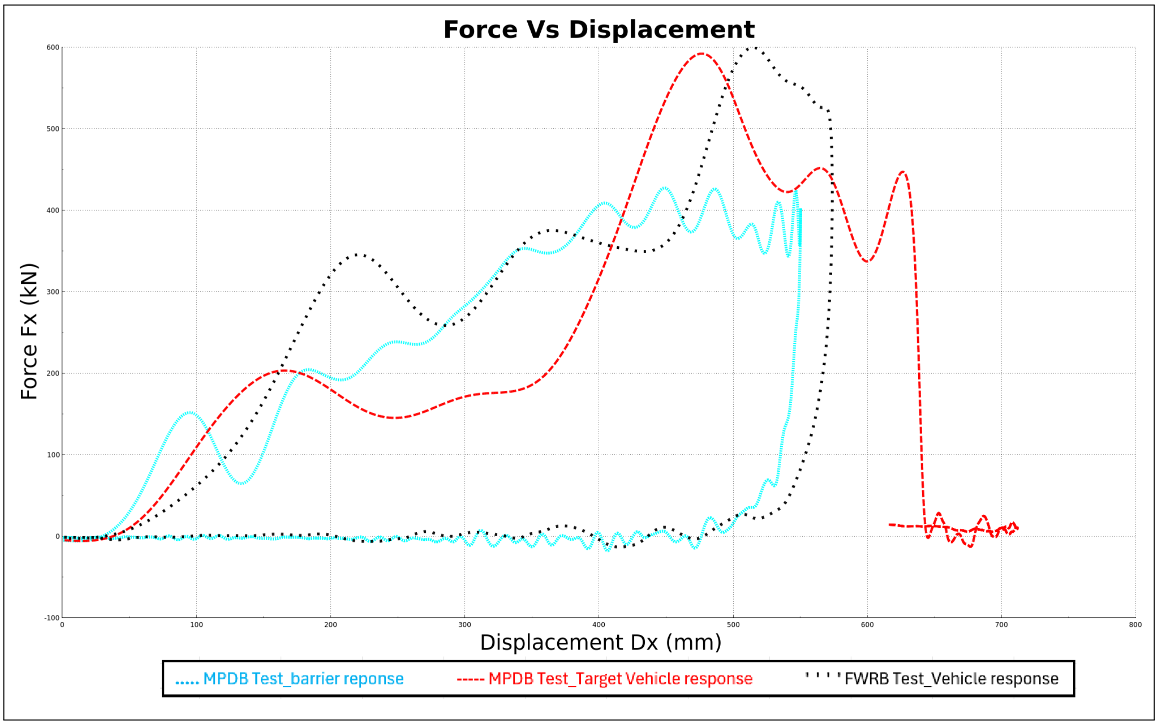

Figure A.23: Vehicle force–displacement (F–D) response - Car 1

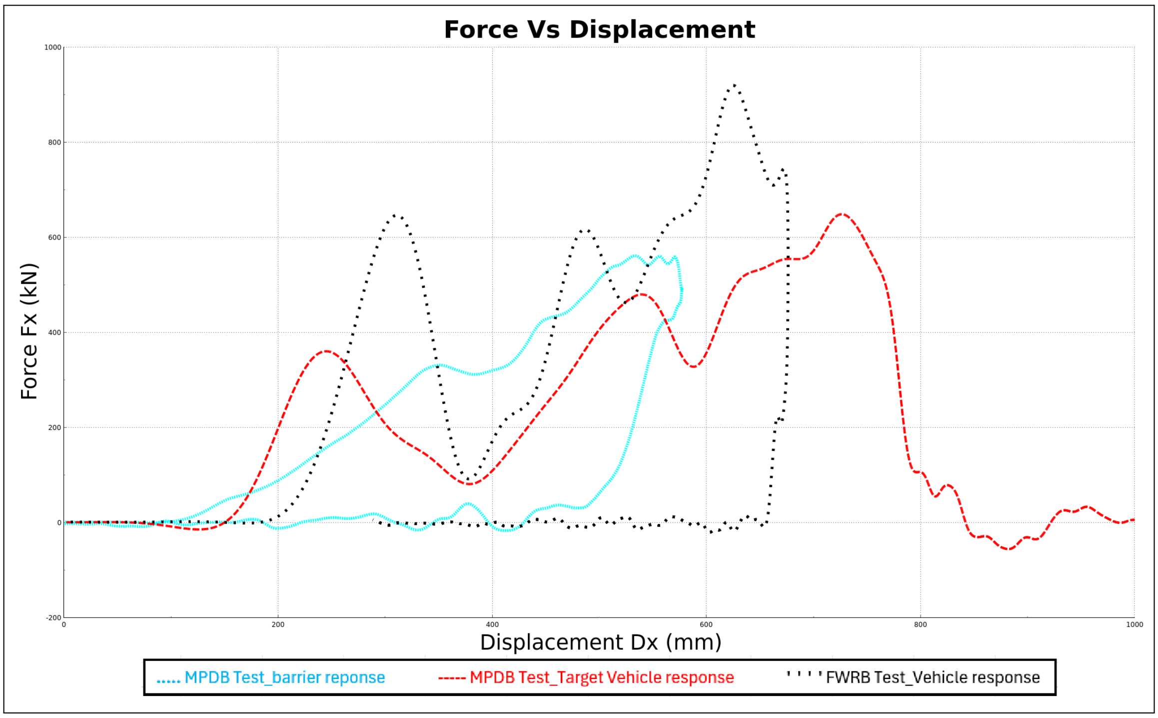

Figure A.24: Vehicle force–displacement (F–D) response - Car 2

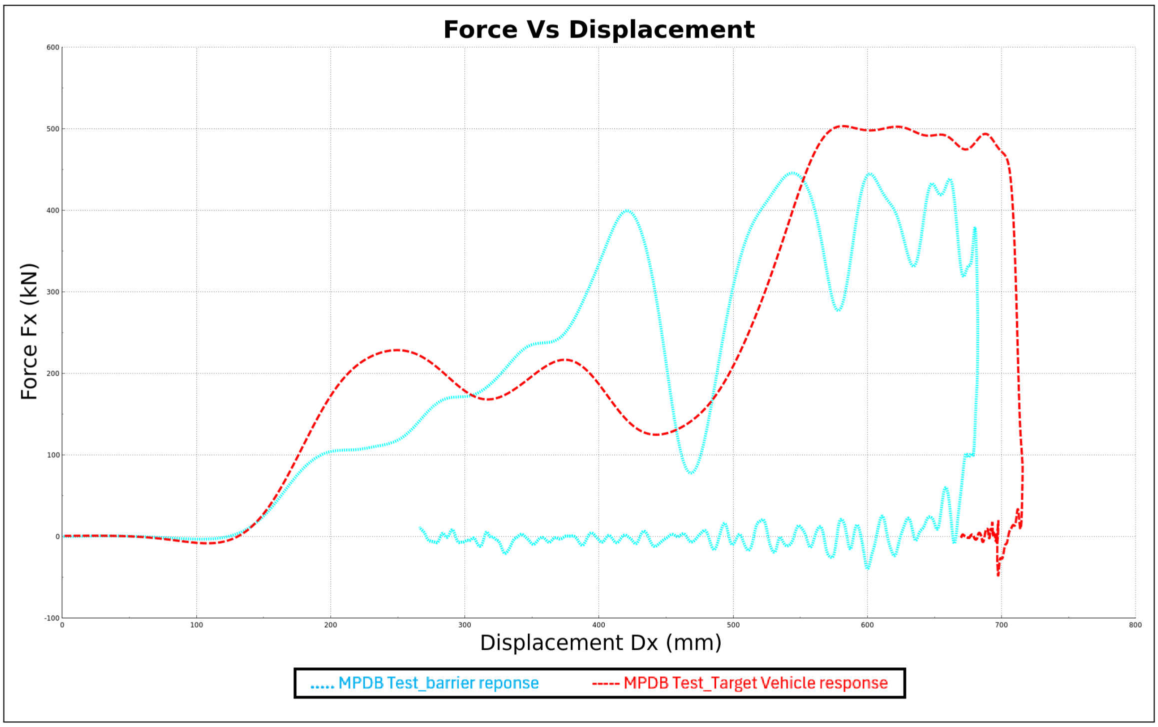

Figure A.25: Vehicle force–displacement (F–D) response - Car 3

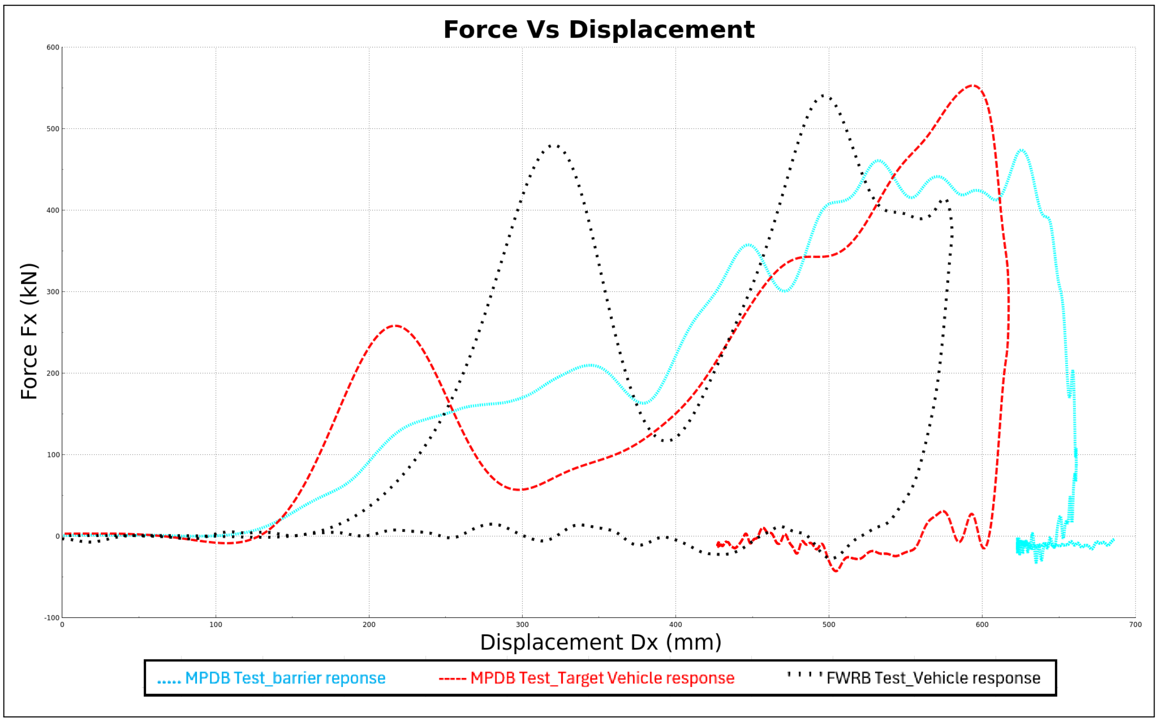

Figure A.26: Vehicle force–displacement (F–D) response - Car 4

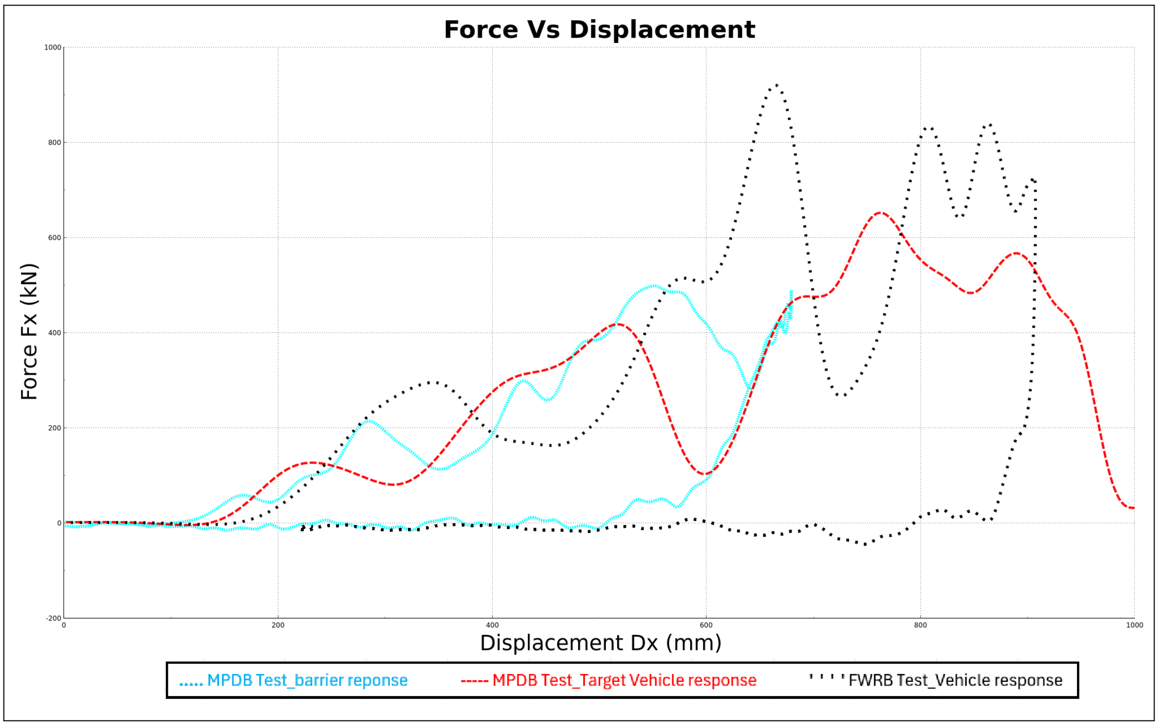

Figure A.27: Vehicle force–displacement (F–D) response - Car 5

A.6 Force distribution heatmaps for individual cars

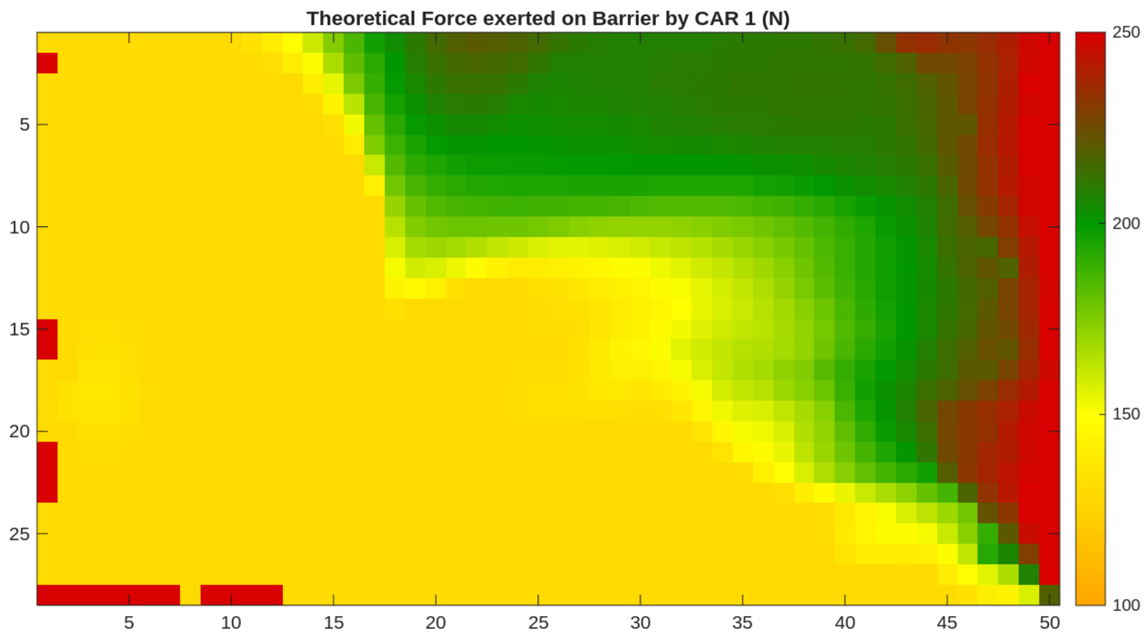

Figure A.28: Theoretical force distribution heatmap - Car 1

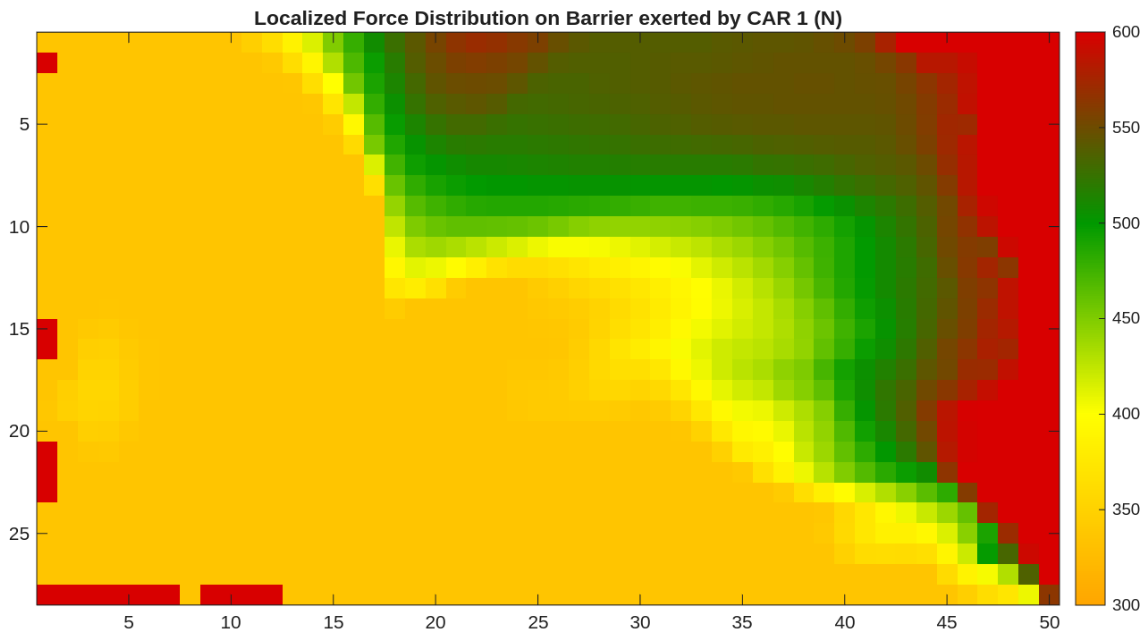

Figure A.29: Actual localized force distribution heatmap - Car 1

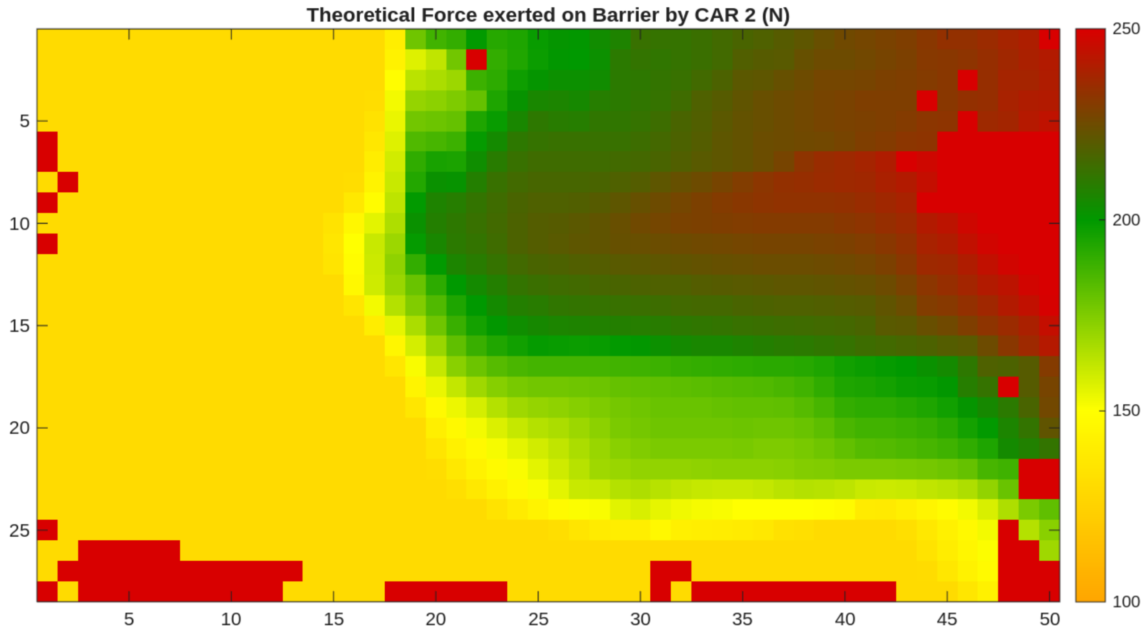

Figure A.30: Theoretical force distribution heatmap - Car 2

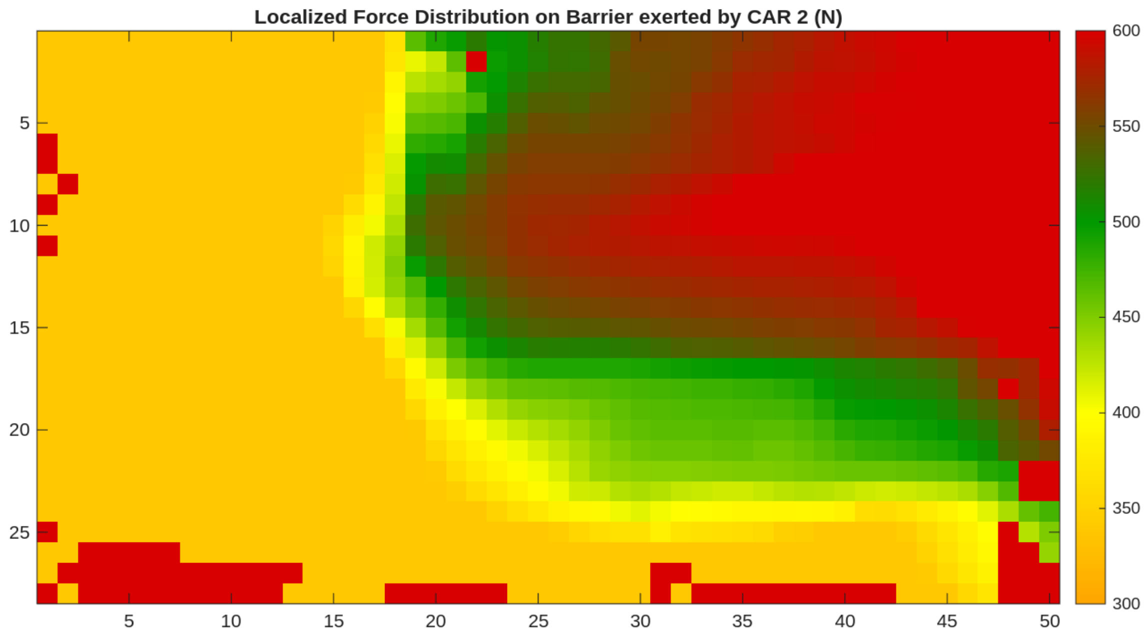

Figure A.31: Actual localized force distribution heatmap - Car 2

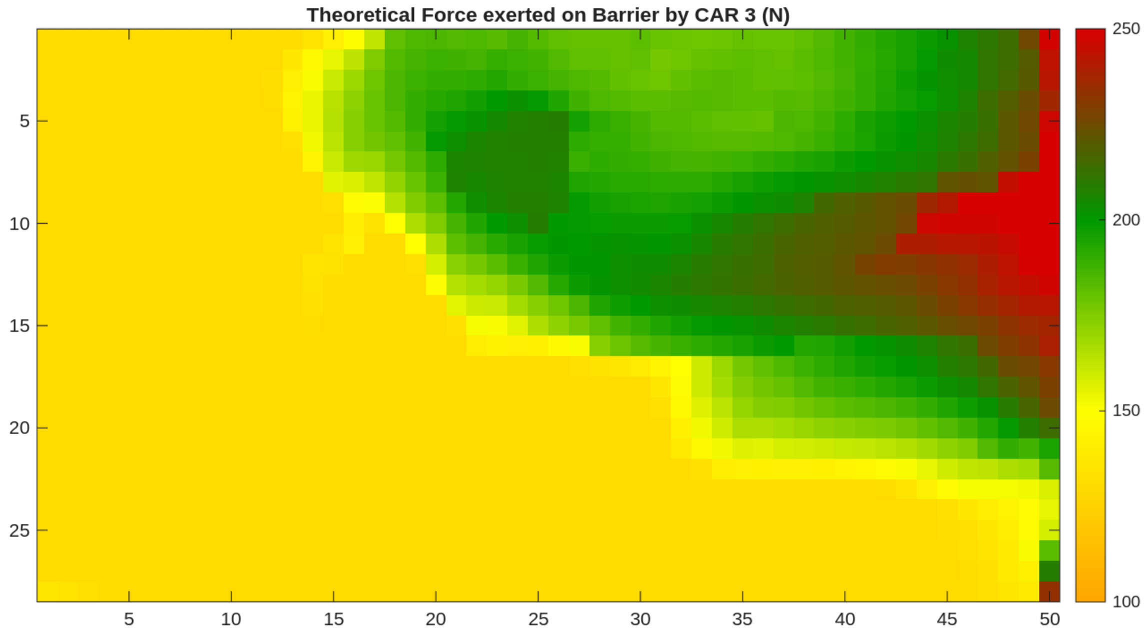

Figure A.32: Theoretical force distribution heatmap - Car 3

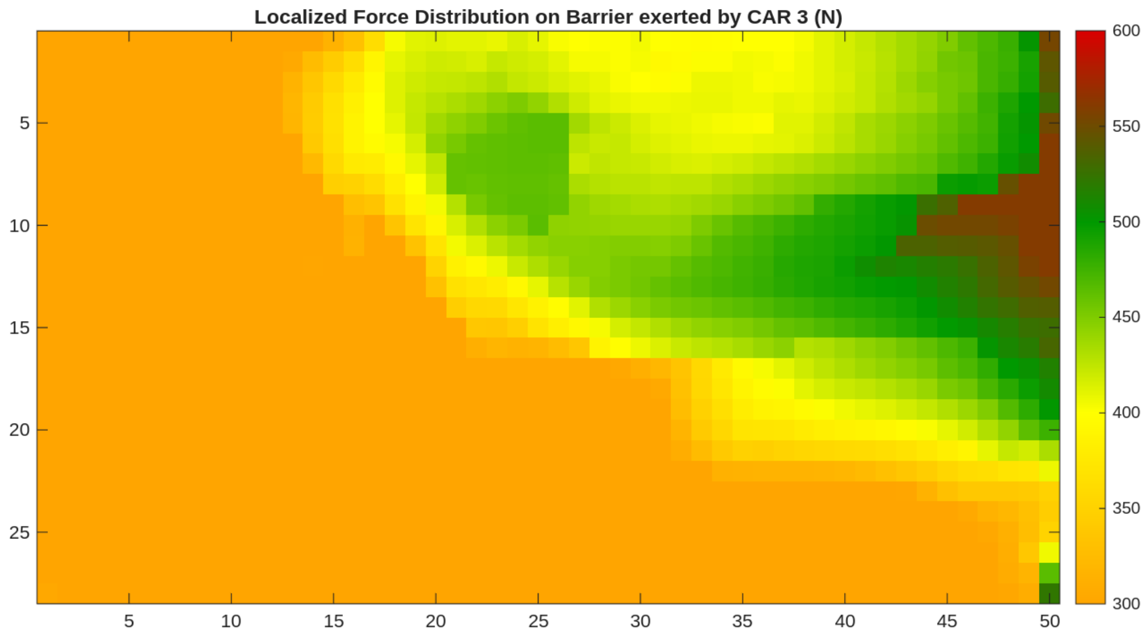

Figure A.33: Actual localized force distribution heatmap - Car 3

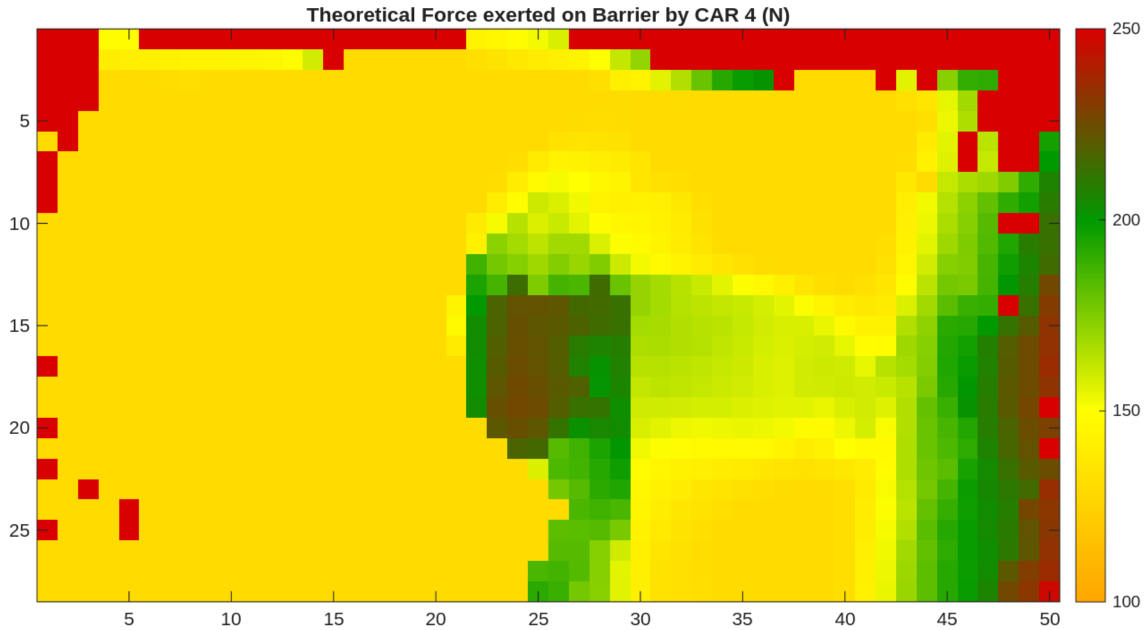

Figure A.34: Theoretical force distribution heatmap - Car 4

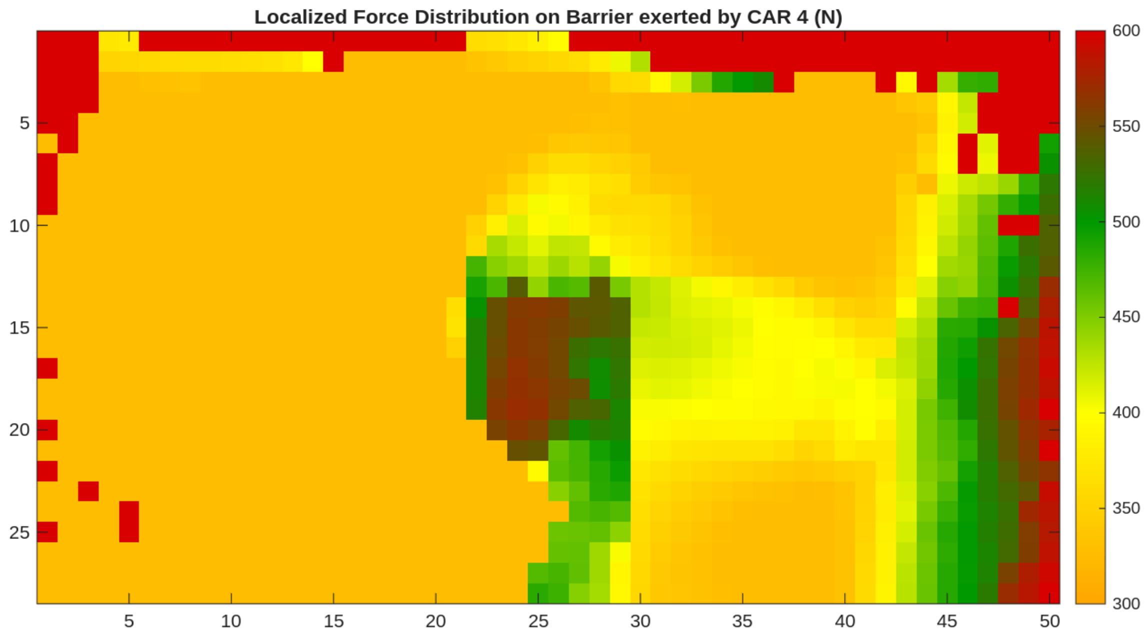

Figure A.35: Actual localized force distribution heatmap - Car 4

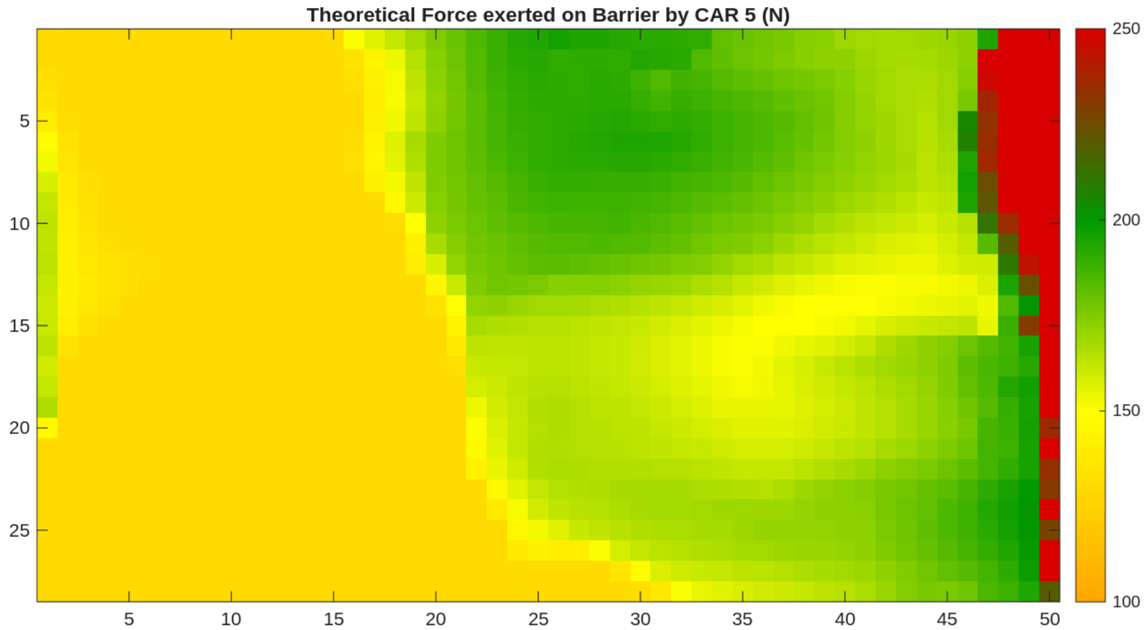

Figure A.36: Theoretical force distribution heatmap - Car 5

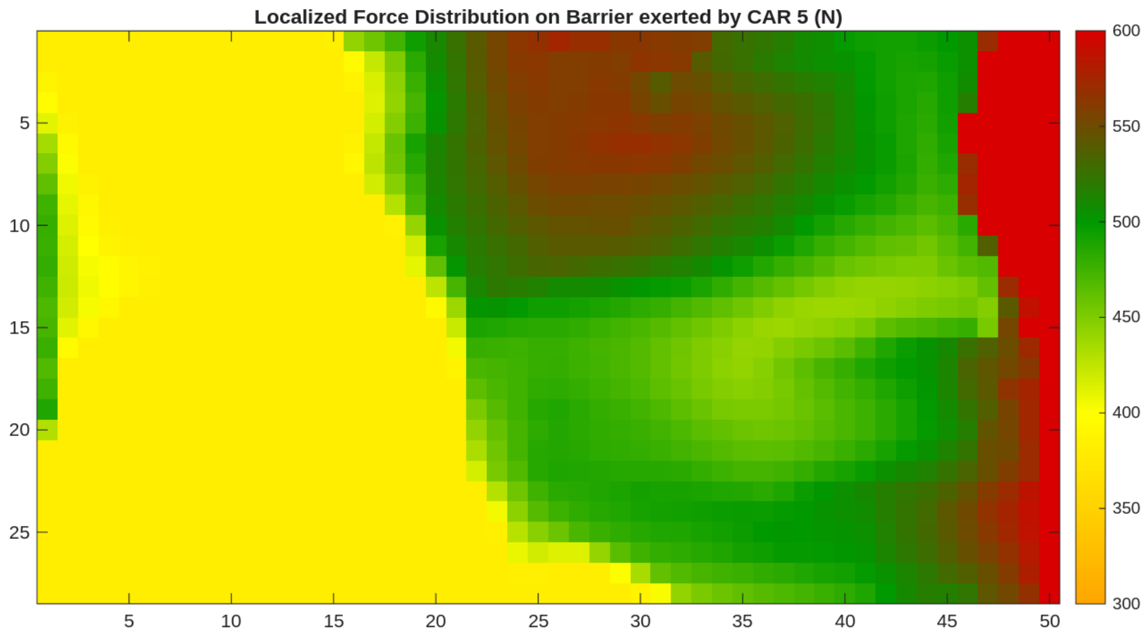

Figure A.37: Actual localized force distribution heatmap - Car 5

A.7 MATLAB script for force distribution

```
cd('/nobackup/ve_crash_06/a546880/CHALMERS/EURO_NCAP/');

% Excel file name
filenames = {'24-REN-1080-MP2_compatibility criteria.xlsx',
             '25-AUD-1106-MP1_MPDB_rating.xlsx',
             '20-SEA-0801-MP1_A204303CLEN.xlsx',
             '24-SUZ-1036-MP1_MPDB_rating_template_.xlsx',
             '25-HQI-1090-MP1_MPDB_rating.xlsx',
             '21-DAC-0861-MP2 Barrier assessment.xlsm',
             '21-FIA-0911-MP1_MPDB_euro-ncap-spreadsheet-v202001-
                mpdb.xlsm'};


% Excel range
sheet = 'Diagram';
range = 'D52:BA79';

numcars = numel(filenames);

% -------------------------------
% READ FIRST FILE FOR SIZE
% -------------------------------
A0 = xlsread(filenames{1}, sheet, range);
[nr, nc] = size(A0);

blsize = 20;
blarea = blsize^2;    % sq.mm

% -------------------------------
% PREALLOCATE
% -------------------------------
Energy_all            = zeros(nr,nc,numcars);
Force_theoretical_all = zeros(nr,nc,numcars);
Force_actual_all      = zeros(nr,nc,numcars);

% -------------------------------
% GLOBAL MAX FORCE (N)
% -------------------------------
Max_Force_list = [
591.8                %CAR 1
648.1                %CAR 2
502.8                %CAR 3
552.5                %CAR 4
651.4                %CAR 5
565.2                %CAR 6
598.8                %CAR 7
] * 1000;    % convert to N

% -------------------------------
% LOOP OVER ALL CARS
% -------------------------------
for k = 1:numcars

```

```
    A = xlsread(filenames{k}, sheet, range);
    Energy = zeros(nr,nc);

    % ---- ENERGY LOOP  ----
    for i = 1:nr
        for j = 1:nc

            def = A(i,j);
            Ecell = 0;

            d1 = min(def,250);
            if d1 > 0
                Ecell = Ecell + 0.325 * blarea * d1;
            end

            d2 = min(max(def-250,0),450);
            if d2 > 0
            sigma_start = 0.686;  % Avg of crush strength at A
                (0.756 MPa) & C(0.616 MPa) = 0.686 MPa
            slope = (1.02 - 0.686)/450; % Avg of crush strength at
                B(1.090 MPa) & D(0.950 MPa) = 1.02 MPa
                Ecell = Ecell + blarea * ...
                    (sigma_start*d2 + 0.5*slope*d2^2);
            end

            d3 = max(def-700,0);
            if d3 > 0
                Ecell = Ecell + 1.623 * blarea * d3;
            end

            Energy(i,j) = Ecell;

        end
    end

    % ---- FORCE ----
    Force_theoretical = Energy ./ max(A,1e-6);

    % Use car-specific max force
    Max_Force = Max_Force_list(k);

    % ---- DISTRIBUTION ----
    W = Force_theoretical;
    W_norm = W / sum(W,'all');

    Force_actual = Max_Force * W_norm;

    % ---- STORE ----
    Energy_all(:,:,k)             = Energy;
    Force_theoretical_all(:,:,k) = Force_theoretical;
    Force_actual_all(:,:,k)       = Force_actual;
end

% -------------------------------
% AVERAGE OVER ALL CARS
% -------------------------------
```

```
Force_theoretical_avg = mean(Force_theoretical_all,3,'omitnan');
Force_actual_avg      = mean(Force_actual_all,3,'omitnan');

% Use reference deformation (first car)
A_ref = A0;

% -------------------------------
% COLORMAP
% -------------------------------
n = 256;
orange = [1 0.65 0];
yellow = [1 1 0];
green  = [0 0.6 0];
red    = [0.85 0 0];

cmap = interp1([1 2 3 4], ...
    [orange; yellow; green; red], ...
    linspace(1,4,n));

% -------------------------------
% FULL GRID PLOTS
% -------------------------------

% Theoretical Force
figure;
imagesc(Force_theoretical_avg);
set(gca,'YDir','reverse'); axis equal tight; colorbar;
colormap(cmap);
title('Average Theoretical Force (N)');
% Local Force
figure;
imagesc(Force_actual_avg);
set(gca,'YDir','reverse'); axis equal tight; colorbar;
colormap(cmap);
title('Average Local Force (N)');

% -------------------------------
% 7 by 10 BLOCK AVERAGING
% -------------------------------
blk_r = 4;
blk_c = 5;

nRows = nr/blk_r;
nCols = nc/blk_c;

Force_theoretical_7x10 = zeros(nRows,nCols);
Force_actual_7x10 = zeros(nRows,nCols);
%Stiffness_7x10    = zeros(nRows,nCols);

for i = 1:nRows
    for j = 1:nCols

        r1 = (i-1)*blk_r+1; r2 = i*blk_r;
        c1 = (j-1)*blk_c+1; c2 = j*blk_c;

        Force_theoretical_7x10(i,j) = mean( ...
```

```
            Force_theoretical_avg(r1:r2,c1:c2),'all');

        Force_actual_7x10(i,j) = mean( ...
            Force_actual_avg(r1:r2,c1:c2),'all');
    end
end

% ------------------------------
% 7 by 10 FORCE PLOT - THEORETICAL
% ------------------------------
figure;
imagesc(Force_theoretical_7x10);
set(gca,'YDir','reverse'); axis equal tight; colorbar;
clim([100 250]);
colormap(cmap);
title('7 by 10 Average Theoretical Force Distribution for 7 cars (N
    )');

for i = 1:nRows
    for j = 1:nCols
        text(j,i,sprintf('%.0f',Force_theoretical_7x10(i,j)),...
            'HorizontalAlignment','center',...
            'FontWeight','bold');
    end
end

% ------------------------------
% 7 by 10 FORCE PLOT - ACTUAL
% ------------------------------
figure;
imagesc(Force_actual_7x10);
set(gca,'YDir','reverse'); axis equal tight; colorbar;
clim([300 600]);
colormap(cmap);
title('7 by 10 Average Localised Force Distribution for 7 cars (N)'
    );

for i = 1:nRows
    for j = 1:nCols
        text(j,i,sprintf('%.0f',Force_actual_7x10(i,j)),...
            'HorizontalAlignment','center',...
            'FontWeight','bold');
    end
end
```

DEPARTMENT OF MECHANICS AND MARITIME SCIENCES
CHALMERS UNIVERSITY OF TECHNOLOGY
Gothenburg, Sweden
www.chalmers.se

CHALMERS
UNIVERSITY OF TECHNOLOGY